OPTIMAL DESIGN OF ELECTRICAL INTERCONNECTION SYSTEMS IN FUTURE ELECTRIC AIRCRAFT

A thesis submitted to The University of Manchester for the degree of

Doctor of Philosophy

in the Faculty of Science and Engineering

2022

HANG XU

Department of Electrical and Electronic Engineering

Table of Contents

List of Figures

List of Tables

Abstract

Future aircraft will use more electrical energy to replace the traditional energy sources as electrical systems are more reliable, environmentally friendly and have lower maintenance costs. Increasing electric power levels result in increasing voltage and current levels, putting more electrical and thermal stresses on electrical interconnection systems (the cables and connectors that run across the aircraft). This thesis focuses on research into high voltage interconnection systems in future aircraft. It aims to investigate current carrying capacity and safe operating voltage related to electrical interconnection systems considering several key operating factors such as temperature, pressure and frequency. The performance of novel busbars and screened cables are compared with conventional aircraft cabling to investigate the advantages they could provide in an aerospace environment.

A thermal model for the determination of current carrying capacity of rods (simulating round cables) and busbars was developed and validated by experimental results under various geometries and operating conditions. Busbars showed a higher current carrying capacity when compared with rods under the same cross-section area and operating condition. The phenomenon was clearer when the busbar aspect ratios were increased. The effect of insulation thickness and frequency on current carrying capacity was also investigated, something not considered in the current standards. The increasing frequency led to a lower current carrying capacity due to skin effect, whilst increasing insulation thickness led to either increasing or decreasing current carrying capacity, depending on the geometry and operating conditions.

The safe operating voltage of unscreened cables and busbars was investigated based on electric field simulations and the streamer criterion method. The results showed that safe operating voltage was determined by the minimum partial discharge inception voltage (PDIV) of the phase-phase geometry. The increasing conductor diameter led to a decrease in the safe operating voltage of unscreened cable, with its effect on the safe operating voltage of unscreened busbars being negligible. For both unscreened cable and busbars, increasing the relative permittivity of insulation resulted in a lower PDIV. However, due to the limited range of permittivity values, its sensitivity was not as large as the insulation thickness, especially under low pressures. Insulation thickness is the most important parameter to determine the PDIV.

The PDIV for cable termination with and without a stress grading system was also measured. The results showed that stress grading material increased the PDIV regardless of operating condition. Frequency had no effect on the PDIV for cable termination without stress grading material. The PDIV decreased with the increasing frequency when stress grading material was applied but was overall higher than the values measured without a stress grading system. The electric field simulation results for the stress grading system showed that the partial discharge inception electric field decreased with decreasing pressure under a fixed frequency, while the partial discharge inception electric field increased and then saturated around 500 Hz under a fixed pressure. Based on the investigation of parameters controlling the electric field distribution of the stress grading material, the effect of stress grading material properties on electric field distribution along the cable termination surface was analysed.

The power carrying capacity and power/weight ratio of unscreened cable, unscreened busbar and screened cable were calculated and compared based on their current carrying capacity and safe operating voltage. The effect of conductor size and insulation thickness on power/weight ratio was analysed. Increasing conductor size and insulation thickness increased power carrying capacity but did not provide the maximum power/weight ratio.

Declaration

I declare that no portion of the work referred to in the thesis has been submitted in support of an application for another degree or qualification of this or any other university or other institute of learning.

Copyright Statement

Acknowledgement

First and foremost, I would like to express sincere gratitude to my supervisor, Prof. Ian Cotton, for his guidance, support and encouragement throughout my PhD study. I could not have imagined completing this research work without his invaluable suggestions and inspirations.

I would like to thank Dr Robert Lowndes for his helpful discussions throughout this research. Also thanks to Dr. Richard Gardner and Dr Vidyadhar Peesapati for their help on my experimental work.

I also would like thanks all my colleagues and friends at the University of Manchester especially in the Department of Electrical and Electronic Engineering. Their companionship made the journey very enjoyable.

Last but not least, I would like to express my gratitude to my family for their unconditional love, continuous support and encouragement throughout the period of my PhD.

Chapter 1. Introduction

1.1 Background

In the modern transportation network, aviation plays an important role in transporting both people and cargo. Since the first flight in 1903, air transport has been continually developing, revolutionising global connectivity [1]. According to International Air Transport Association (IATA), approximately 4 billion passengers and 64 million tonnes of cargo were transported through 22,000 airline routes in 2018 [2]. IATA also predicted that the air passenger journal would grow at an annual rate of 3.7% from 2015 to 2035 [3].

The rapid growth of the aviation industry has also impacted on the environment, especially greenhouse gas (GHG) emissions. In 2018, commercial aviation accounted for 2.4% of global man-made GHG emissions. The GHG emissions of commercial aviation is expected to triple by 2050 [4]. In order to control the impact of aviation emissions on climate change, IATA targeted that GHG emissions from total civil aircraft would be reduced by half by 2050 when compared to 2005 levels [5].

In order to achieve sustainable development, the aviation industry has incorporated more electric power in aircraft to help reduce and ultimately eliminate GHG emissions caused by aviation fuel. The maximum electric power in the Boeing 737 was 100 kVA in 1965, increasing to 1 MVA in the Boeing 787 launched in 2009 [6, 7]. Figure 1.1 presents the evolution of the installed electric power level in aircraft, highlighting the increasing tendency for electrical power in aircraft [8].

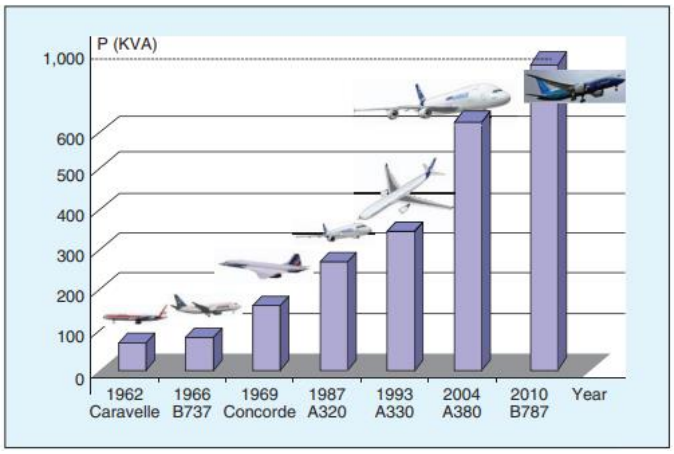

Figure 1.1 Evolution of the electric power level in aircraft [8].

In conventional aircraft, turbine engine generated power is converted to electrical, pneumatic, hydraulic and mechanical power [9]. Figure 1.2 shows the power distribution of conventional aircraft [10]. Most of the power from the engine is used to move the aircraft. The remaining power is converted into four types of non-propulsive power. The gearbox initially converts the mechanical power, before transferring it to electrical power and hydraulic power using electric generators and hydraulic pumps, respectively. Pneumatic power is obtained from the high-pressure compressors in the engine. These four types of power are used in aircraft distribution systems, such as the avionics, actuation, environmental control and wing ice protection systems [9]. Compared to the other three types of power, electrical power is both more flexible and reliable, with its key drawback being lower power density when compared with pneumatic and hydraulic power [9, 10].

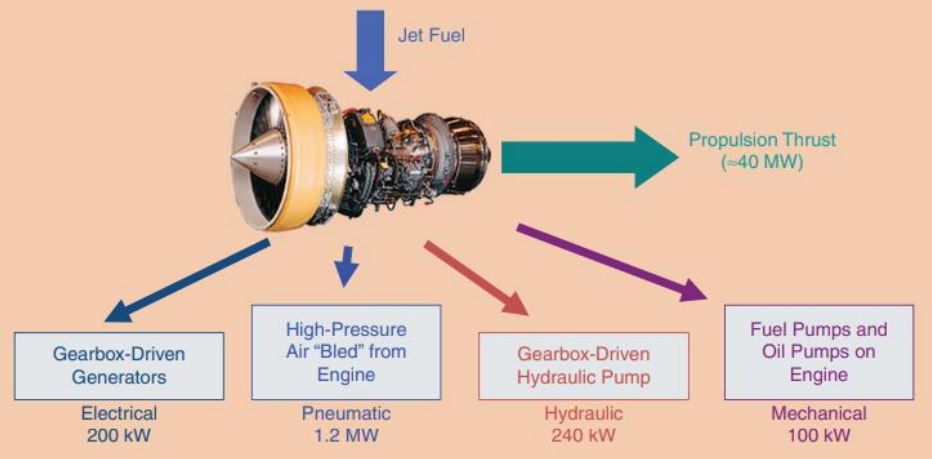

Figure 1.2 Power system of a conventional large civil aircraft [10].

Figure 1.3 shows the power distribution system of a more electric aircraft (MEA) [10]. Compared with conventional aircraft, it replaces non-propulsion systems, which includes the pneumatic, mechanical and hydraulic systems, with an electrical alternative [9, 11]. For example, the Boeing 787 has a fully electrical ice-protection and environmental control system, which had previously been controlled by pneumatic power [12].

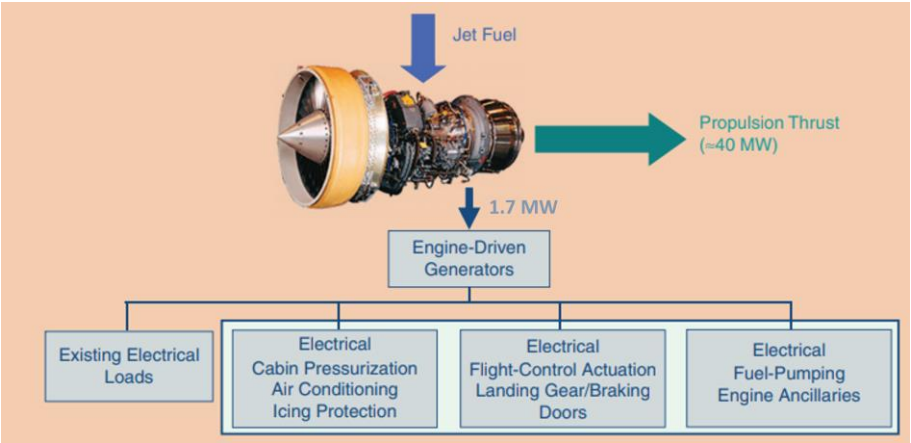

Figure 1.3 Power system of a MEA [10].

The advantages of MEA compared with conventional aircrafts are summarised as follows [6, 11-13]:

- Reduced GHG emissions and noise level to ensure sustainable development.
- Increased efficiency by eliminating interaction between different power systems and centralising the whole system.
- Increased reliability by eliminating pneumatic and hydraulic system leakage risks, thus decreasing maintenance costs.

The most common voltage level is 115 VAC and 28 VDC in existing aircraft. The frequency of the first generation voltage was fixed at 400 Hz. At this frequency, the electrical equipment such as transformer and motor is smaller and lighter than that at 50 Hz or 60 Hz, which reduces the overall weight of aircraft. The fixed frequency is achieved by a constant speed mechanical gearbox, which is then completed by AC-DC and DC-AC power converters as the power electronics provide higher reliability and lower cost [9]. To simplify the equipment required to convert various-speed mechanical power generated by an engine to constant-frequency electrical power applied in the electric system, variable-frequencies are used in MEA to reduce the weight associated with the gearbox. To deliver a higher electric power level, the voltage level has been increased to 230 VAC (360 Hz-800 Hz) and ± 270 VDC in most Boeing 787 electrical aircraft [6].

The ultimate goal of the aviation industry is to achieve all-electric aircraft (AEA) [7]. Compared with a MEA, an AEA does not only replace conventional power system with electrical alternatives but also uses electrical power from batteries or fuel cells to

provide propulsion power. Figure 1.4 shows an electrical air taxi, VoloCity, designed for two people that commenced its first fight with a cruise speed of 70 km/h in 2016 [1]. Its travel range has increased from 27 km to 35 km from 2016 to 2019, with its maximum speed achieving 110 km/h in 2019 [1, 14]. An all-electric VTOL (vertical take-off and landing) aircraft, CityAirbus, plans to make its prototype's first flight in 2023 and is expected to achieve an 80 km range with a cruise speed of 120 km/h [15].

Figure 1.4 VoloCity Designed by Volocopter [16].

Due to the limitation of power density and energy density of a battery, a hybrid-electric aircraft is a promising choice in the short-medium term for regional aircraft. These would use both gas turbines and batteries to provide propulsion power through an electric machine. A recent aircraft conversion, E-Fan X, designed by Airbus, Rolls-Royce and Siemens, used a 2MW electric motor to achieve hybrid-electric techniques in 2020. It aimed to accommodate 50-100 passengers in 2035 [17]. The electrical power level in hybrid-electric aircraft is expected to be between 2 and 16 MW, with passenger numbers between 50 and 150 [1]. The potential GHG emission reduction is expected to be between 40% and 80% [1].

According to IATA, battery or fuel cell powered aircraft for 50 and 80 passengers is expected to be achieved between 2035 and 2045 [1]. Wright Electric is targeting an AEA model for 150 passengers with a distance of 540 km by 2035 [18]. Electrical power is not emission-free at present but lower emissions are expected with the increasing usage of renewable energies [19].

Aircraft electrical interconnection systems, including aircraft cables and connectors, are used to transmit electric power in aircraft. The increasing power level can be achieved by either increasing the voltage or current levels but this will put interconnection systems under unprecedented electrical and thermal stresses. An additional challenge

for the interconnection system design is reducing the weight and size whilst ensuring safety.

Increasing voltage levels increase the risk of partial discharge and electrical system breakdown, especially under low pressure [20]. As the cruising altitude of aircraft increases, the gas molecule amount decreases, resulting in a lower air pressure compared with sea level. In most aircraft, the cabin altitude is maintained at around 6000-7000 feet by the environmental control system [21]. As a result, more insulation is required to make sure the systems are safe to operate. However, it is impossible to solely increase voltage level because thicker insulation increases both the weight and volume, and may decrease the thermal dissipation capability of interconnection systems [22]. Increasing the current level generates more losses in the conductor, leading to the need for a larger conductor size and a consequently larger weight to avoid the high temperature that could possible damage the insulation material surrounding the conductor [20]. Furthermore, the frequency in future aircraft is expected to increase to kilohertz to reduce the size and weight of equipment [23]. An increasing frequency can also increase the power density of the generator. However, an increasing frequency leads to a higher conductor resistance caused by the skin effect and proximity effect which may result in further thermal challenges [13]. Accordingly, there is a trade-off between voltage and current levels when aiming to achieve a minimum power/weight ratio in interconnection systems.

The traditional aircraft cables shown in Figure 1.5 are used to transmit electric power in MEA [24]. They were originally designed for a 28 VDC and 115 VAC network, and then extended to ± 270 VDC and 230 VAC due to the increasing voltage level. A conventional aircraft cable has a simple geometry, with the design including a conductor surrounded with single or multiple insulation layers. There has been little technical development of this type of cable due to the relatively low voltage level in aircraft.

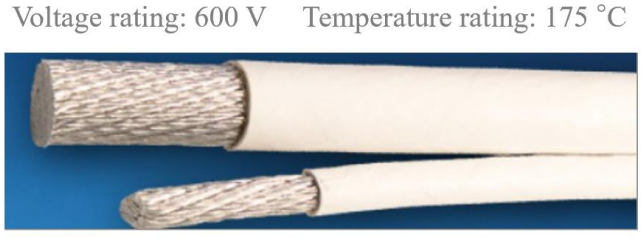

Figure 1.5 Traditional aircraft cables [24].

Due to the increasing power demand, alternative interconnection systems are required to replace traditional aircraft cables to provide higher power carrying capacity. Screened cables have been introduced by Habia to ensure cables are free of air gaps and impurities [25]. They have similar geometry to the screened cables used in a ground electric power system. Compared with unscreened cables, screened cables can control the electric discharge inside a cable due to the electric field being retained within the insulation. The operating voltage of Zerocarc cables can be up to 10 kV AC and 50 kV DC, which satisfy the high voltage requirements of power cables for future aerospace applications [25].

Figure 1.6 Habia Zeroarc aircraft cables [25].

Partial discharge needs to be managed at the cable termination of screened cable, where the electric field is high due to the sharp shield ends. Stress grading material can be applied on the cable termination to reduce the electric field and keep the mass and volume within acceptable limits. To date, the application of stress grading material on cable termination under atmospheric pressure has been widely investigated [26]. However, there is a lack of information on stress grading material applied to aerospace cable termination. The existing research on stress grading material focuses on ground cables, which operate under power frequency (50 Hz or 60 Hz) and atmospheric pressure. However, aircraft cables operate under higher frequency and lower pressures. There is a lack of information on the performance stress grading materials under these conditions. A better understanding of stress grading material in the aerospace environment will assist the application of screened cable applied in future electric aircraft.

Busbars are promising choices for interconnection systems in future aircraft. While cylindrical cables have been the traditional choice for interconnection systems given

their mechanical flexibility allowing their easy routing to different parts of the aircraft, they are not necessarily optimal in terms of weight and space. Busbars can reduce mass efficiently, minimise issues associated with the skin effect and have a high current carrying capacity [27]. In the power system for the Royal Navy Queen Elizabeth Class aircraft carrier, the installation of insulated busbars can save 42% of space than cables, with the mass reduced by 42% or 58% when using copper or aluminium as conductor, respectively [28]. Reducing mass is important in aircraft, with each kilogram saved per flight potentially saving 1,700 tons of fuel and 5,400 tons in GHG emissions per year [8]. Therefore, it is necessary to investigate the electrical and thermal performances of busbars in comparison with conventional cables in aerospace environments.

1.2 Research Aim and Objectives

The aim of this PhD study is to investigate the current carrying capacity and safe operating voltage of different designs of interconnection systems in future electrical aircraft. The work will optimise the interconnection system design by analysing power carrying capacity and weight. Both cables and busbars will be studied and compared to determine whether unscreened busbars and screened cables are promising alternatives to conventional aircraft cables. To achieve the research aim, the following objectives are covered in this PhD study. The rationale for these objectives is described within the literature review.

(i) To Investigate Thermal Performance and Current Carrying Capacity of Cables and Busbars

The existing standard does not consider the effect of insulation thickness and frequency on current carrying capacity. There is still a lack of information on the thermal performance of rectangular busbars in aerospace environments. Both experimentations based on high-frequency temperature rising test and numerical simulations based on FEM thermal analysis will be conducted to analyse the effects of various geometries, materials and operating conditions on the thermal performance and current carrying capacity of cables and busbars.

(ii) To Estimate Safe Operating Voltage of Unscreened Cables and Busbars

Partial discharge inception voltage is a critical value to define the safe operating voltage of aircraft interconnection systems. Previous research focused on the PDIV of

conventional aerospace cables, with there being a lack of research on the PDIV calculation of busbars, especially in aerospace environments. The streamer criterion method will be used to analyse the effect of conductor geometry, insulation thickness and pressure on the PDIV of unscreened cables and busbars.

(iii) To Investigate the Performance of Stress Grading Material in the Aerospace Environment

Stress grading material can be used to reduce the electric field around the cable termination. However, the performance of stress grading material under aerospace operating conditions it is still not deeply understood. The PDIV of a cable termination with stress grading material will be tested under various frequencies and pressures. Then an electrostatic model will be developed to simulate the electric field distribution along the cable termination surface. Based on the partial discharge inception electric field, the PDIV of screened cable can be simulated under aircraft operating conditions.

(iv) To Compare the Power Carrying Capacity of Different Interconnection Systems

Based on the thermal and electrical models, an optimal design process will be developed by comparing the power carrying capacity and the power to weight ratio of unscreened cables, unscreened busbars and screened cables under various designs and operating conditions. The possibility of applying unscreened busbars and screened cables in future electric aircraft will be investigated.

1.3 Major Contributions

The major contributions of this thesis are as follows:

(i) A high-current (up to 500 A) high-frequency (up to 2000 Hz) temperature rise test setup was designed and built to simulate the practical currents in future electric aircraft. The test setup is a state-of-the-art temperature rise platform for aircraft interconnection systems that could be used to investigate the effect of frequency and current on thermal performance of both cables and busbars. This experimental platform has now been used commercially for the evaluation of cables and connectors manufactured by major suppliers.

(ii) The temperature distribution and current carrying capacity of cables and busbars were simulated based on a thermal model using the finite element method. The technical innovation of this model is considering the effect of frequency on power losses. Moreover, it can better simulate the thermal dissipation performance under complex geometries and low pressures compared to the analytical method. The simulation results were consistent with the experimental results, proving that the thermal model is accurate to be applied for both cables and busbars under aerospace conditions. The effects of insulation thickness, frequency and pressure on current-carrying capacity were also examined, with the results showing that increasing frequency and decreasing pressure led to a lower current capacity. Increasing insulation thickness may increase or decrease current capacity, depending on the specific case. The results indicate that frequency and insulation thickness need to be considered for the thermal design of interconnection systems. Busbars with an aspect ratio higher than 2 had a better thermal performance than cables with the same cross-section area.

(iii) The streamer criterion method was applied to calculate the safe operating voltage of unscreened cables and busbars as this method is suitable for non-uniform electric field. Compared with existing research only focusing on unscreened cables, it investigated the effects of conductor geometry, insulation material property and pressure on the PDIV of busbars. Results showed that the increasing cross-section area led to a decreasing PDIV (this is something that is counterintuitive to most engineers), while the PDIV was not affected by the cross-section area of busbars. For both unscreened cables and busbars, increasing the relative permittivity of insulation resulted in a lower PDIV. However, due to the limited range of permittivity values, its sensitivity was not as large as the insulation thickness, especially under low pressures. Insulation thickness is the most sensitive parameter determining the PDIV.

(iv) The performance of stress grading materials was studied under aerospace operating conditions. PDIV of the cable termination with and without a stress grading system was measured under various frequencies and pressures. The results showed that stress grading material increased the PDIV

regardless of the operating condition. Frequency had no effect on the PDIV of cable termination without stress grading material. The PDIV decreased with increasing frequency when stress grading material was applied. An electrostatic model was developed to simulate the electric field along the cable termination surface. It was used to determine the partial discharge inception electric field strength under various frequencies and pressures by inputting measured PDIV into the model. The results showed that the partial discharge inception electric field decreased with decreasing pressure while it increased with increasing frequency and saturated at around 500 Hz. Increasing initial conductivity and nonlinearity of stress grading material led to a lower electric field strength along the cable termination surface. However, it increased the electric field strength of the stress grading material ends as the stress grading system became more conductive.

(v) The power to weight ratio of unscreened cables, unscreened busbars and screened cables were compared. When the conductor size increased, the power to weight ratio of the unscreened cables continuously decreased, while the power to weight ratio of unscreened busbars and screened cables initially increased before decreasing. When the insulation thickness increased, the power to weight ratio of all interconnection systems increased to a maximum value before decreasing.

1.4 Thesis Outline

This thesis is comprised of eight chapters.

Chapter 1 Introduction

This chapter presents the background information and motivation of this PhD study. It reviews the development and benefits of MEA, and introduces the corresponding challenges associated with interconnection systems in terms of both thermal and electrical designs. It then presents the characteristics of conventional aircraft cables and the benefits of busbars and screened cables that have the potential to be applied in future MEA.

Chapter 2 Literature Review

This chapter initially reviews the characteristics of interconnection systems, including existing unscreened cables, screened cables and busbars. Existing standards and research on the current carrying capacity of aircraft cables and busbars are then reviewed. Then the partial discharge inception voltage calculation methods for unscreened interconnection systems are summarised and existing research on stress grading material on cable termination is reviewed.

Chapter 3 Validation of Current Carrying Capacity Models

This chapter initially describes the experiment setup and numerical thermal model. An overview of the test circuit, sample preparation and test procedure is described and the build-up process of the thermal model given. The simulation results are then validated by the test results for both cables and busbars under atmospheric pressure. The thermal dissipation performance in the aerospace environment simulated by the thermal model will then be validated by the experimental results.

Chapter 4 Current Carrying Capacity Design

Based on the verified thermal model in Chapter 3, this chapter initially analyses the effect of parameters, such as material, insulation thickness, frequency and pressure, on thermal performance and the current capacity of round cables. The differences between busbar and cables are then compared and analysed.

Chapter 5 Safe Operating Voltage Design

This chapter initially describes the streamer criterion method and electric field simulation model used to calculate the partial discharge inception voltage. The simulation model is then validated by comparing with results in previous research. Finally, the effect of parameters, such as geometry, insulation thickness, pressure and insulation permittivity, on the PDIV for both unscreened cables and unscreened busbars is analysed.

Chapter 6 Stress Grading System for Screened Cables

This chapter initially describes the test setup used to measure the PDIV of the cable termination before introducing the electric field simulation model used to simulate the electric field distribution along the cable termination surface. The partial discharge inception electric field under various frequencies and pressures is then presented.

Finally, the effect of stress grading material properties on the electric field distribution is discussed.

Chapter 7 Power Carrying Capacity Comparison

This chapter initially describes the power carrying capacity calculation processes of unscreened cables, unscreened busbars and screened cables based on their current carrying capacities and safe operating voltages. It then analyses the effect of conductor cross-section area and insulation thickness on the power carrying capacity of these interconnection systems. Furthermore, their power/weight ratios will be compared to provide guidance for optimal interconnection system designs in future electric aircraft.

Chapter 8 Conclusion and Future Research

This chapter describes the main findings of this PhD study and recommends future research that can be conducted into optimising the design of interconnection systems in future aircraft.

Chapter 2. Literature Review

2.1 Introduction

This chapter describes and compares the characteristics of interconnection systems consisting of existing aircraft cables, screened cables and busbars. Then existing research focused on the current carrying capacity of interconnection systems, including standards, simulation studies and experimental studies is reviewed. Finally, the safe operating voltage calculation methods for unscreened cables is reviewed, followed by a summary of the working principle, material properties and modelling of stress grading material involved in the cable termination.

2.2 Review of Interconnection Systems

2.2.1 Existing Aircraft Cables

Various types of cables have been applied in aircrafts as shown in Figure 2.1 [29]. These cables usually cooperate to transmit electric power and data. Compared with other cables, power transmission cables have a larger size as they need to withstand a high power level. Hook-up cables are applied in the airframe throughout the surfaces, wings, landing gear, avionic system and cabinet areas. They are light weight and small, connecting the load and subsystems to transmit power or signal. Data transmission cables are used to transmit data in avionics, communication and the in-flight entertainment system, with some cables connected to sensors used for environment conditioning. The data transmission cables are usually covered with a metallic sheath to avoid them being affected by electromagnetic interference [30]. High temperature cables with fire-resistant insulation are used in high temperature areas such as turbine engine and its surrounding areas, withstanding temperatures up to 310 °C [31].

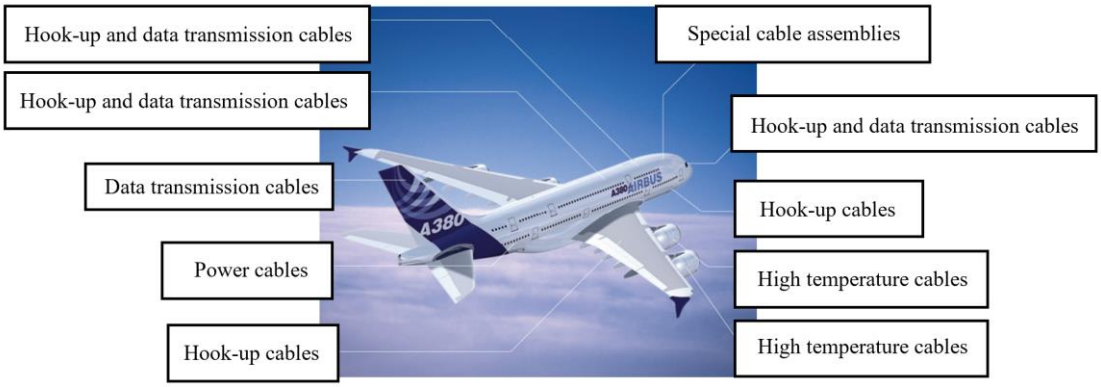

Figure 2.1. Various types of cables used in aircraft [29].

All aircraft at present use unscreened cables for power transmission. Unscreened cables consist of a solid or stranded conductor surrounded by single or multiple layered insulation. The solid conductor has better physical strength, while the stranded conductor provides better flexibility during installation. A metallic braided sheath may cover the cable surface to avoid electromagnetic interface from the surrounding environment. However, it is not a screened cable as there is an air gap between the sheath and insulation layer where partial discharge may occur. Figure 2.2 presents the typical structure of an unscreened aircraft cable [32].

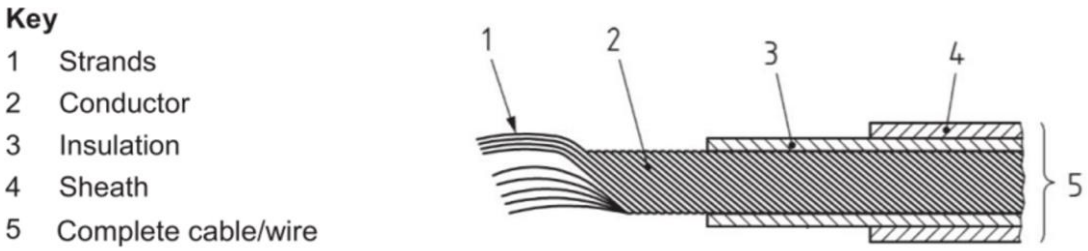

Figure 2.2 Unscreened cables configuration [32].

Power losses in aircraft cables are generated by the conductor, which leads to a high temperature and then thermal stresses on the insulation material. To optimise the temperature, it is important to match the material properties with the size of the conductor. Copper and aluminium are the two materials mainly used as conductor material, but the choice of material is a trade-off process. Compared with aluminium, copper has a lower resistivity, higher tensile strength and is easier to solder. However, it is heavier and more expensive than aluminium [33]. The main advantage of aluminium is that it has lower density than copper, which leads to a lighter weight for the same conductor resistance but a larger diameter.

Cable size in aircraft is defined by the American Wire Gauge (AWG). The AWG only defines the conductor size, with the overall cable size then including the insulation and the sheath layer. The relationship between conductor diameter and AWG number is: $Diameter = 0.127 \times 92^{\frac{36-n}{39}}\ mm$, where n is the AWG number and it is -1, -2 and -3 for AWG 00 (2/0), AWG 000 (3/0) and AWG 0000 (AWG 4/0), respectively [33]. The conductor diameter of conventional power transmission cables usually ranges from AWG 12 (2.05 mm diameter) to AWG 4/0 (11.68 mm diameter) [29]. An increasing cable size leads to a high current carrying capacity and more weight. The cable size decision is a trade-off between current carrying capacity, weight, the size of apertures in the airframe that allows the cable to be installed and flexibility.

In order to ensure aircraft cables operate as safely as possible, the insulation material is required to withstand high thermal, mechanical and electrical stresses. Furthermore, it should withstand and provide chemical resistance to any contamination on the surface. Typical aircraft cable insulation materials are polytetra-fluoroethylene (PTFE) and ethylene tetrafluoroethylene (ETFE). These materials are more expensive than the cross-linked polyethylene (XLPE) material typically used on the ground based power system but the higher operating temperature gives a key advantages compared with the operating temperature of XLPE [33-35].

At present, the maximum operating voltage for most aircraft cables is 600 V [29]. With the increasing power level, the interconnection system's insulation system in future aircraft will face challenges associated with aerospace environments. The increasing voltage level may cause partial discharge under low air pressure, which will increase the risk of electrical degradation of the insulation.

2.2.2 Screened Cables

Table 2.1 shows the voltage levels in aircraft as defined by the Society of Automotive Engineers (SAE) AE-7 committee in 2021 [36]. The committee defined these values to provide component suppliers a range of levels against which they could design components. The voltage values of both Level 1 and Level 2 are lower than the Paschen's limit (327 V). If applied voltage is lower than this value, no electric discharge occurs between two uniform electrodes in air. Most aircraft cabling systems designed for 28 VDC and 115 VAC would operate in this category. Level 3 shows the voltage

level for existing qualified cables rising to 540 VDC and 230 VAC and is therefore aligned with platforms like Boeing 787 and Airbus 350 where the 600 V cabling systems described above are used. Level 4 and above do not, as of yet, have any commercially available cable designs in routine manufacture by suppliers. Level 5 and Level 6 show the expected voltage values in future aircraft may be above 3600 VAC and 5100 VDC. With an increasing voltage level expected in future aircraft, the insulation thickness of conventional aircraft cables should be increased to avoid electric discharge. However, this will increase both the weight and volume of the interconnection system.

Table 2.1 Voltage level range definition [36].

Voltage Level Type	AC, Volt rms	Abnormal surge voltage based on L-L, rms	DC, Volt (Based on Maximum Voltage Amplitude)	Normal Transients Surge Voltage (Based on Maximum Voltage Amplitude)
Voltage Level 1	Up to 42.4 VAC	66 VAC	Up to 60 VAC	86 VDC
Voltage Level 2	42.4 to 213 VAC	332 VAC	60 to 300 VDC	432 VDC
Voltage Level 3	213 to 425 VAC	663 VAC	300 to 600 VDC	864 VDC
Voltage Level 4	425 to 851 VAC	1327 VAC	600 to 1000 VDC	1440 VDC
Voltage Level 5	Up to 3600 VAC	5612 VAC	1000 to 5100 VDC	7344 VDC
Voltage Level 6	Above 3600 VAC	Above 5612 VAC	Above 5100 VDC	Above 7344 VDC

A screened cable is a promising solution to manage the issues associated with high voltage level in future aircraft. The structure of a screened cable is presented in Figure 2.3 [37]. The semiconductor layers are used to make the electric field around the conductor and insulation surface uniform. A conducting shield is grounded and a jacket applied to protect the cable from corrosion by external pollutions.

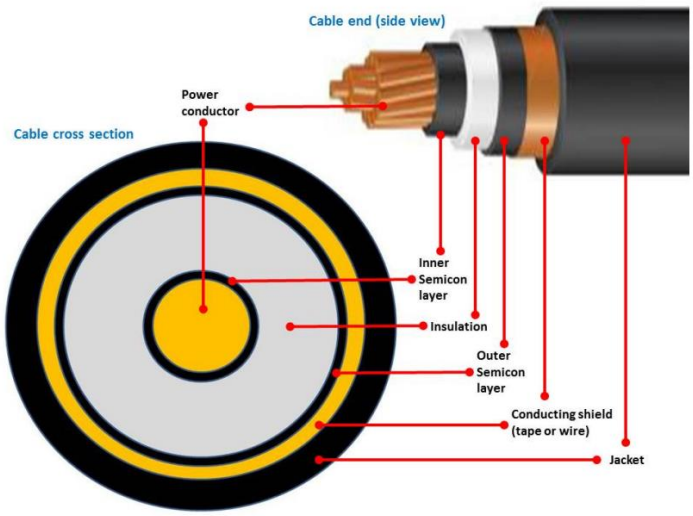

Figure 2.3 Structure of a screened ground cable [37].

Compared with an unscreened cable, the main advantage of a screened cable is that the electric field will be retained within the insulation and an electrical discharge will not be possible in the surrounding air. The electric field distribution of a screened cable and an unscreened cable are presented in Figure 2.4 (a) and (b), respectively. The results show that for a screened cable, the electric field is uniformly distributed between the conductor and screen layer. The electric stress is only withstood by the insulation material because it has a much higher dielectric strength than air. The disadvantage of a screened cable is the higher cost and larger weight caused by its complex geometry and metal shield. Moreover, its termination part has a high risk of a partial discharge because of the strong electric field around the screen edge in the termination part [38].

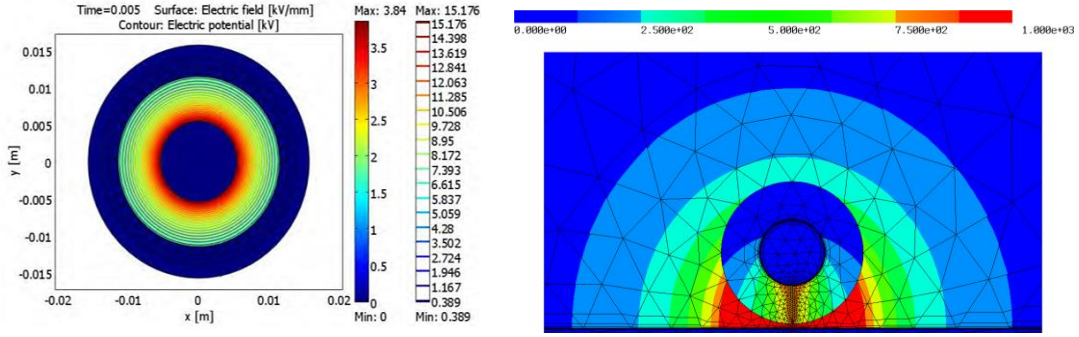

(a) (b)

Figure 2.4 Electric field simulation of (a) a screened cable and (b) an unscreened cable [39, 40].

2.2.3 Busbars

Busbars have been widely applied in power transmission equipment to transmit electric power from supply to the load [41]. A busbar is a metallic strip or bar housed in switchgear or a busbar enclosure to aid power distribution. The enclosure or casing is usually grounded as a safety consideration. A busbar can be made into non-standard shapes such as flat strip, solid rods and bars [41]. They are generally non-insulated and have enough stiffness to be fixed by insulated pillars.

The advantages of busbars over cables are [27, 41-43]:

- Higher current capacity: Busbars have better thermal dissipation than cables due to their larger surface area as a ratio of conductor cross-section [42]. In addition, an appropriate busbar shape design can decrease resistance by reducing the influence of the skin effect [41].
- Space-saving: The compact design of busbars and contours that match the building structure reduce space requirements. The overall dimensions of busbars are usually smaller than the cable system. [27, 43].
- Easier to install and maintain: Busbars are compact and allow fast installation. Due to their rigid arrangement, it is easy to change busbar components if sufficient space is available [27, 43].
- Lower fire load: Busbars are highly heat resistant as they do not use a large amount of plastic insulation materials [27].

2.3 Review of Current Carrying Capacity Designs

The current carrying capacity is defined as the maximum amount of current that can be transmitted through interconnection systems to ensure its working temperature is below the safety threshold [44]. The current capacity can be either a continuous rating or dynamic rating [45]. The continuous current capacity is the maximum current carrying capacity under steady-state operating conditions, while the dynamic current capacity is the maximum current carrying capacity for a specified period of time under short circuit or overload operating conditions. This thesis focuses on the continuous current carrying capacity because it is the most representative for operating conditions and the foundation of the current carrying capacity design in aircraft interconnection systems [44].

The current carrying capacity is dependent on various parameters, including the geometry and material properties of cable components and the surrounding environment. Both simulation and experimental methods have been applied to calculate the current carrying capacity of aircraft cables [46-50] and busbars [45, 51, 52] under various scenarios. Analytical method used to calculate the current carrying capacity uses empirical assumptions based on thermal equilibrium, where heat generation rate is equal to the heat dissipation rate. Another method used to calculate the carrying capacity is numerically solving the differential equations representing heat generation and heat transfer processes. The characteristics of this method are that it requires less assumptions but does need more computation power when compared to the analytical method [53]. Experimental methods can directly measure the current carrying capacity without any assumptions. Its disadvantages are the high cost and being more time-consuming than simulation methods.

2.3.1 Existing Standards

SAE Standard AS50881

The SAE Standard AS50881, entitled "Wiring In Aerospace Vehicles", was initially published in 1998 based on military specification MIL-W-5088X [44]. It defines the selection of the current rating for aerospace wire by considering the wire size and altitude derating factor.

The relationship between temperature difference (cable conductor temperature minus ambient temperature) and current rating for a single copper wire is shown in Figure 2.5 [44]. The current rating for a specific gauge in the range of AWG 26 and AWG 4/0 can be obtained from the graph once the maximum operating temperature and ambient temperature are known. The obtained current rating needs to be multiplied by the altitude derating factor shown in Figure 2.6 [44]. The maximum operating current for each wire can then be determined. The application of an aluminium conductor is also considered in this standard. The current rating needs to be derated by 20% when compared with that for copper for the same size. This derating factor can be explained by the difference in resistivity between copper and aluminium. When the cable size is the same, the heat transfer to the surrounding environment of a cable made of copper and aluminium is the same (assuming both cables have the same maximum operating temperature and surface emissivity). Therefore, the heat losses of the conductors for the

two cables should be the same. Assuming the temperature is 200 °C, the resistivity of aluminium is 4.87×10^{-8} Ω·m 200 °C while the resistivity of copper is 2.93×10^{-8} Ω·m [41]. According to the heat generation equation I^2R, the current carrying capacity of an aluminium cable is around 78% of that of a copper cable. It explains the 20% derating factor for an aluminium conductor mentioned above.

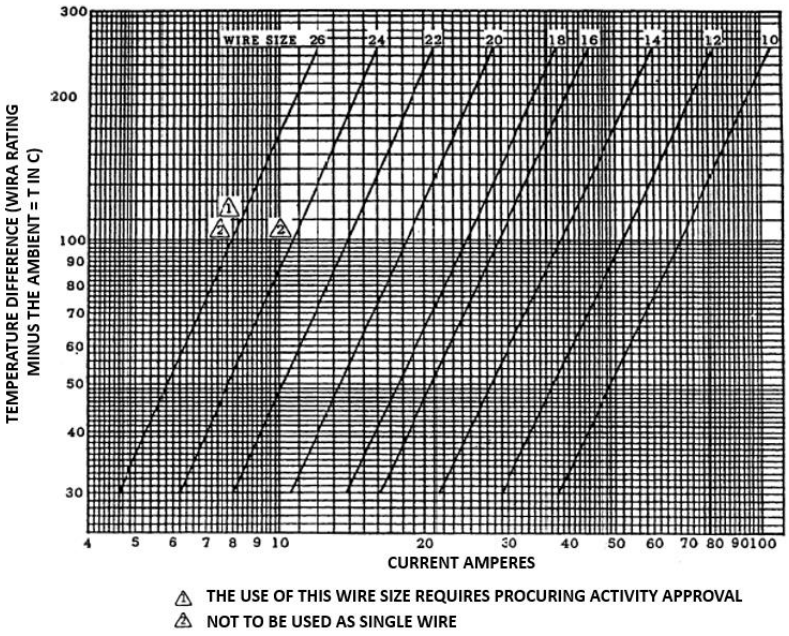

(a)

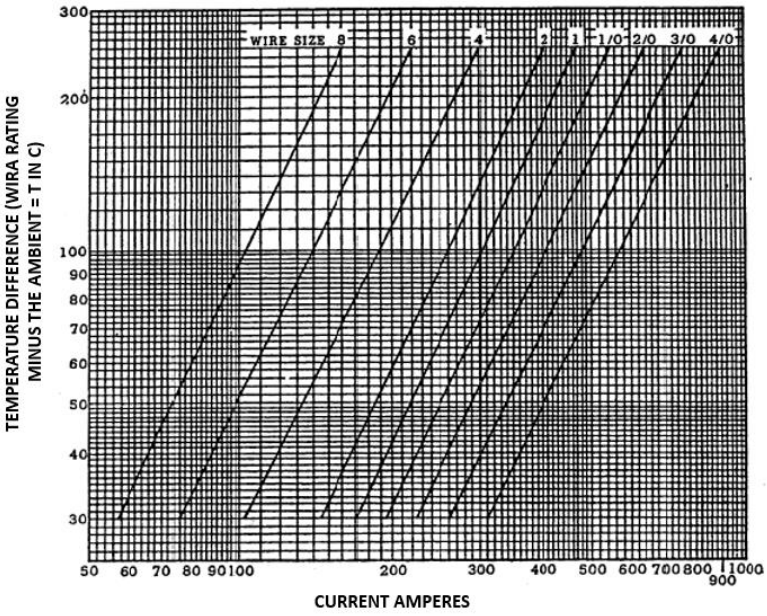

(b)

Figure 2.5 Single copper wire current rating in free air [44].

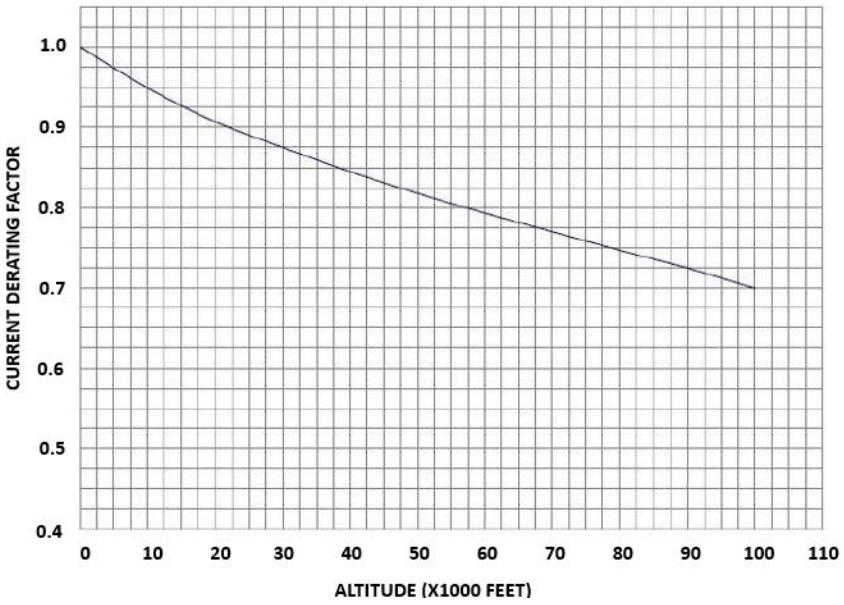

Figure 2.6 Altitude derating factor [44].

The standard states that the current rating is applicable for frequencies up to 800 Hz. However, it does not consider skin effect at all. The skin depth is calculated by Equation 2.1 [54].

$$\delta = \sqrt{\frac{\rho}{\pi \times f \times \mu}} \tag{2.1}$$

where ρ is the resistivity of the conductor (Ω.m), f is the frequency (Hz) and μ is the absolute magnetic permeability (H/m).

$$\mu = \mu_0 \mu_r$$

where μ_0 is the permeability of free space with the value of $4\pi \times 10^{-7}\ H/m$ and μ_r is the relative permeability dependent on the material. For copper and aluminium, μ_r is around 1 [11].

If the conductor temperature is 200 °C, the skin depth versus frequency of round aluminium and copper conductor is shown in Figure 2.7. The skin depth is around 3 mm and 4 mm for a copper conductor and aluminium conductor respectively at 800 Hz. This means that if the conductor size is larger than AWG 2 (6.54 mm diameter) for the copper conductor and AWG 0 (8.25 mm diameter) for the aluminium conductor, the skin effect may affect the current carrying capacity. The result also suggests that AS50881 should have a skin effect correction factor when the skin depth is smaller than the conductor radius.

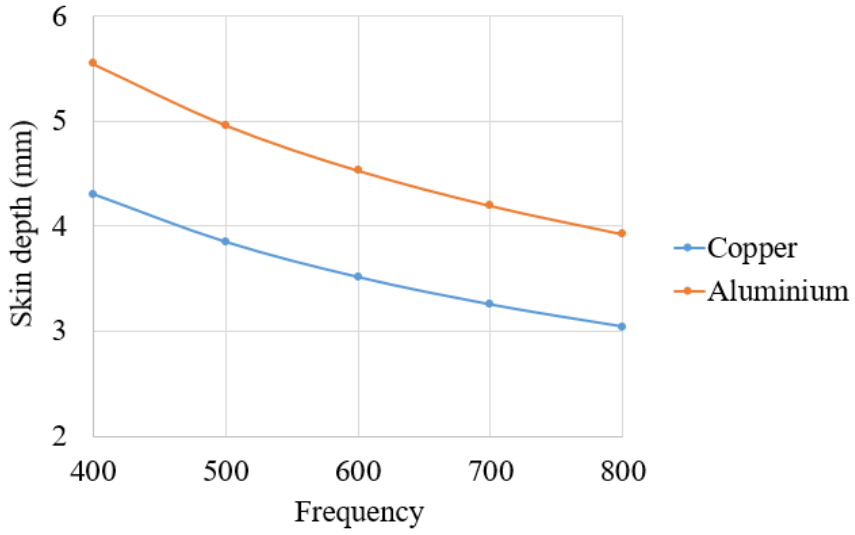

Figure 2.7 The relationship between skin depth and frequency of a solid round conductor under 200 °C.

Although SAE AS50881 has been utilised as an aircraft cable installation guide, it still has some limitations for applications. Firstly, it does not explain the principle and process for calculating the current capacity. Thus, it can be only applied to specific cable types (round, aluminium and copper conductors, sized 26 to 4/0) mentioned in the standard and cannot be applied to busbars. Furthermore, the size of cable encapsulation space is not defined, bringing uncertainty to the current rating determination. The encapsulation space can affect the convective thermal coefficient of cables and eventually affect the current carrying capacity. In addition, it does not consider the effect of insulation thickness and frequency. The increasing insulation thickness may decrease the thermal dissipation performance of cables and increasing frequency may increase power losses due to increasing resistance caused by the skin effect. Thus, there is a risk that if insulation thickness and frequency increase, the current rating guidance in the SAE AS50881 standard will be inaccurate.

Copper for Busbars – Guidance for Design and Installation

Copper for Busbars - Guidance for Design and Installation provides the current carrying capacity design of busbars at atmospheric pressure [41]. The current carrying capacity of busbars is limited by the working temperature of the busbars and the equipment connected to them. There are two types of temperature limits used in design. One is the permitted temperature, which considers safe operation. The other is the temperature rise, which considers the lowest life time cost [41].

For busbars, heat is generated by the load current through the conductor, which is dissipated by convection and radiation through its surface. Conduction is negligible since there is no heat flow out of the bar of uniform temperature. Conduction only needs to be considered when heat flows longitudinally out of the busbar system to adjacent parts with cooling capacity. This standard summarises empirical equations of convection and radiation heat losses for busbars under various temperature rises and shapes. Figure 2.8 shows the convection and radiation losses for a vertical surface at atmospheric pressure with various temperature rises and surface heights assuming a surface emissivity of 0.5 and an ambient temperature of 30 °C [41]. When surface height increases, the ratio of radiation to the total thermal dissipation increases. In addition, increasing temperature leads to both higher convective and radiative heat dissipation.

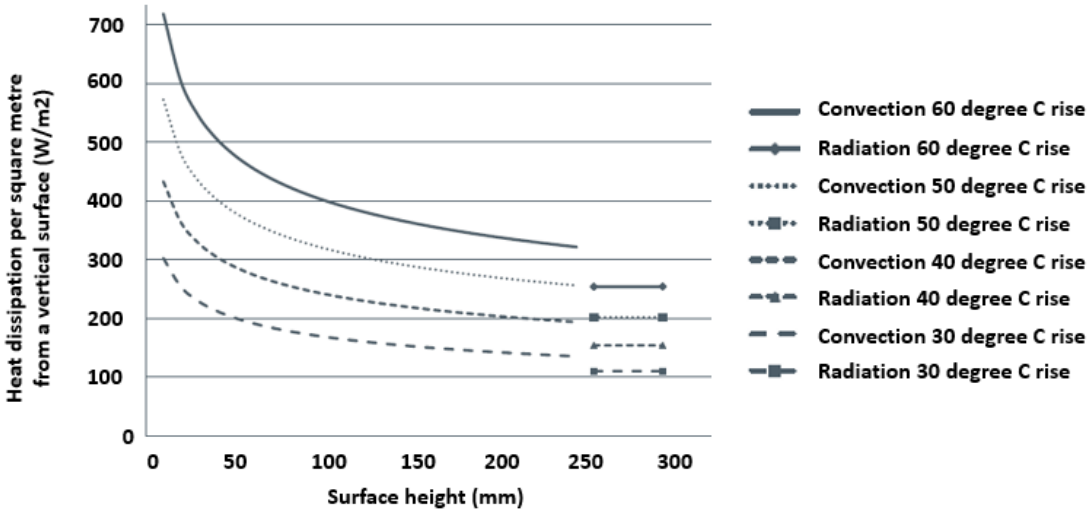

Figure 2.8 Convection and radiation losses as a function of temperature and surface height assuming relative emissivity of 0.5 and 30 °C ambient temperature [41].

This standard provides guidance for the current-carrying capacity design of busbars based on heat generation and thermal dissipation. However, it does not analyse the effect of parameters such as temperature rise and conductor shape on current carrying capacity. Moreover, this standard is used for busbars in ground power systems at atmospheric pressure, with low pressure operation conditions not considered.

2.3.2 Analytical Method Based Studies

Analytical methods are generally based on thermal equilibrium balances to determine the current carrying capacity - the thermal generation rate is equal to the thermal dissipation rate to maintain a stable temperature in the interconnection system [47, 55].

When current is circulating through a conductor, joule loss is generated and can be described as Equation 2.2:

$$W = I^2 R \tag{2.2}$$

where W is the heat loss (W), I is the current through the conductor (A) and R is the AC resistance considering the effect of temperature and electromagnetic field (Ω).

For DC systems, the resistance can be calculated from the resistivity and the operating temperature. The DC resistance varies with temperature since the resistivity changes with temperature as in Equation 2.3:

$$R_{DC} = \frac{\rho l}{A}[1 + \alpha(T - T_0)] \tag{2.3}$$

where R_{DC} is conductor resistance (Ω), ρ is conductor resistivity (Ω · m), l is the conductor length (m), A is the conductor cross-section area (m^2), α is the temperature coefficient at the reference temperature (K^{-1}), T is the conductor temperature (K) and T_0 is the reference temperature (K).

For AC systems, the alternating current generates an alternating magnetic field inside the conductor that circulates around the centre of the conductor, which induces a circulating current and the current density increases around the outer surface and reduces in the centre. This phenomenon is called the skin effect [41]. For multiple phase systems, circulating current caused by the magnetic field generated by surrounding conductors also increases conductor resistance. This is called the proximity effect [41]. The AC resistance of a conductor when considering both the skin and proximity effects can be expressed in Equation 2.4 [41]:

$$R_{AC} = R_{DC}(1 + y_s + y_p) \tag{2.4}$$

where R_{AC} and R_{DC} are the AC resistance (Ω) and DC resistance (Ω) respectively at the maximum operating temperature, y_s is the skin effect factor and y_p is the proximity effect factor.

Conduction occurs between two contacted items with different temperatures through collisions between contacting atoms or molecules [56]. Conduction is an important mechanism of heat transfer in a cable as heat must conduct through the insulation to reach the surface. Generally, it is assumed that there is a perfect contact heat transfer between different layers. The conduction process is expressed in Equation 2.5 [56]:

$$q_{cond} = -k\frac{dT}{dx} \tag{2.5}$$

where q_{cond} is the heat flux density (W/m^2), k is the thermal conductivity (W/(m·K)) and $dT/\,dx$ is the temperature gradient (K/m).

Convection is a heat transfer process between a boundary surface and a moving fluid caused by the temperature difference between the surface and the fluid. Convection is caused by two main mechanisms. The first is heat transfer through conduction in the no-slip boundary. The second is the fluid movement along the surface [56]. Convection heat transfer is normally described as being natural convection or forced convection. Natural convection is caused by buoyancy forces arising from density variation caused by temperature changes in the fluid. Forced convection is caused by external forces such as fans, creating an induced convection flow. The convective heat transfer rate can be expressed as Equation 2.6 [56]:

$$q_{conv} = h_{conv}\Delta T \tag{2.6}$$

where q_{conv} is the convective heat transfer rate (W/m^2), h_{conv} is the convective heat transfer coefficient (W/(m^2·K)) and ΔT is the temperature between fluid temperature and object surface (K).

The convective heat transfer coefficient can be calculated by the dimensionless Nusselt number (N_u), as described in Equation 2.7 [57]:

$$h_{conv} = \frac{N_u k}{D} \tag{2.7}$$

where k is the air thermal conductivity of the fluid (W/(m·K)) and D is characteristic length, which is the diameter of the cylindrical conductor (m).

For free convection, the N_u is related to Rayleigh number (Ra_D). Rayleigh number can be expressed as Equation 2.8 [57]:

$$Ra_D = \frac{g\beta D^3(T_1 - T_2)}{\nu\alpha} \tag{2.8}$$

where g is the acceleration due to the gravity (m/s^2), β is the volume expansion coefficient of fluid (K^{-1}), ν is the kinematic viscosity (m^2/s), α is the thermal diffusivity of fluid (m^2/s), T_1 is the surface temperature (K) and T_2 is the ambient temperature (K). All the thermophysical properties of air should be evaluated at the film temperature $(T_1 - T_2)/2$.

Figure 2.9 shows the relationship between the Nusselt number and Rayleigh number for free convection in horizontal cables assuming there is a laminar flow for convection. Both experimental results in [57] and the empirical equations in [58-61] are compared, with the results showing that both numbers decrease with pressure, leading to a smaller convective heat transfer coefficient.

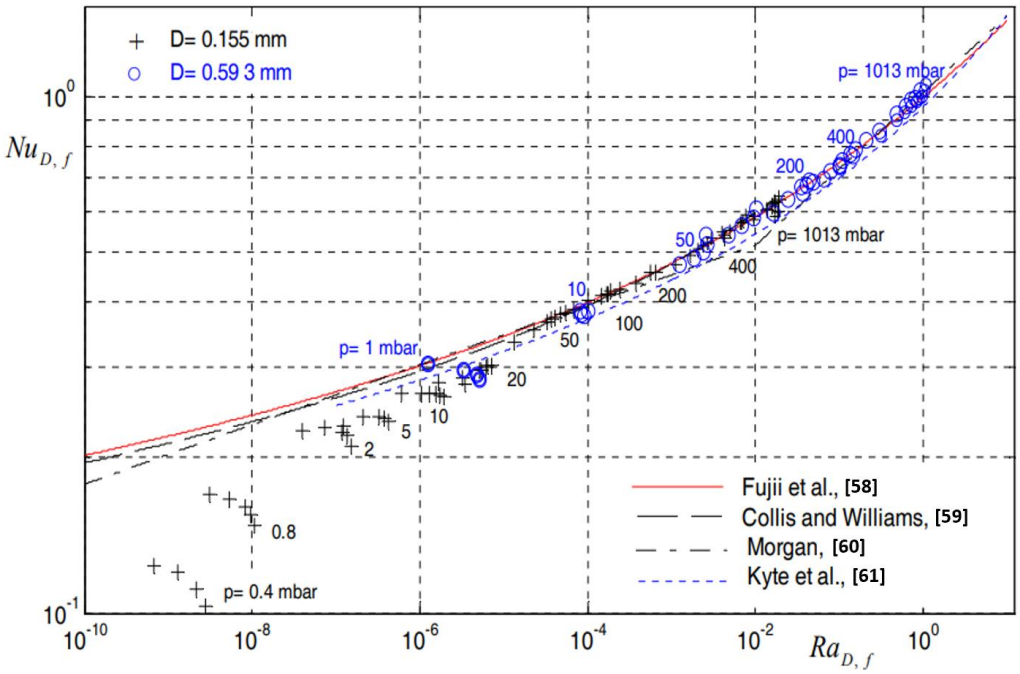

Figure 2.9 The relationship between Nusselt number and Rayleigh number for free convection of horizontal cables [57].

Thermal radiation is a heat transfer process caused by electromagnetic radiation generated by the thermal motion of particles in the material [56]. Radiation can be absorbed, transmitted and reflected at the object surface. The radiative heat transfer process is expressed using Equation 2.9:

$$q_{rad} = \sigma\varepsilon\left(T_1^{\,4} - T_2^{\,4}\right) \tag{2.9}$$

where σ is the Stefan-Boltzmann constant (approximately $5.67\times10^{-8}\ \mathrm{W\cdot m^{-2}\cdot K^{-4}}$), ε is the emissivity, T_1 is the surface temperature (K) and T_2 is the ambient temperature (K).

A graphical method to predict the steady state current capacity of single layer insulation aerospace cables was proposed in [48]. It used Equation 2.10 and 2.11 to describe the relationship between current level and insulation outer surface temperature. Equation 2.10 is based on the heat transfer process through insulation by conduction and Equation 2.11 is based on the heat transfer processes through the insulation outer surface by convection and radiation. The intersection point between the two equations is the current capacity value. The limitations of this method are that the convective coefficient as a function of cable diameter and the temperature difference between cable surface and ambient temperature has to be initially measured under various pressures, increasing the complexity to the application of this method.

$$I = \sqrt{\frac{2\pi K(T_1 - T_2)}{R_{T1}\log\left(\frac{b}{a}\right)}} \tag{2.10}$$

$$I = \sqrt{\frac{2\pi bh(T_2 - T_3) + 2\pi b\sigma\varepsilon({T_2}^4 - {T_3}^4)}{R_{T1}}} \tag{2.11}$$

where I is current of cables (A), R_{T1} is the conductor resistivity per unit at temperature T_1 ($\Omega\cdot$ m), K is the thermal conductivity of the insulation (W/(m $\cdot$ K)), T_1 is the conductor temperature (K), T_2 is the outer surface temperature (K), T_3 is the ambient temperature (K), a is the conductor radius (m), b is the overall cable radius (m), h is the convective coefficient (W/(m$\cdot$K)), σ is the Stefan-Boltzmann constant, and ε is the emissivity.

In [49], the convective heat coefficient from previous studies was used [56] and the iterative method using Equation 2.2, Equation 2.3, Equation 2.6 and Equation 2.9 was applied to calculate the current carrying capacity. The advantage of this method was to reduce the experimental cost to obtain the convective heat transfer coefficient. In [62], a Thermal Mathematical Method (TMM) based on an analytical approach, was applied to compute the temperature difference and current capacity of a single copper cable with a size ranging from AWG 24 (0.51 mm diameter) to AWG 4 (5.19 mm diameter) in a 200 mm enclosure. The resistance only depends on the temperature, with the effect

of frequency on resistance not considered. The results are consistent with the data shown in Figure 2.10. The results indicates that when the conductor size is increased, the current capacity increases under a specific temperature difference.

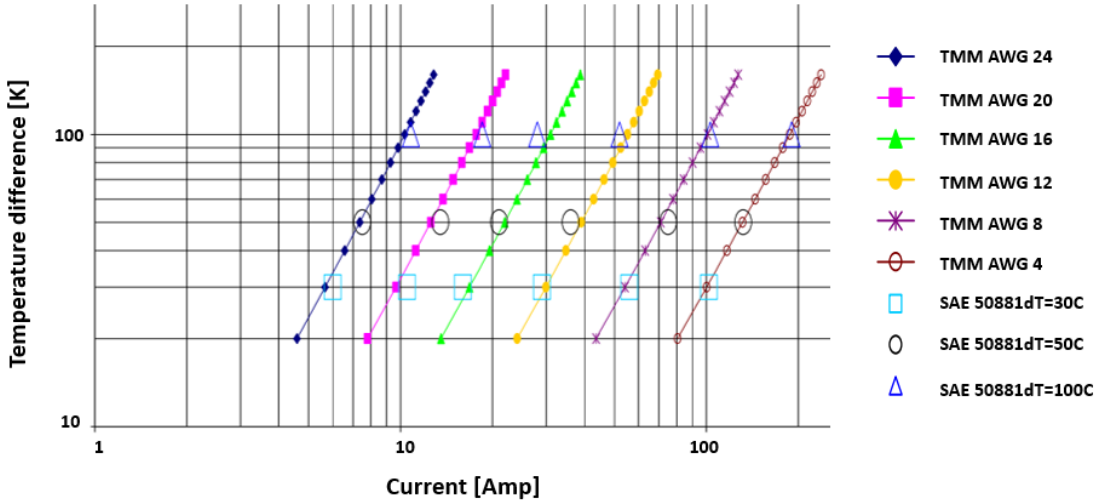

Figure 2.10. Predicted temperature difference between conductor and ambient temperature versus current for a single free copper wire with a size ranging from AWG 24 to AWG 4 compared with SAE AS50881 [62].

A thermal model based on thermal equilibrium equations was built to calculate the current carrying capacity of rectangular busbars under indoor conditions with a 30 °C rise above a 40 °C temperature [45]. The operating current was 60 Hz AC and the effect of temperature on resistivity was considered. The convection heat transfer coefficient was obtained from the empirical equation based on air thermal properties and busbar geometries [63]. The effect of busbar geometry and busbar material on the current carrying capacity were both analysed, with the results showing that material with a lower resistivity had a lower steady-state temperature and a larger cross-section area led to a higher current carrying capacity.

The analytical method can be only applied for simple geometries because the heat transfer coefficient is obtained from empirical equations or experimental results. It is difficult to ensure the accuracy of the convective heat transfer coefficient when the conductor geometry and environment conditions change.

2.3.3 Finite Element Method Based Studies

To achieve an accurate evaluation of the convective heat transfer coefficient, the finite element method (FEM) is applied by solving the governing differential equations of

heat transfer based on conservation principles, i.e. mass conservation, momentum conservation and energy conservation. It decomposes the original geometry into a finite number of small elements. The equations describing the field variables in each of the elements are enforced between neighbouring elements. An approximate solution for the equations can be determined by solving the governing equations from an initial value [64]. The advantage of FEM is that it allows the evaluation of the thermal performance under various conditions such as geometries, temperatures and pressures. Compared with the analytical method, FEM requires more computational efforts and a longer processing time.

The FEM has been widely applied to investigate the thermal performance and current carrying capacity of power cables and busbars. In [65], the steady-state thermal behaviour of cables was analysed in free air. The variation of resistance affected by temperature is considered in the model. Both natural convection and radiation through the cable surface are calculated. In [66], the cable current carrying capacity and temperature rise of three-loop power cable inside a cable trench was researched by FEM, with the effect of the layout method on the current carrying capacity also analysed. In [67-69], the temperature rise of gas-insulated busbar was predicted by FEM, with the power losses calculated by a magnetic field analysis when a 50 Hz AC current flowed into single and three phase busbars, which is used as the input value to ascertain the temperature rise for the thermal analysis. A thermal model based on the FEM has been applied to simulate the thermal distribution of busbars in a circuit breaker with a rated current of 1000 A [52].

The convective heat transfer coefficient has been calculated by FEM under various geometries and layout conditions. However, existing research only uses FEM under atmospheric pressure, with the heat transfer coefficient simulated by FEM under low pressure not yet investigated. In addition, the effect of frequency on the thermal performance of interconnection systems also lacks research. By applying the FEM to aircraft interconnection systems in aerospace environments, a more representative current carrying capacity can be predicted and a better understanding of the thermal behaviour can be obtained.

2.3.4 Experimental Method Based Studies

Figure 2.11 shows a test facility to measure the current carrying capacity of two gauges of cable (AWG 20 and AWG 26) with two types of insulation (ETFE and Teflon-Kapton-Teflon) under various temperatures and pressures [50]. The temperature inside the shroud can be maintained between -50 °C and +80 °C, with the maximum temperature across the shroud being 5 °C. A vacuum chamber was used to measure under both atmospheric pressure and vacuum conditions (1.3 e-10 atm). The DC power supply was used to provide current through the cables. The maximum errors for the measured temperature and current are ± 2 °C and ± 0.1 A, respectively. The current level was increased steeply until the cable temperature reached 200 °C and a steady state condition was achieved for at least 1 hour. The current level under the steady state condition could be regarded as the current carrying capacity of the tested cable. The current carrying capacity of AWG 20 was 25.2 A under atmospheric pressure and a 22 °C ambient temperature, which was close to the predicted current carrying capacity (24.2 A) in SAE AS50881.

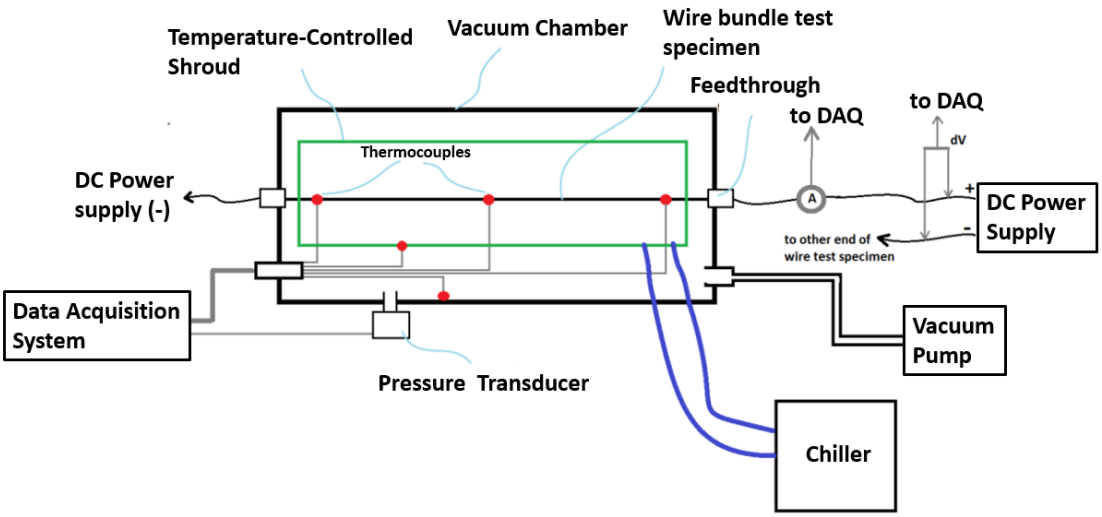

Figure 2.11. Schematic diagram of a thermal test facility [50].

Netherlands Aerospace Centre built an environment chamber to measure the thermal performance of aircraft engine cables and cable bundles [46]. The ambient temperature applied in the test was 100 °C, with both atmospheric pressure and low pressure (200 mbar) applied to test the thermal performance. The cable samples are shown in Figure 2.12 [46]. The wire size for a single wire was AWG 20 and there were 22 wires in a bundle. The temperature stability was set at 1 °C per hour.

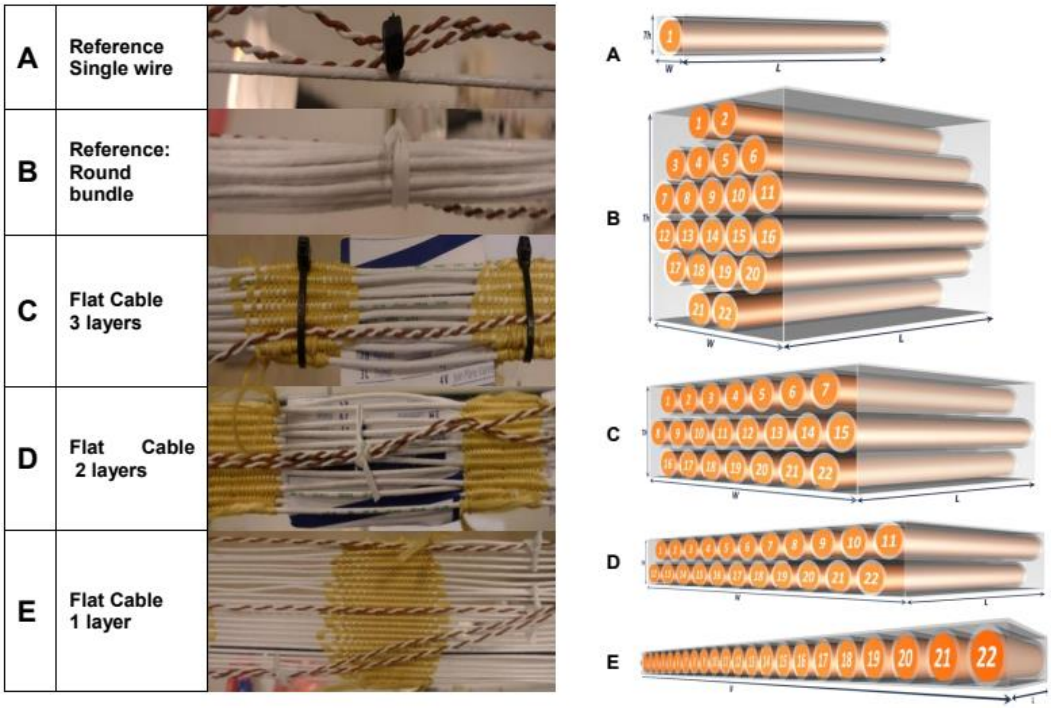

Figure 2.12 Five samples applied for thermal testing [46].

Figure 2.13 shows the measured temperature rise for five samples. The single cable had the lowest temperature rise when compared to the other samples under the same operating condition. This finding is due to the thermal dissipation of a single cable not being affected by other cables. Moreover, the flat cable bundle had a higher current rating when compared to the round bundle due to it having an increased surface area and thus enhanced natural cooling. A single layer cable can withstand 1.8 times higher current in ambient air than the round one, leading to a potential weight reduction of around 60%. Figure 2.14 shows the average pressure derating for all samples when compared with SAE AS50881. SAE AS50881 included a conservative margin of 15%.

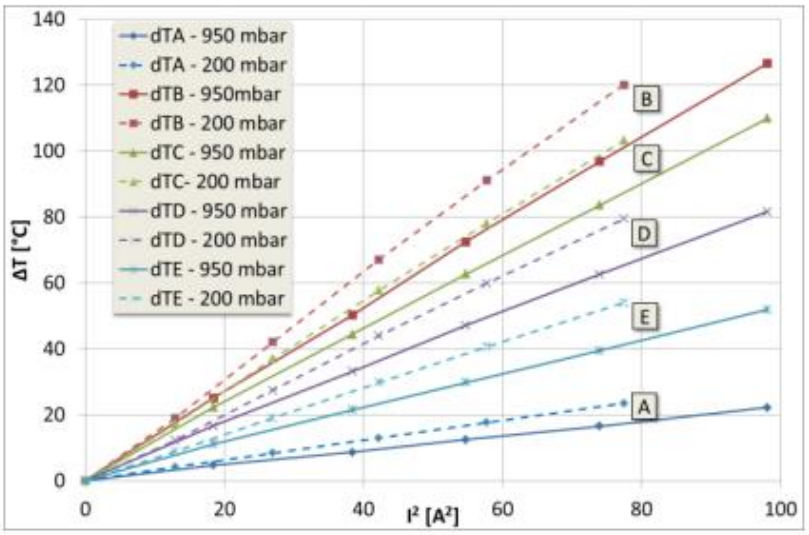

Figure 2.13. Measured temperature rise as a function of the square of the current [46].

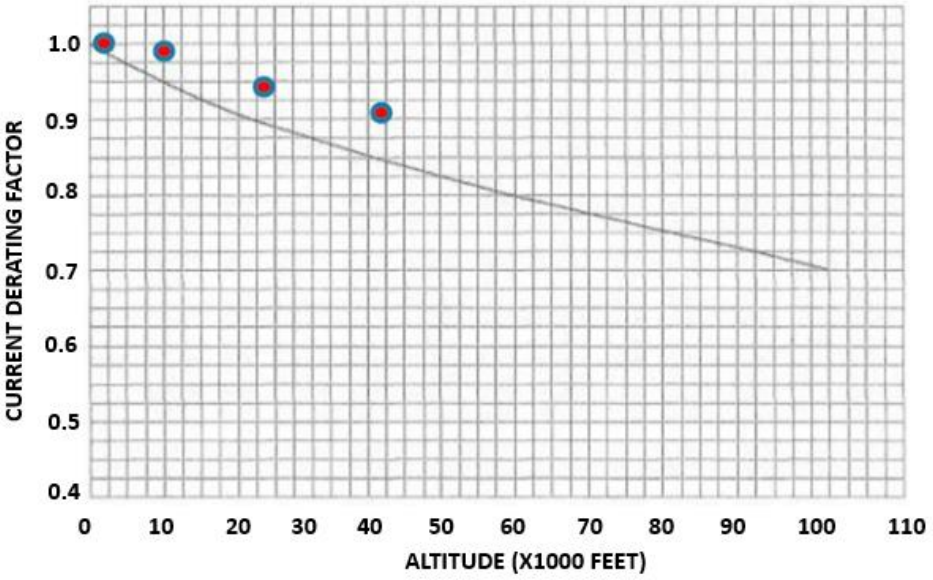

Figure 2.14. Average pressure derating for all samples compared with AS50881 [46].

2.4 Review of Safe Operating Voltage Design

2.4.1 Overview of Electrical Discharge

There are two types of electrical discharge usually occurring in aircraft: disruptive discharge and partial discharge. Disruptive discharge, also known as breakdown, is a fully bridged between the gap between two conductors with a potential difference between them. A disruptive discharge results in the flow of fault current across the gap and is usually a high energy event. A protective device is usually required to clear the fault and avoid failure of the whole system.

Disruptive discharge can occur in an air gap between two uninsulated conductors. However, in this thesis only insulated interconnection systems are considered. For existing aircraft cables, the dielectric strength of insulation material is usually magnitudes higher than that of air. For instance, the dielectric strength of PTFE is 60 kV/mm [70], meaning that an aircraft cable with 0.1 mm insulation thickness can theoretically operate up to several kilovolts (without taking into account ageing over time), which is much higher than the existing voltage in an aircraft system. However, the insulation material may degrade due to thermal and electrical aging in an aerospace environment [70]. Solid insulation is not self-restoring, with damage accumulating and leading to defects like cracks through thermo-mechanical ageing processes that can lead to oxidation, embrittlement and then damage from mechanical stress. As a result, the dielectric strength of the insulation material can be reduced leading to premature failure of the insulation system [70].

However, unscreened cables are usually limited because of partial discharge. This is a localised electrical discharge that does not completely bridge between two conductors. Figure 2.15 shows some common types of partial discharge in aircraft power systems, such as void discharge, corona discharge, surface discharge and discharge between cable and ground [71]. It can occur in air-filled voids, the sharp edge of a conductor, insulation surface and the air gap. For instance, the cable-ground geometry is shown in Figure 2.15 (d), if the insulation thickness is not sufficient, an electric field will build up in the air gap between the cable and the ground. Once the voltage in that air gap exceeds the breakdown voltage of the air gap, a partial discharge will take place.

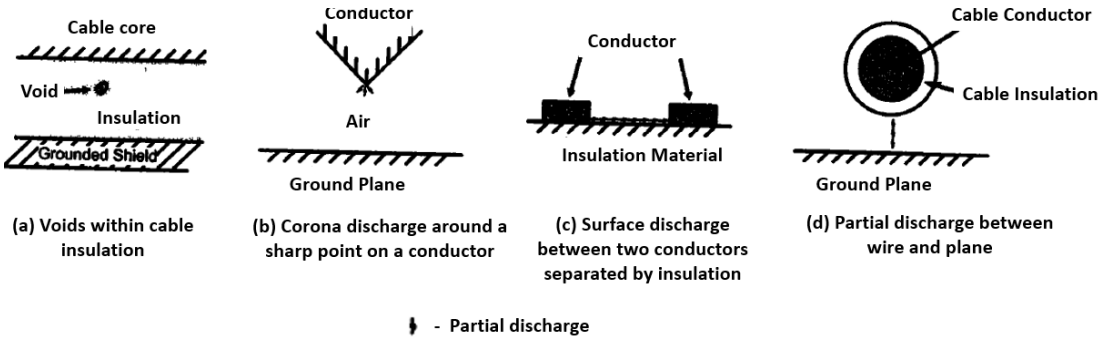

Figure 2.15 Types of partial discharge [71].

Partial discharge can degrade the insulation and shorten its lifetime, increasing the risk of the cable insulation failing [72]. Repetitive discharges cause irreversible mechanical and chemical deterioration of the insulation material as a result of the heat, ultraviolet

light and ozone produced by discharges. The degradation of insulation material can increase the electrical stress of the surrounding unaffected dielectric material and accelerate the breakdown process [70].

2.4.2 Partial Discharge Inception Voltage Calculation

The impact of pressure on partial discharge in aircraft cables is partly explained by Paschen's curve. A classical Paschen's curve is shown in Figure 2.16 [73]. It effectively describes the relationship between breakdown voltage and pressure distance product (p·d). As pressure reduces, breakdown voltage initially decreases to a minimum value and then rapidly increases. The minimum value for air is 327 V [74]. This phenomenon can be explained by the ionisation of electrons moving in the gas with different electron energies. For pd < $(pd)_{min}$, the pressure is low, reducing the possibility of collisions between free electrons and gas molecules. For pd > $(pd)_{min}$, the number of gas molecules increases, therefore this requires a higher electric field (or voltage) to increase the acceleration speed of the electron given there is a smaller distance between collisions.

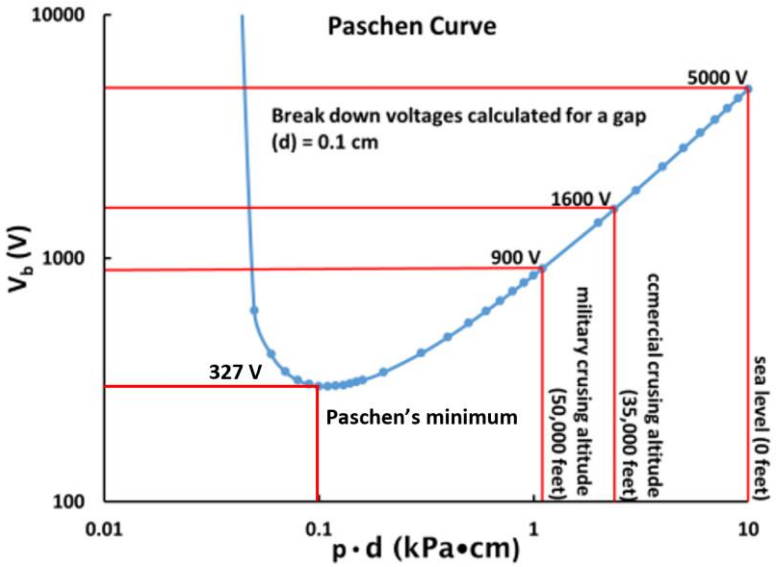

Figure 2.16 Paschen curve for air under uniform electrodes [73].

Paschen's curve describes the breakdown voltage of an air gap. It is therefore necessary to determine the applied voltage in the air gap of an unscreened cable system to determine the PDIV. The applied voltage is distributed into the insulation material and the air gap. The percentage of the voltage applied on the air gap to the applied voltage depends on insulation thickness and permittivity. If PDIV can be calculated, it can be used to determine the safe operating voltage of the insulation system given it will be

much lower than the voltage at which disruptive discharges occur [22]. Halleck proposed a method to calculate the PDIV of unscreened cables based on the minimum breakdown voltage of the air gap between a high voltage cable and the ground [75]. In this method, the cable insulation and the air gap can be regarded as two capacitors as displayed in Figure 2.17. The voltage is distributed in two capacitors depending on the thickness and dielectric constant of the capacitors.

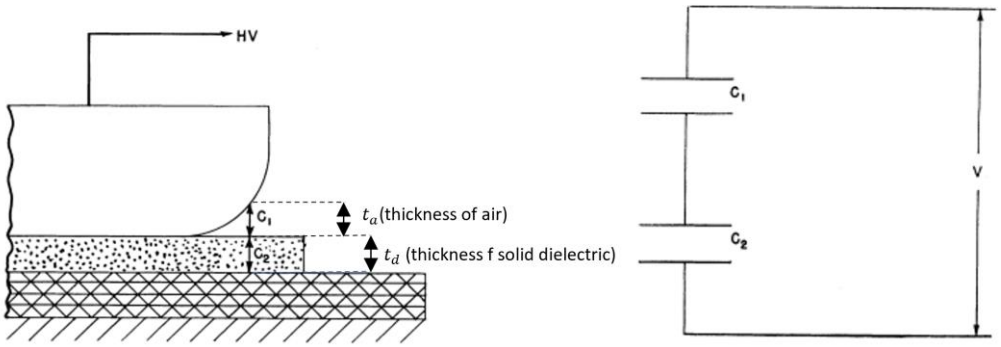

Figure 2.17 Two equivalent capacitors of air gap and insualtion between high voltage and ground electrodes [75].

The relationship between the applied voltage and the voltage in the air is expressed using Equation 2.12:

$$V = V_a(1 + \frac{t_d}{\epsilon_d t_a}) \tag{2.12}$$

where V is the applied voltage (V), V_a is the voltage applied in the air (V), , t_d is the thickness (m) and ϵ_d is dielectric constant of the insulation material. t_a is the thickness of air (m).

According to Paschen's curve, under specific pressure, the breakdown voltage of air (V_a) varies in accordance with the size of the air gap t_a. By varying the air gap distance, the corresponding breakdown voltage is used as V_a and the corresponding applied voltage (V) calculated using Equation 2.12. The lowest applied voltage in the system can be regarded as the safe operating voltage. Figure 2.18 shows a typical process to calculate the safe operation voltage of an aircraft cable [76], with the results showing that the minimum operation voltage is obtained under a 0.15 mm gap distance [76].

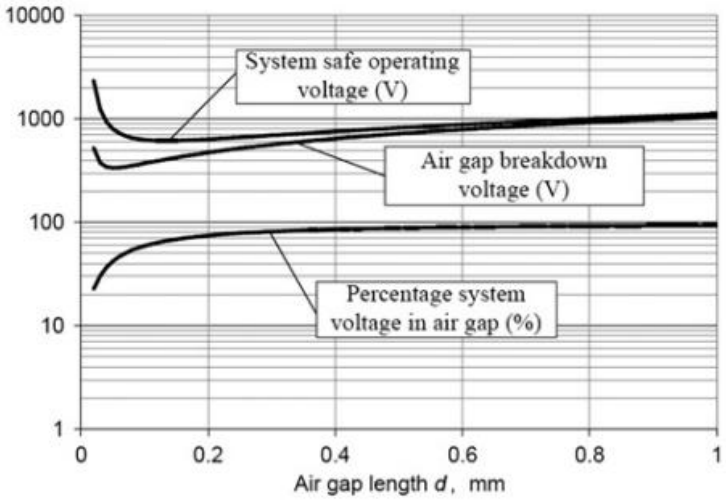

Figure 2.18 Prediction of safe operation voltage for a cable with 0.3 mm insulation thickness and relative permittivity of 4.4 under 10 kPa pressure [76].

This method has been applied to investigate the effect of insulation thickness, relative permittivity and pressure on safe operating voltage [71, 76, 77]. SAE AS50881 probably uses this method to show the relationship between PDIV and cable insulation thickness under various altitudes although there is no clear reference in the standard to confirm this. For each altitude, the effect of temperature between -50 °C and 200 °C on the PDIV is also shown in the standard [44]. The effect of temperature change can be converted to pressure change due to the mean free path of electrons being affected by air density and not pressure alone [78, 79].

The limitation of this method is that it is only strictly applicable in a uniform field [75]. The electric field is assumed to be uniform and the breakdown voltage from Paschen's curve is tested under uniform electrodes. Thus, this method is not suitable for geometries with a non-uniform field distribution, such as busbars. In addition, this method is only suitable for AC and not DC systems (given the field in a DC system is based on conductivity and not permittivity).

As an alternative, the streamer inception criterion method can be used to predict PDIV in both uniform and non-uniform fields. According to the gas discharge theory, there must be a critical number of electrons to initiate an electron avalanche. The streamer inception criterion is the integral of the effective ionisation coefficient along a electric field line is higher than a specific constant [78]. The equation can be expresses as Equation 2.13:

$$\int \bar{\alpha} dx = K \tag{2.13}$$

where $\bar{\alpha}$ is the effective ionisation coefficient of air depends on electric field, pressure and gas properties and K is a critical constant to determine if electron avalanche occurs.

The value of K is influenced by discharge conditions such as gas pressure, electric field and electrode materials. Therefore, a specific value of K suitable for all situations does not exist. For air, the majority of previous research using this method assumes K to be between 9 and 18. However, most of these values are tested under bare electrodes, which may lead to an error in the calculation of the PDIV for insulated aircraft cables. In [78], the value of K is determined to be approximately 6 for twisted insulated wires.

The method has been implemented in [78], it firstly used COMSOL to simulate the electric field strength across each electric field line in the air gap of an insulated twisted wire as shown in Figure 2.19. Then the database of gas ionisation parameters based on electric field strength and pressure was imported. Finally, the left part of Equation 2.13 was calculated for each electric field line and compared with critical constant K to determine if the partial discharge occurs.

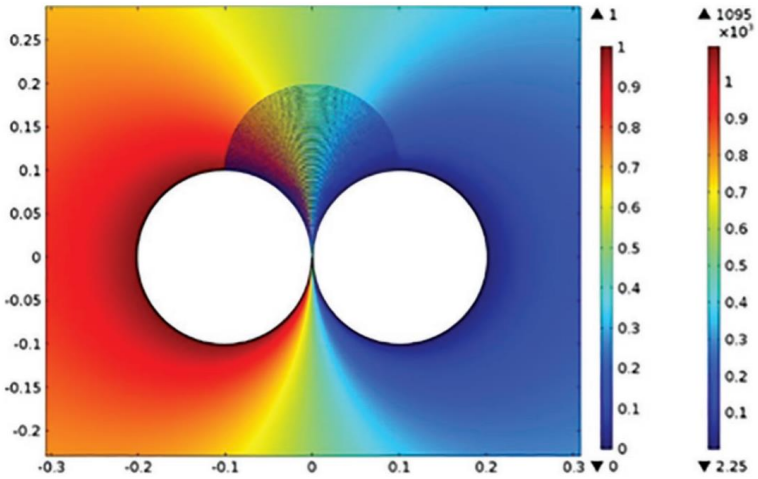

Figure 2.19 Electric Filed Simulation of an insulated twisted wire [78].

2.4.3 Stress Grading Material on Cable Termination

While the current voltage level in aircraft is relatively low compared to land-based power systems, the increasing voltage level increases the risk of partial discharge. For an unscreened system, increasing insulation thickness can increase the PDIV [75]. However, there is a conflict between increasing reliability and reducing weight and

volume. A screened cable may be a promising choice to replace conventional aircraft cable as the electric field is controlled in the insulation material that has a magnitudes higher dielectric strength than air. However, there is always a challenge in managing the electric field around the terminations of a screened cable with special cable sealing ends being required in terrestrial power systems.

The installation of a cable termination requires the partial removal insulation layer and the shield layer of the cable. This is needed to provide separation between the conductor and the earthed shield. At the edge of the shield, there are resulting high electric fields as shown in Figure 2.20 [80]. Therefore, partial discharge can occur, causing degradation of the insulation material. If the electric field is high enough, breakdown may occur and the entire system will collapse.

It is unavoidable to remove the outer layer of the cable to make connections between lines or electrical equipment. As such, in a normal power system, two cables are jointed and the space between the ground edge and conductor then filled by insulation compound. In an aerospace situation, termination may be connected to the terminal boxes and surrounded by an air gap. To ensure the reliable operation of the cable, it is likely that stress control techniques will be needed to reduce the electric field strength at the cable ends if the electric field at the sharp edges is high enough for partial discharge.

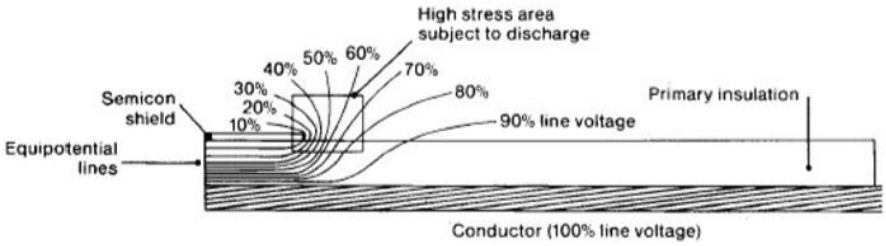

Figure 2.20 The Cable termination without stress control [80].

From previous investigations, the longitudinal electric field along the stress grading surface is used as the criterion to define the safe operating voltage. In the majority of application including cable terminations and in electrical machines (where a similar issue exists as the stress grading tape exits the stator), it is stated necessary to limit the longitudinal electric field below 0.6 kV/mm [81]. In [82], the partial discharge inception electric field strength is 0.65 kV/mm on a clean surface. The longitudinal partial

discharge inception electric field is an empirical value from experimental results or electric field simulation. Existing studies have only been conducted at atmospheric pressure.

A number of methods exist to manage the electric field at a cable termination.

Capacitive Stress Control

The refractive stress control method uses materials with high permittivity. The material is wrapped around the high electric field area. As the permittivity of the material (ε_{r2}) is higher than that of the insulation (ε_{r1}) and the surrounding gas (ε_{r3}), the electric field vector is refracted as shown in Figure 2.21 and the high electric field at the cable termination can be reduced. Refractive stress control technology is mainly applied in medium-voltage cable terminations, with the main advantage of this technology being that it can be combined with other stress control technology. The main limitation of the method is the dielectric losses in high permittivity material [83]. Therefore, the cable termination needs to be well designed in terms of heat transfer to avoid overheating especially in high-frequency situations. This may be a risk in a high-frequency aerospace application.

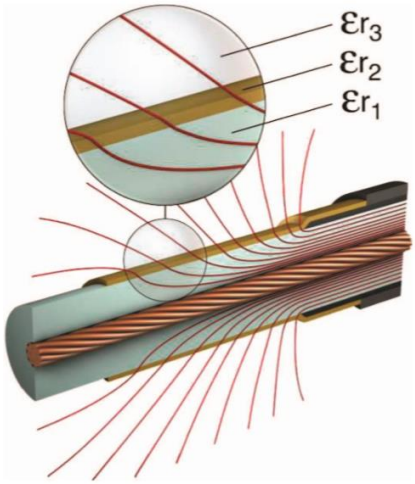

Figure 2.21 Field distribution for refractive stress control [83].

Impedance Stress Control

The impedance stress control method is a common stress control method that applies stress grading layers with a specific resistivity. As Figure 2.22 shows, an equivalent circuit under the impedance control method is analysed using the transmission line model. Distribution of the voltage can be adjusted using the impedance value. The specific impedance can reduce the highest electric field at the screen cut [84]. The

impedance stress control material is an insulation matrix with conductive additives such as carbon black particles. The concentration of conductive additives determines the conductivity of the stress control material. This method may be difficult to implement in an aircraft that operates at variable frequencies given the change in stress distribution that will take place in the equivalent network described above.

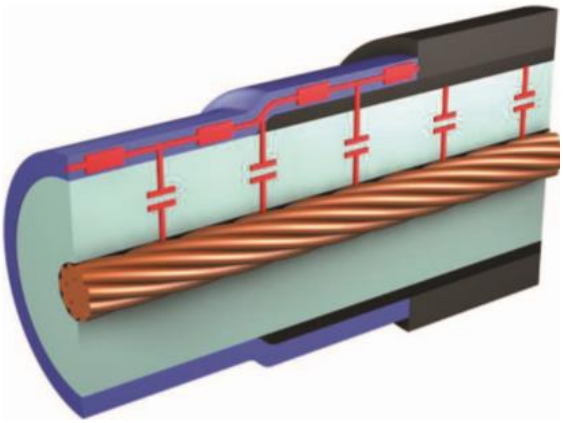

Figure 2.22 Field control using the impedance control method [83].

Nonlinear Impedance Stress Control

The state-of-the-art method for stress control at terminations is applying nonlinear material. Today, most nonlinear resistive field grading materials are composites consisting of various utility materials because one single utility material cannot achieve all the material requirements. The typical base material is polymer, which focuses on the mechanical requirements for easy processing and is used as the carrier of fillers. Fillers are used to improve the electrical properties of the base material, which are typically semiconducting materials (SiC and ZnO) [83].

When the applied electric field on the stress grading material is below a certain value, the behaviour of the stress grading material functions like insulation. When the applied electric field strength is above a certain value, the conductive path becomes active. Figure 2.23 shows the relationship between current and applied electric field strength of ZnO. After applying the stress control material over the screen cut area, the highest electric field is limited to a certain level to avoid electrical discharge.

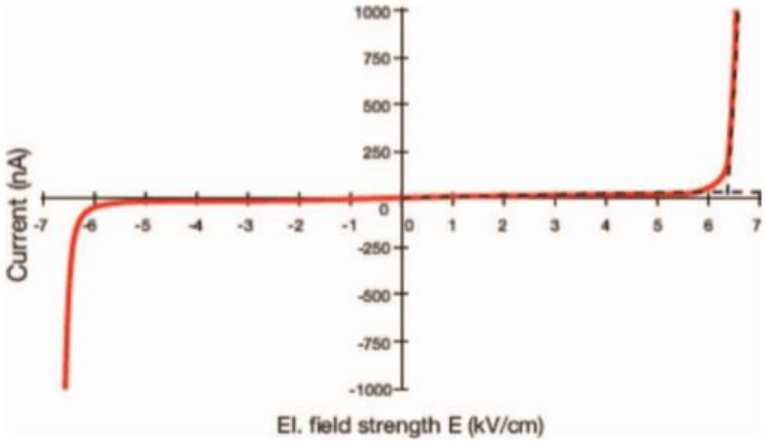

Figure 2.23 The relationship between current and applied electric field strength for ZnO [83].

To describe the properties of nonlinear field grading material, a commonly agreed model and some terminologies can be applied to describe the phenomenon. A generalised model to describe the conductivity-electric field (σ-E) characteristics has been proposed as shown in Figure 2.24 [85].

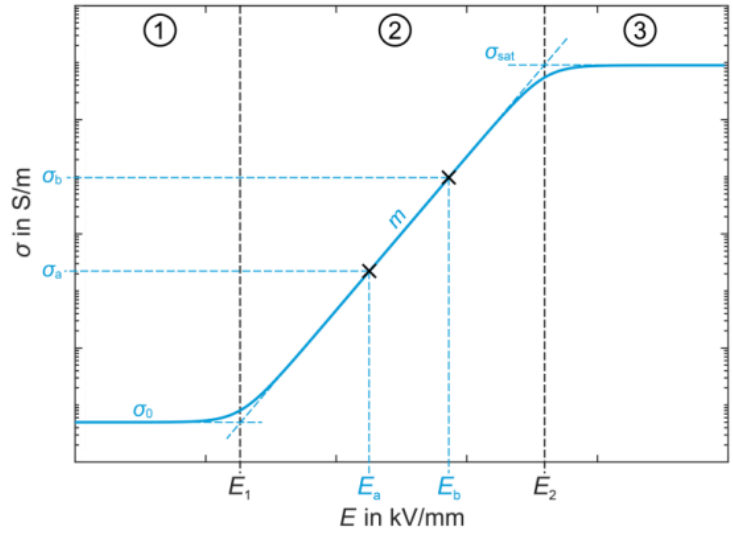

Figure 2.24 The σ-E characteristics of nonlinear field grading material [85].

When the electric field strength is low, the σ-E characteristic is usually flat. This region is usually regarded as continuous operation point and is marked as ① in Figure 2.24. The conductivity in this range is described by the term "base conductivity", σ_0.

Nonlinear material typically has a rapidly increasing conductivity above a certain electric field. When the electric field undergoes an abrupt change in conductivity, it is called “switching electric field strength”, which is E_1 in Figure 2.24.

The region that is marked as ② in Figure 2.24 is called “nonlinear region” and the degree of nonlinearity in this range is described by the exponent of nonlinearity α, which can be expressed as Equation 2.14:

$$\alpha = \frac{\lg\left(\frac{J_b}{J_a}\right)}{\lg\left(\frac{E_b}{E_a}\right)} \tag{2.14}$$

Where E_a, J_a and E_b, J_b are pair values of electric field and current density in the nonlinear region.

The nonlinear material typically shows a saturation of field dependant conductivity, which is marked as ③. The conductivity and electric field strength in this range are expressed as “saturation conductivity”, σ_{sat} and “saturation electric field strength”, E_2.

Table 2.2 summarises the conductive properties of nonlinear field grading material. The various base conductivity and nonlinearity can be applied for different situations.

Table 2.2 Nonlinear conductivity properties in the literature.

Filler	Matrix	base conductivity σ_0 S/m	switching electric field strength E_1 kV/mm	Nonlinearity α	Ref
SiC/CB	EPDM rubber	≈5×10^{-16}	≈0.22	≈4	[86]
SiC - 0.7 μm	ethylene propylene diene terpolymer (EPDM) rubber	≈5×10^{-16}	≈0.6	N/A	[87]
SiC - 3.0 μm		≈3.3×10^{-15}	≈0.3	N/A	
ZnO	silicone rubber	N/A	0.50~0.82	10~11	[88]
ZnO	silicone rubber	10^{-12}	1.5	22	[89]

For a simple stress grading system, an analytical solution of the electric field based on equivalent electric circuit is possible [90]. However, for a complex stress grading system with complex geometry or nonlinear materials, it is difficult to derive analytical solutions. The distributed network model and numerical simulation methods are used for the electric field calculation of the field grading system.

The distributed network is based on physically existing electric parameters. It can be expressed as the equivalent electric circuit consisting of lumped electric elements such as resistor, inductors and capacitors [91]. Relevant electric parameters, such as voltage, current and electric field, can be derived. It is also possible to solve the electric and thermal coupling problems. However, the disadvantage of this method is that it is challenging to accurately determine the electric element values. Numerical field simulations can be applied in complex geometry and material properties by solving the related differential equations.

Paper [92] simulated the electric field strength distribution and temperature distribution of the stress grading system of a large hydro generator under power frequency. To validate the simulation model, measurements were applied to measure the physical parameters. There are two important parameters in a stress grading system: electric field and temperature. The temperature is usually measured by thermographic cameras [93]. The electric field distribution is based on two methods. The first is measuring the potential distribution with an electrostatic voltmeter and then calculating the electric field strength using the mean electric potential difference quotient [94]. The second method is measuring the electric field strength directly using an electric field sensor [95].

2.5 Summary

This chapter initially reviewed the characteristics of existing aerospace and screened cables, followed by a discussion of the advantages of busbars over those cables. In terms of current capacity design, it described the existing standards, analytical methods, FEM models and experimental methods that have been applied to investigate the thermal performance and current capacity design of aerospace cables and busbars. In terms of safe operating voltage design, it reviewed typical electrical discharge occurring in aircraft and described the PDIV prediction methods. For screened cables, the stress grading material on its termination was summarised. Finally, previous investigations on electric field simulation of stress grading systems and partial discharge inception electric field on cable termination were reviewed.

Based on the literature review, the following research gaps can be summarised:

- In the existing standards that describe carrying capacity design of aircraft cables, only conductor size and pressure are considered. There is lack of information

about the effect of frequency and insulation thickness on current carrying capacity. In addition, the current carrying capacity of rectangular busbars under a high-frequency and low-pressure condition has not been investigated.

- FEM models can better simulate the thermal dissipation performance under complex geometries when compared to the analytical method. However, the thermal performance of cable systems using FEM in low pressure has not been described in existing literature.
- PDIV calculation methods have been applied for aircraft cables. However, their application is generally for uniform field cases. There is a lack of research on the PDIV calculation of insulated busbars, especially under low pressure. Streamer criterion method can be used to calculate busbars under low pressures.
- The performance of stress grading materials and the partial discharge inception electric field for surface discharge along cable termination have been widely studied under atmospheric pressure and power frequency (50 Hz and 60 Hz). However, the effect of two important operating parameters including pressure and frequency on them is not clear.

Chapter 3 Development of Thermal Models for Current Carrying Capacity

3.1 Introduction

Current carrying capacity is an important parameter in aircraft interconnection systems. Excessive current generates more heat losses and higher temperatures, which may cause insulation degradation and lead to partial discharge or breakdown between the conductor and adjacent systems. On the other hand, a conservative current carrying capacity increases the interconnection system weight and volume, resulting in higher fuel consumption and more GHG emissions.

With the increasing electric power in modern aircraft, both current and frequency levels may increase in the future. Existing current carrying capacity design methods are not sufficient for providing guidance, with a more accurate model needing to be developed that considers important parameters in future MEA and AEA, including frequency and insulation thickness. Furthermore, busbars have been widely applied in ground power systems due to the advantages of having higher current capacity and less weight than conventional cables [27, 96]. Therefore, the application of busbars in aircraft operating environments should also be investigated to compare their thermal performance with conventional aircraft cables.

This chapter describes the construction of a temperature rise rig, which is used to validate the thermal model based on the FEM for both cables and busbars under high-frequency (up to 2000 Hz) operating conditions. In addition, the thermal performance of the model under low pressures (0.1 bar and 0.4 bar) is validated with experimental results carried out by another researcher. The novel model can simulate the effect frequency on conductor resistance for both cables and busbars and it can also calculate thermal dissipation under various pressures. Therefore, this model can be used to investigate the effect of insulation thickness, frequency and pressures on current carrying capacity on both aircraft cables and busbars, which were not considered in existing research.

This chapter initially presents the high-frequency temperature rise test circuit and the development of the test rig, preparation of test samples and the test procedure. A thermal model is then described to simulate the temperature distribution under the same

conditions as the thermal tests. A comparison of them is then used to validate the thermal model for both cables and busbars under atmospheric pressure. Finally, validation of the thermal model under low pressures is conducted by comparing the simulation results with Milano's experimental research [57].

3.2 Thermal Test Design

3.2.1 High-Frequency Circuit Theory

The most common temperature rise test method for aircraft cables involves connecting voltage supply and tested cables in series to form a closed loop system [46, 50]. The current level can be increased by increasing the voltage level of the power supply. This test circuit is easy to build and control but can only be operated under a low current level (tens of ampere) because the power supply equipment has a limited operating current range. In [51], a compact current source can provide a current up to 2500 A by current transformer. However, this type of current source is high cost and can only operate under power frequency. Another method uses a power transformer to circulate current through test samples [97, 98]. In this method, the power supply is connected with the primary winding of a transformer and the test sample is coupled with a transformer as a secondary winding under a short-circuit condition. Compared to the first method, the current level in this method can be increased up to several thousand amperes as the current only circulates through the test samples and does not affect other equipment.

The equivalent circuit of a transformer under a short circuit condition can be regarded as a circuit consisting of resistance and inductance as shown in Figure 3.1 [99]. The inductive reactance and resistance of the transformer core can be ignored as they are much higher than the inductive reactance and resistance of the transformer winding respectively. In this circuit, r_p and x_p are resistance and inductive reactance of transformer winding on the primary side respectively. r_s and x_s are resistance and inductive reactance of transformer winding on the secondary side respectively. The symbol a is the number of turns in the primary winding divided by the number of turns in the secondary winding.

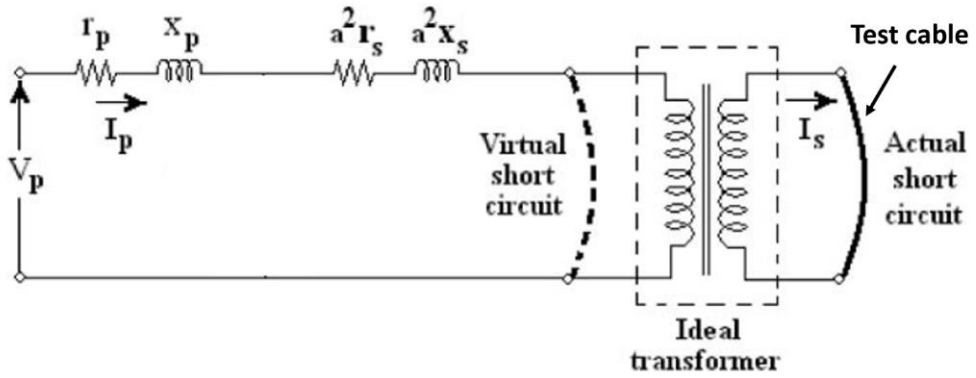

Figure 3.1 Equivalent circuit of a transformer under short-circuit conditions [99].

The impedance of the equivalent circuit can be calculated using Equation 3.1 and Equation 3.2.

$$Z = \sqrt{R^2 + {X_L}^2} \tag{3.1}$$

$$X_L = 2\pi f L \tag{3.2}$$

where Z, R, and L are respectively impedance (Ω), resistance (Ω) and inductance (H) in the circuit and f is the operating frequency (Hz).

In the circuit shown in Figure 3.1, the inductive reactance increases 40 times when the frequency is increased from 50 Hz to 2000 Hz, leading to a high impedance and the need for a power supply to provide a high level of reactive power to circulate a current through the test object. To reduce circuit impedance, capacitors can be placed in series with transformer wining on the primary side to make the circuit resonant. The impedance of a RLC circuit can be calculated using Equation 3.1 to Equation 3.4.

$$Z = \sqrt{R^2 + (X_L - X_C)^2} \tag{3.3}$$

$$X_C = \frac{1}{2\pi f C} \tag{3.4}$$

where Z, R, L and C are respectively impedance (Ω), resistance (Ω), inductance (H) and capacitance (F) in the circuit and f is the operating frequency (Hz).

When capacitance is $\frac{1}{4\pi^2 f^2 L}$, the circuit is in resonance and impedance is at a minimum. This frequency is defined as resonant frequency. For a 4 m length, single-turn circular loop of AWG 4/0 (diameter=11.68 mm) cable made of aluminium, the inductance can be calculated in Equation 3.5.

$$L = \mu_0 a \left[ln \frac{8a}{r} - 2 \right] \tag{3.5}$$

where L is inductance (H), μ_0 is permeability of free space ($4\pi \times 10^{-7}$ H/m), r is the cable conductor radius (m) and a is diameter of the circular loop (m).

The resistance of the cable is calculated in Equation 3.6.

$$R = \rho \frac{l}{S} \tag{3.6}$$

Where R is resistance (Ω), ρ is resistivity at a specific temperature ($\Omega \cdot$m), l is length (m) and S is cross-section area (m^2).

If assuming the current through the cable is 300 A under 1000 Hz and the conductor temperature is 200 °C according to [44], the resistance, inductance and capacitance for series resonance on the secondary side can be calculated using Equation 3.2 - Equation 3.6. The effect of frequency on resistance is not considered here, with the results shown in Table 3.1.

Table 3.1 Calculated impedance values of a 4 m length, single-turn circular loop cable with an AWG 4/0 conductor under a frequency of 1000 Hz and a conductor temperature of 200 °C.

Resistance (R_S)	Inductance (L_S)	Capacitance for series resonance (C_S)
$1.82 \times 10^{-3}\ \Omega$	$8.74 * 10^{-6}$ H	2.9×10^{-3} F

The current on the primary side of the transformer can be calculated by Equation 3.7.

$$I_P = \frac{N_S}{N_P} \times I_S \tag{3.7}$$

where I_P is current on the primary side (A), I_S is current on the secondary side (A), N_P is number of turns in the primary winding and N_S is number of turns in the secondary winding.

The capacitance for series resonance on the primary side can be calculated by Equation 3.8.

$$C_P = (\frac{N_S}{N_P}) \times C_S \tag{3.8}$$

where C_P is capacitance for series resonance on the primary side (H) and C_S is capacitance for series resonance seen on the secondary side (H).

The voltage on the capacitor on the primary side can be calculated by Equation 3.9.

$$V_{capacitor} = I_P X_{CP} \tag{3.9}$$

The resistivity of the cable seen on the primary side can be calculated by Equation 3.10.

$$R_P = (\frac{N_P}{N_S})^2 \times R_S \tag{3.10}$$

The output voltage of the power supply can be calculated by Equation 3.11 if the resistance of the primary windings is not considered.

$$V_P = I_P \times R_P \tag{3.11}$$

The effect of the turn ratio on the capacitance, voltage and current values on the primary side is presented in Table 3.2. When the turns ratio increases, the required capacitance decreases. It needs to be noted that the voltage level applied to the capacitors increases with the turn ratio and is magnitudes larger than that from the power supply. Therefore, suitable capacitors should be chosen to make sure the voltage applied to them is lower than their voltage ratings.

Table 3.2 The effect of turn ratio on the capacitance, voltage and current on the primary side for a constant 300A at 1kHz.

Turn Ratio (N_P/N_S)	50	100	150	200
C_P (μF)	1.16	0.52	0.19	0.072
I_P (A)	6	3	2	1.5
V_P (V)	27	54	82	109
$V_{capacitor}$ (V)	824	1650	2470	3300

3.2.2 Test Setup

The test setup diagram is shown in Figure 3.2. The power supply is provided by an amplifier controlled by a National Instrument (NI) analogue output board. A capacitor bank is connected between the amplifier and the primary side of the transformer to make sure the resonant frequency of the test circuit is close to the testing frequency. The test samples are connected as a closed loop, which is coupled with a transformer as a secondary winding under a short-circuit condition. A current clamp is used to measure the current going through the test samples. K-type thermocouples are used to

measure the surface temperature of test samples and the ambient temperature. The measurement data is recorded by LabVIEW. The test platform of an example of busbars is shown in Figure 3.3. Plastic supports are used to reduce the contact between test samples and the ground.

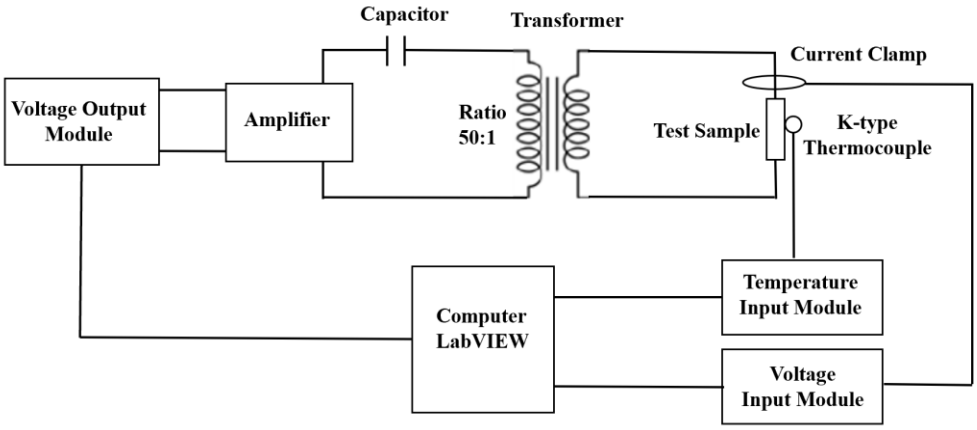

Figure 3.2 Schematic diagram of the temperature rising test.

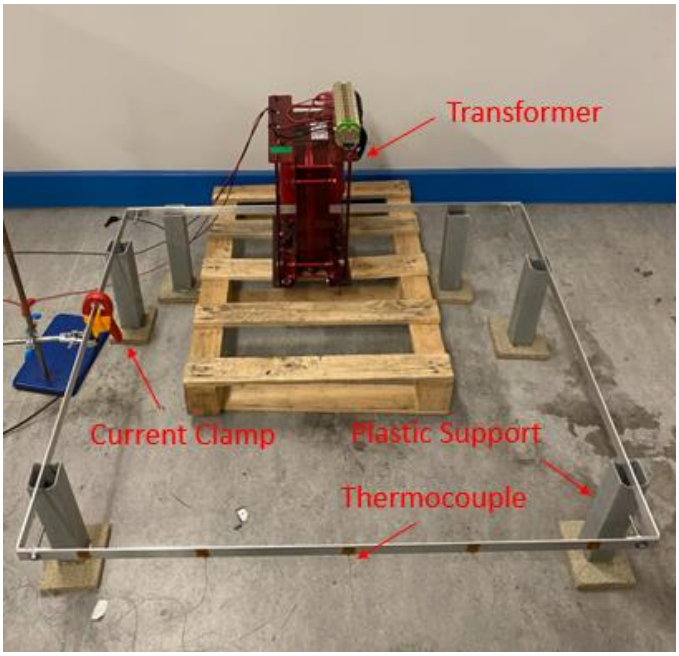

Figure 3.3 Test platform for busbars.

3.2.1.1 High-frequency Power Supply

The high-frequency current circulating the test sample is achieved with three main parts: a variable-frequency sinusoidal voltage source, a capacitor box and a transformer. In the voltage output part, a sinusoidal voltage signal is generated by NI 9263 with a magnitude range between -10 V and 10 V [100]. The frequency of the voltage signal can be adjusted in LabVIEW. The sampling rate of the output voltage signal was set as

100 kS/s. An amplifier, American Audio V6001 Plus, was connected in series to amplify the voltage signal from NI 9263 and output it to the transformer. The amplifier can provide an output power up to 5000 W and an output voltage up 141 V [101]. The total harmonic distortion is less than 0.03% between 20 Hz and 20 kHz, meaning that the amplifier can output an accurate sinusoidal voltage waveform obtained from NI 9263.

KEMET PHE426 Film capacitors were used to build up a capacitor bank as shown in Figure 3.4. The capacitor is 4.7 µF with 5% uncertainty. Its voltage rating is 160 VAC (although the capacitors were successfully operated at voltage levels much higher than this). The desired capacitance value can be obtained by connecting the capacitors in series or parallel. The capacitance should make the circuit resonant frequency close to the test frequency and ideally ensure the voltage level applied on the capacitor is below its rated voltage.

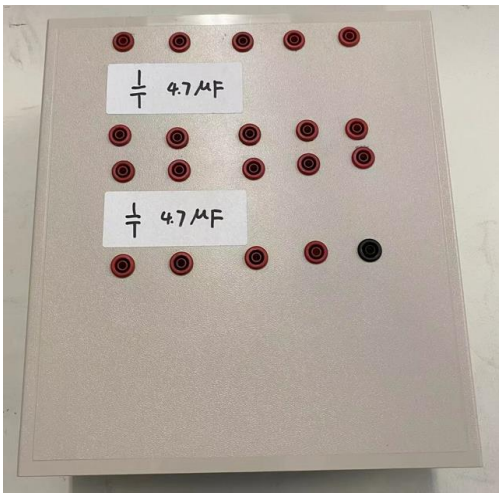

Figure 3.4 Capacitor bank.

A Boardman test transformer was used to generate a high circulating current through the test sample. It has a power rating of 3000 VA and working frequency range from 400 Hz to 2000 Hz. It has eight 25-turn coils on the primary winding that can be connected in series / parallel. In this work, two coils in series were used to provide 50 turns. The secondary winding was removed and the test samples used as the single turn in the secondary winding.

3.2.2.2 Data Measurement and Processing

The current passing through the test samples was measured by current clamps, including Fluke i400s and Fluke i3000s. The current clamp measured the current and

output voltage at a rate of 1 mV/A. The voltage data was measured by voltage input module NI 9215 with a sampling rate of 50 kS/s. It was then processed to a Root Mean Square (RMS) value and recorded by LabVIEW. The measurement uncertainty for the current clamp is 1% and the reading uncertainty for the analogue input module NI 9215 is 0.02% [102].

The test samples' surface and ambient temperatures were measured by K-type thermocouples and thermocouple temperature data logger Pico TC-08 shown in Figure 3.5. The working temperature range of K-type thermocouples applied in the test was -70 and 250 °C [103]. The sampling rate for both surface temperature and ambient temperature was set as 1S/s. An alarm system was designed so that the system can be stopped once the measured temperature is above 250 °C. The measurement accuracy of the K-type thermocouple is ±1.5 ºC and the reading accuracy of Pico TC-08 is ±0.5 ºC [104].

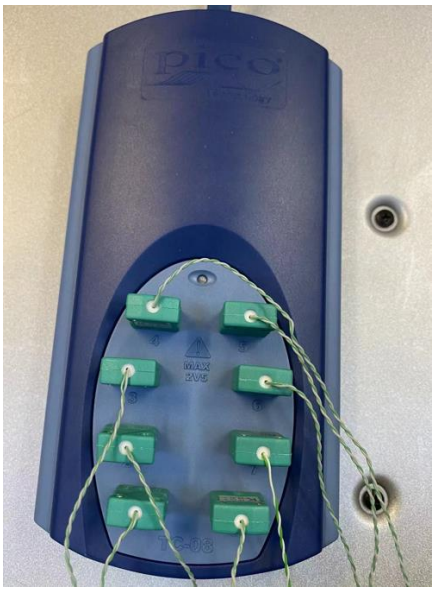

Figure 3.5 K-type thermocouples connected to Pico TC-08.

The layout of the thermocouple on the sample surface is presented in Figure 3.6 (a). The thermal paste ensures contact between the thermocouples and test samples. Kapton tape was then used to fix the position of each thermocouple. Five thermocouples were applied to measure the conductor temperature (described in detail in Section 3.2.4). The layout of the thermocouples used to measure the ambient temperature is presented in Figure 3.6 (b). Each thermocouple was immersed in mineral oil to eliminate temperature fluctuation caused by random factors, such as people's movement in the laboratory. One thermocouple used to measure the ambient temperature was placed 2

meters away from the test setup to avoid the effect of heat dissipation caused by the test setup.

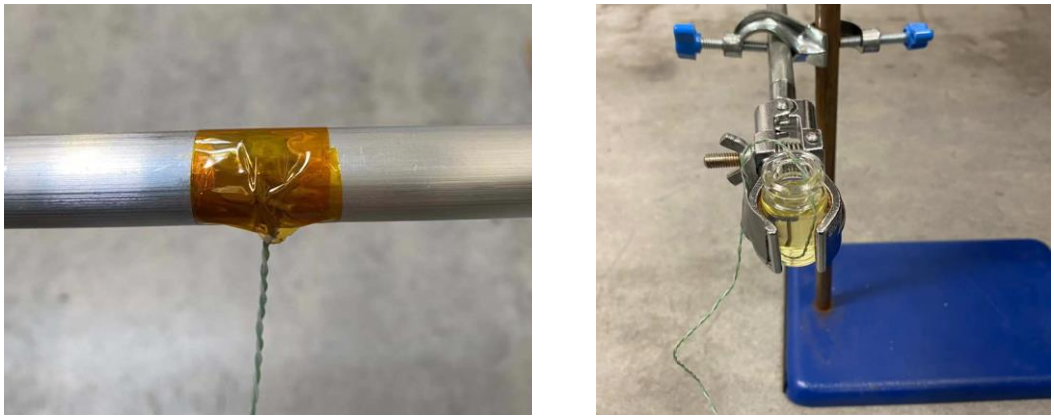

(a) (b)

Figure 3.6. Layout of thermocouples used to measure (a) the sample surface temperature. (b) the ambient temperature.

3.2.3 Test Samples

In this programme, aluminium 6082-T6 rods/busbars were used to model a simple aerospace cable with the same cross-section area. Figure 3.7 shows the cross-section of four types of rods and busbars used in the test. The length for all four samples is 1 m, with their cross-section areas shown in Table 3.3. The 10 mm rod and the 25*3 mm busbar have a similar cross-section area, as do the 15 mm rod and the 30*6mm busbar.

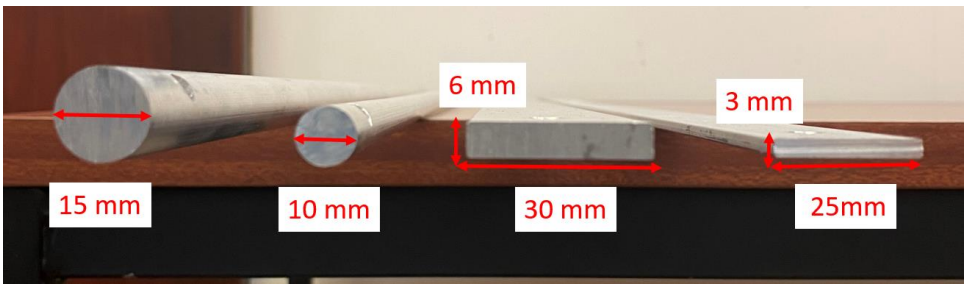

Figure 3.7 Cross-section diagram of Aluminium rods and busbars.

Table 3.3 Dimension of rods and busbars

Rods		Busbars	
Diameter (mm)	Cross-section area (mm^2)	Dimension (mm)	Cross section area (mm^2)
10	78.53	25*3	75
15	176.71	30*6	180

Both horizontal and vertical positions of busbars were tested. In the rest of the thesis, a horizontal busbar means the longer side of the busbar is in the horizontal position (30*6 mm busbar and 25*3 mm busbar) and a vertical busbar (6*30 mm busbar and 3*25 mm busbar) means the longer side of the busbar in the vertical position as shown in Figure 3.8.

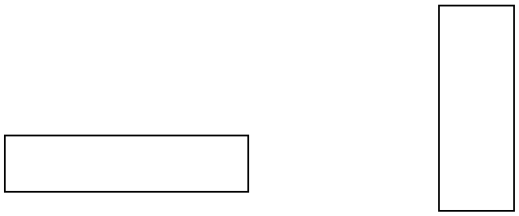

Horizontal busbar Vertical busbar

Figure 3.8 Example of horizontal and vertical busbars.

In order to connect the rods/busbars as a square, M6 holes (6 mm diameter) were threaded at the end of the rods/busbars at a distance of 25 mm from the end as shown in Figure 3.9.

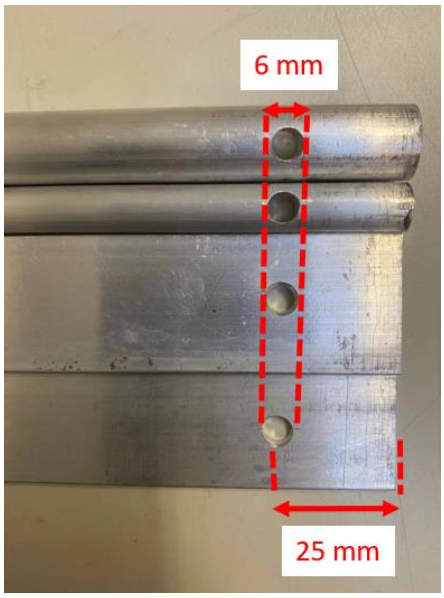

Figure 3.9 M6 holes threaded at the end of rods/busbars.

In order to connect busbars in vertical positions, the busbar end was bent 90 degrees as shown in Figure 3.10.

Figure 3.10 Bending at the end part.

3.2.4 Test Procedures

The experiment was carried out using the procedure shown in Figure 3.11. The details of each step are described in the following.

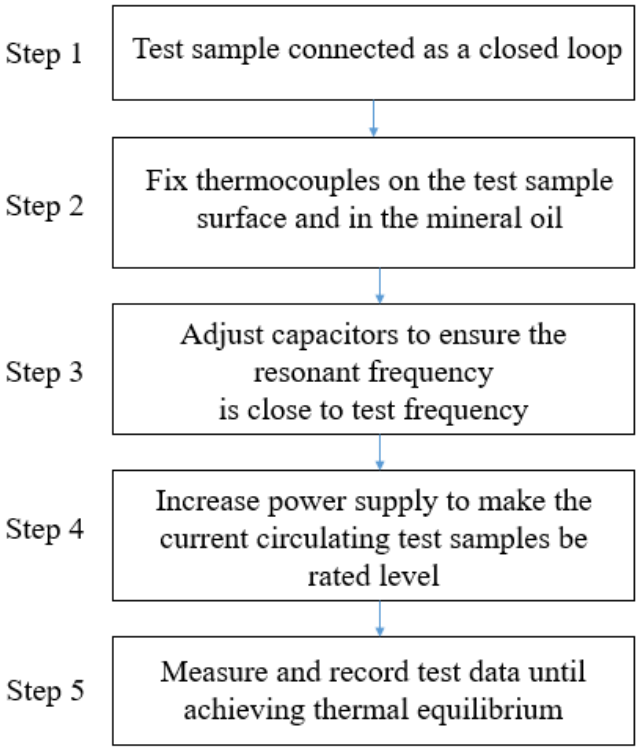

Figure 3.11 Test procedure.

- **Test Sample Preparation**

Four samples were connected to form a square loop as a secondary winding of the transformer. The temperature of the sample farthest from the transformer was measured.

- **Thermocouple Layout**

Five thermocouples were applied to measure the conductor surface temperatures as shown in Figure 3.12.

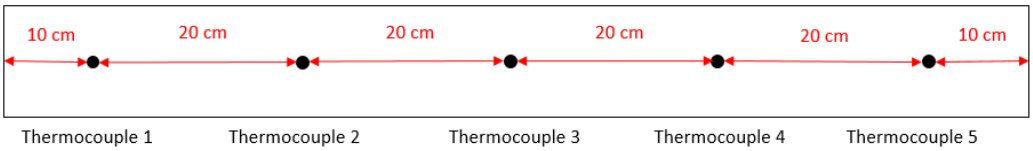

Figure 3.12 Position of thermocouples.

- **Suitable Capacitance**

The suitable capacitance values for different samples under the frequencies between 500 Hz and 2000 Hz are shown in Table 3.4.

Table 3.4 Suitable capacitance for the four samples.

	Capacitance / uF			
Test Frequency / Hz	10mm Rod	15mm Rod	25*3 mm busbar	30*6 mm busbar
500	11.75	11.75	11.75	11.75
1000	2.82	2.82	2.82	2.82
1500	1.26	1.34	1.26	1.34
2000	0.67	0.78	0.67	0.78

Figure 3.13 shows the relationship between frequency and current for the 30*6 mm busbar when the capacitance is 2.82 μF and the voltage output is constant. The resonant frequency for the circuit is around 1000 Hz. Similar procedures were applied to obtain suitable capacitances for all samples under various frequencies.

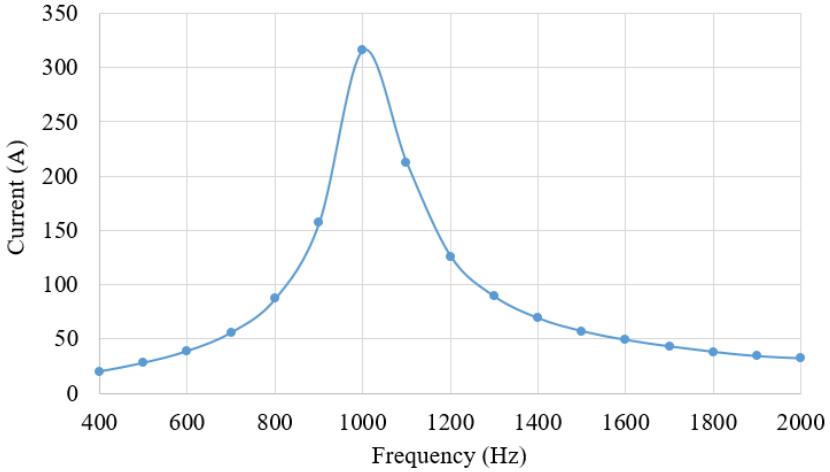

Figure 3.13 Current versus frequency at a constant voltage output for the 30*6 mm busbar.

- **Thermal Equilibrium**

The relationship between the conductor temperature and test time of the 25*3 mm busbar under a current of 400 A and a frequency of 1000 Hz is presented in Figure 3.14. The temperature reaches stability within 30 minutes (stability being defined as when the temperature fluctuation compared to the previous minute is less than 1%). The other samples, such as the 10 mm rod, 15 mm rod and 30* 6 mm busbar, also achieve thermal equilibrium after a similar test time. Thus, the test time is selected to be 60 minutes, with the average results of the last 10 minutes used as the conductor temperature. Due to changes in the ambient temperature, the temperature rise of the conductor over the ambient temperature is used for the thermal performance analysis.

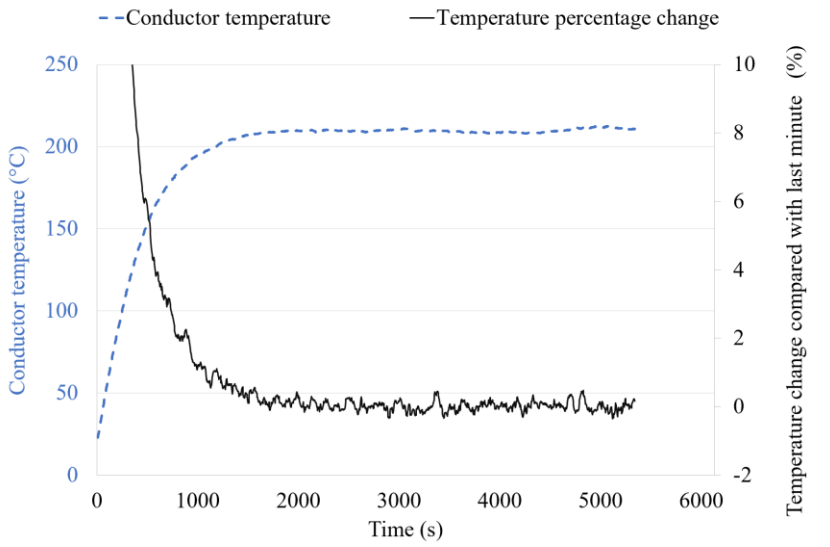

Figure 3.14 Conductor temperature versus test time.

The temperature distribution of the five thermocouples is shown in Figure 3.15. It can be found that the conductor temperature at the end of the test sample is lower compared with the other three positions. The temperature at the end part is more complex to analyse as it is affected by many factors, such as contact resistance, airflow around the connection area and proximity effect. The three thermocouples in the centre position (thermocouple 2, thermocouple 3 and thermocouple 4) are used for analysis as these best reflect the worst case scenario in a cable.

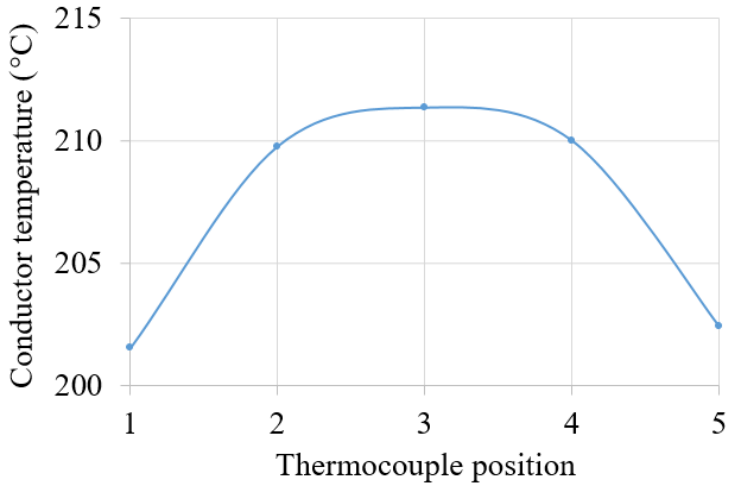

Figure 3.15 The distribution between temperature and thermocouple position.

3.3 Thermal Model Design

COMSOL Multiphysics is a FEM software that can model multi-physics systems such as electrical, fluid flow and heat transfer. In this section, the thermal model is built by COMOSL Multiphysics 5.4. This model is based on FEM by solving the governing differential equations of heat transfer based on conservation principles, i.e. mass conservation, momentum conservation and energy conservation. The temperature distribution of cables and busbars under steady the state condition can be simulated. The model can be applied to investigate the effect of model geometry, material properties and operating conditions in future electric aircraft on thermal distribution of both cables and busbars.

3.3.1 Model Geometry and Material

The 2D thermal model consists of two parts, the test sample and surrounding air, which is shown in Figure 3.16. The geometry of the interconnection system is the same as the test samples shown in Section 3.2.3. There are four samples: 10 mm rod, 15 mm rod,

25*3 mm busbar and 30*6 mm busbar. Both busbars were placed in both horizontal and vertical directions for comparison. The distance between the test sample and ground was 0.25 m, the same as the test condition. The height and width of the air domain was set at 2 m and is explained in Figure 3.19. The model assumes the conductor is isolated in free space.

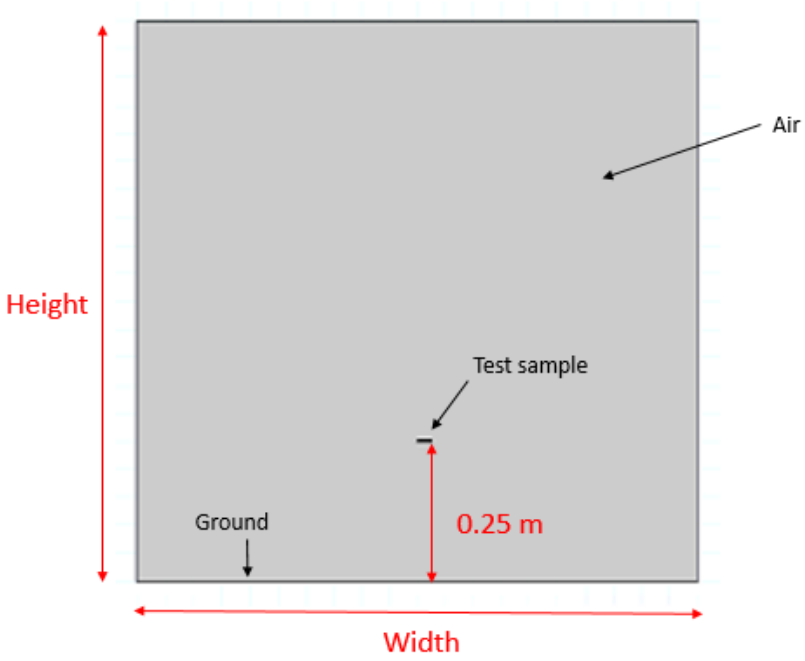

Figure 3.16 Model geometry.

There are two materials in the model: the test sample material is aluminium alloy and the surrounding gas is air. The general material properties of air and aluminium required for the thermal model calculation (e.g. thermal conductivity, density and heat capacity and surface emissivity) were taken from Haynes [105]. To make the model accurate, both the resistivity and temperature coefficient of the test samples need to be measured. The resistances of the four test samples with a length of 80 cm were initially measured to obtain the resistivity at room temperature (around 25 ^{o}C). The test circuit is shown in Figure 3.17. The four-wire measuring instrument CROPICO Microhmmeter DO500 with an uncertainty of 0.03% was used to measure resistance, eliminating the effect of connection wire resistance [106]. The advantage of this connection method is that the measured resistance is not affected by the resistance of the connection wire between test samples and test equipment. The resistivity can be calculated using Equation 3.12.

$$\rho = \frac{S}{RL} \tag{3.12}$$

where R is resistance (Ω), L is length (m), ρ is resistivity at the reference temperature (Ω/m) and S is cross-section area (m^2).

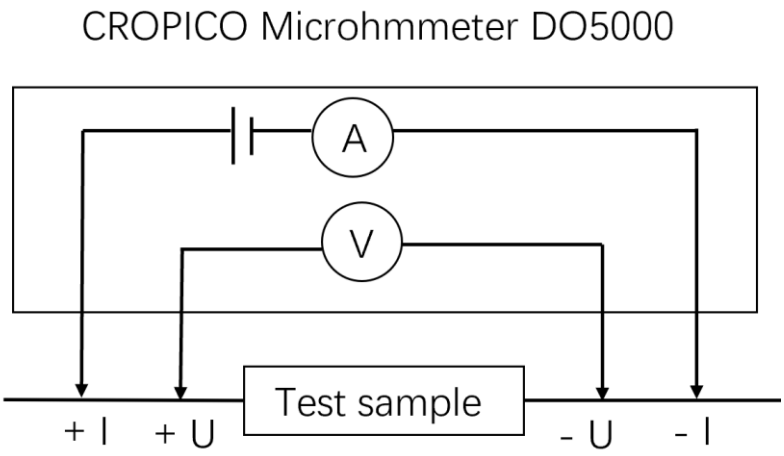

Figure 3.17 Resistance measurement circuit.

The resistivity of the four test samples at a length of 0.4 m were measured from 25 °C to 80 °C to calculate the thermal coefficient. The temperature coefficient can be calculated by Equation 3.12 and Equation 3.13.

$$\rho = \rho_0[1 + \alpha(T - T_0)] \tag{3.13}$$

where T_0 is the reference temperature (K), T is conductor temperature, $\rho_0$is resistivity at the reference temperature (Ω/m) and α is the temperature coefficient (K^{-1}).

Table 3.5 shows the resistivity and temperature coefficient of the four test samples. Compared with pure aluminium, the resistivity of test samples is 26%-36% higher and their temperature coefficients around 25% and 50% lower. In [107], the resistivity of copper alloy is around 2 times higher than pure copper, with the temperature coefficient of copper alloy being 35% that of pure copper. The measured values were applied in the simulation model for each one respectively.

Table 3.5 Resistivity and temperature coefficient for test samples.

Sample	Resistivity (Ω.m)	Temperature Coefficient (1/K)
10 mm rod	3.577×10^{-8}	0.0030
25*3 mm busbar	3.309×10^{-8}	0.0029
30*6 mm busbar	3.611×10^{-8}	0.0020
15 mm rod	3.422×10^{-8}	0.0028

3.3.2 Heat Generation and Heat Transfer Governing Equation

Heat Generation

The heat generation of the conductor was simulated by joule loss, which is calculated by Equation 3.14.

$$Q = \frac{I^2 R_{AC}}{SL} \tag{3.14}$$

where Q is the heat generated by the conductor (W), I is the current through the conductor (A) and R_{AC} is the AC resistance of the conductor (Ω), which considers the effect of temperature and frequency.

When AC current flows through the conductor, the current density is concentrated on the surface of the conductor due to the skin effect [108], which affects the current distribution and increases conductor resistance. In this simulation, the AC resistance of rods was calculated by the Magnetic Field interface. The governing equations are shown in Equation 3.15 - Equation 3.18 [109]. The magnetic field is calculated based on Ampere's Law in Equation 3.15 - Equation 3.16. The relationship between magnetic flux is defined in Equation 3.17 and the relationship between current and electric field is defined in Equation 3.18 [108].

$$\nabla \times \mathbf{H} = \mathbf{J} \tag{3.15}$$

$$\mathbf{E} = -\mathrm{j}\omega\mathbf{A} \tag{3.16}$$

$$\mathbf{B} = \nabla \times \mathbf{A} \tag{3.17}$$

$$\mathbf{J} = \sigma\mathbf{E} \tag{3.18}$$

where **H** is magnetic field (A/m), **J** is current density (A/m^2), **E** is electric field (V/m), ω is angular frequency (radians/second), **A** is magnetic vector potential (T·m), **B** is magnetic flux (T) and σ is the conductivity (S/m).

The AC resistance of cables can be calculated based on skin depth while the AC resistance of busbars can only be calculated based on empirical equations.Therefore, in this project, the AC resistance of busbars was calculated by COMSOL through the empirical equations shown in Equation 3.19-Equation 3.25 [110]:

$$R_{ac} \approx \left[\frac{\rho l}{wt}\right]\left[\frac{K_C}{1 - e^{-x}}\right] \tag{3.19}$$

Where $$K_C = 1 + F_{(f)}\left[\frac{1.2}{e^{\frac{2.1t}{w}}} + \frac{1.2}{e^{\frac{2.1w}{t}}}\right] \quad (3.20)$$

$$F_{(f)} = (1 - e^{-0.026p}) \quad (3.21)$$

$$p = \sqrt{8\pi f / R_{DC} \times 10^7} \quad (3.22)$$

$$x = \frac{\left[\frac{2\delta}{t\left(1+\frac{t}{w}\right)} + \frac{8\left(\frac{\delta}{t}\right)^3}{\frac{w}{t}}\right]}{\left[\left(\frac{w}{t}\right)^{0.33} e^{\frac{-3.5t}{\delta}} + 1\right]} \quad (3.23)$$

$$\delta = \sqrt{\frac{\rho}{\pi \times f \times \mu}} \quad (3.24)$$

$$\mu = \mu_0 \mu_r \quad (3.25)$$

Where R_{ac} is AC resistance (Ω), ρ is material resistivity (Ω/m), l is the length of samples (m), w and t are the width and thickness of the conductor respectively (m), f is frequency (Hz), μ_0 is permeability of free space with the value of $4\pi \times 10^{-7}\ H/m$ and μ_r is relative permeability depending on the material. For aluminium, μ_r is around 1.

Heat Transfer

The heat transfer process of a single-layer insulated cable in free air can be described as an equivalent thermal resistance circuit shown in Figure 3.18.

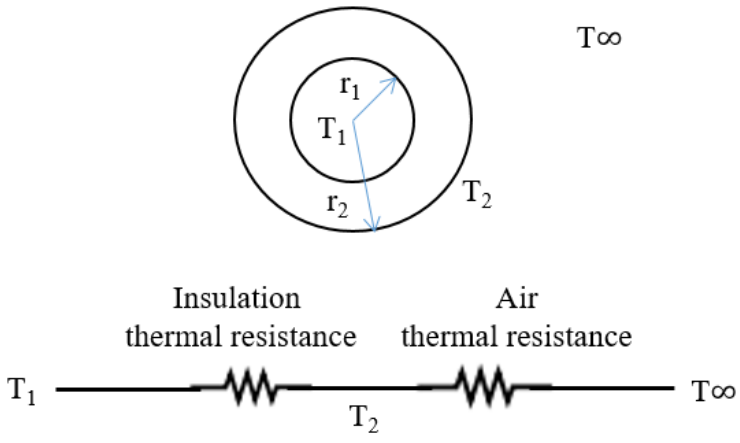

Figure 3.18 Equivalent thermal resistance circuit for an insulated cable.

The heat generated by the conductor is transferred to the cable surface through insulation by conduction. The thermal resistance between the conductor and insulation

surface is expressed using Equation 3.26:

$$T_{insulation} = \frac{\ln (r_2/r_1)}{2\pi kL} \tag{3.26}$$

Where $T_{insulation}$ is thermal resistance the conductor and insulation surface (K/W), k is the thermal conductivity of insulation material (W/(m·K)), $r_1$is the conductor radius (m), r_2 is the cable radius (m) and L is the cable length (m).

The heat transfer in cable can be expressed using Equation 3.27:

$$\rho C_p \frac{\partial T}{\partial t} = \nabla \cdot (k\nabla T) + Q \tag{3.27}$$

where ρ is the density (kg/m^3), C_p is the specific heat (J/kg·K), ∇T is the temperature difference (K), k is the thermal conductivity (W/(m·K)), and Q is the heat source (W).

Then the heat on the cable surface is dissipated by convection and radiation. The convective thermal resistance between cable surface and surrounding medium is expressed using Equation 3.28:

$$T_{air} = \frac{1}{\pi D h L} \tag{3.28}$$

Where T_{air} is thermal resistance the insulation surface and surrounding air (K/W), D is the cable diameter (m), h is the heat transfer coefficient (W/(m^2·K)) and L is the cable length (m).

The heat transfer coefficient in 3.28 includes both convection and radiation and as such the value is often computed by computational fluid dynamics (CFD). In fluid mechanics, the Rayleigh number is a dimensionless number used to describe the airflow regime. In order to make the model accurate in respect of convective heat transfer, the flow regime needs to be specified. The Raleigh number can be calculated using Equation 3.29:

$$R_a = \frac{g\beta(T_S - T_{amb})x^3}{\nu\alpha} \tag{3.29}$$

where g is standard gravity (9.8 m/s^2), β is thermal expansion coefficient (K^{-1}), T_S is conductor surface temperature and T_{amb} is ambient temperature far from the conductor, ν is kinematic viscosity of the fluid (m^2/s), α is thermal diffusivity of the fluid (m^2/s), x is characteristic length (m).

The boundary temperature was set at 20 °C, which is close to experimental conditions. The initial pressure was defined at 1 bar. At the ambient pressure, assuming the surface temperature is 200 °C and the ambient temperature is 20 °C, the air parameter is obtained from [111-113]. The calculated Rayleigh number is shown in Table 3.6. When the Raleigh number is lower than 10^9 over a flat plate, the flow type is considered as laminar flow [114]. Thus, laminar flow is applied for the simulation in this chapter.

Table 3.6 Rayleigh number for the different test samples.

Sample	Rayleigh number
10 mm rod	2125
15 mm rod	7174
25*3 mm busbar horizontal	57
3*25 mm busbar vertical	33211
30*6 mm busbar horizontal	459
6*30 mm busbar vertical	57390

The radiative heat transfer was simulated by Equation 3.30:

$$q_{rad} = \sigma\varepsilon\left(T_s{}^4 - T_{amb}{}^4\right) \tag{3.30}$$

Where q_{rad} is the heat flux through cable surface by radiation (W/m^2), σ is the Boltzmann constant (W/m^{2}K^4) and ε is the surface emissivity.

A sensitivity analysis was performed to ensure that the air domain size and meshing size of the model did not significantly influence simulation results. Figure 3.19 presents the effect of model length on the conductor temperature for the 25*3 mm busbar when the current is 400A at 500 Hz. When the model size is above 2 m, the effect of chamber size on the conductor temperature can be negligible. Therefore, the chamber size length was set at 2 m. In this model, it is assumed the test sample is isolated in free space.

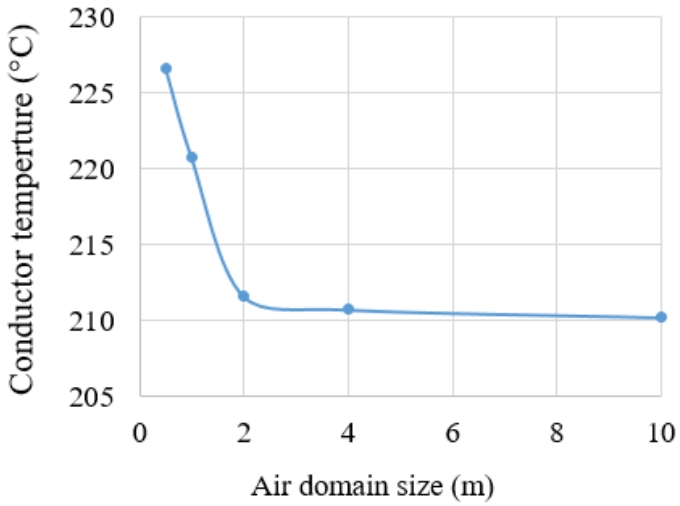

Figure 3.19 The effect of air domain size on the conductor temperature for a 25*3mm busbar when the current is 400 A at 500 Hz.

Simulations were run to calculate the maximum temperature of the 25*3 mm busbar with an applied current of 400 A at 500 Hz using each of the different present mesh sizes shown in Table 3.7. The conductor maximum temperature is a parameter that can show the suitability of the mesh size. The value of the conductor temperature gradually becomes stable when the number of elements is above 7492. The "fine" mesh setting was found to be optimum, with finer meshes not having a significant impact on the results.

Table 3.7 The effect of mesh size on the conductor temperature for a 25*3 mm busbar when current is 400A at 500 Hz and air domain length is 2 m.

Element size	Element number	Conductor maximum temperature (°C)
Coarser	2090	208.96
Coarse	3017	211.1
Normal	4832	211.62
Fine	7492	215.24
Finer	10730	215.74

Processes were conducted to select a suitable air domain size and mesh setting for the 10 mm diameter rod, 15 mm diameter rod, 25*3 mm busbar (vertical position) and 30*6 mm busbar (horizontal and vertical position). A 2 m model size and 'fine mesh' pattern were chosen for all the simulation processes.

3.4 Validation Results

3.4.1 Model Validation under Atmospheric Pressure

This section compares the simulation and test results on the temperature difference between the conductor temperature and ambient temperature for both rods and busbars

Rods

The comparison between the simulation results and experimental results for the 10 mm and 15 mm rods is shown in Figure 3.20 and Figure 3.21, respectively. The results show that the simulation results have a similar tendency as the test results. The difference is between 2 ºC and 4 ºC for the 10 mm rod and is in the range between 1 ºC and 3 ºC for the 15 mm rod.

The conductor temperature increases with the increasing frequency and current in all cases. The 15 mm rod has a lower conductor temperature than the 10 mm rod under the same operating conditions because it has a lower resistivity and a large surface area, leading to lower heat losses and better convection and radiation.

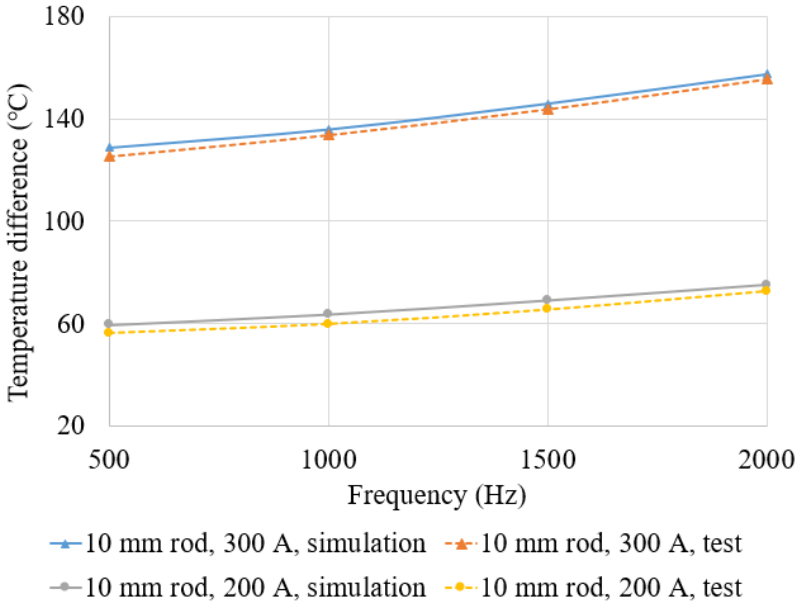

Figure 3.20 Comparison between simulation and test results for the 10 mm rod.

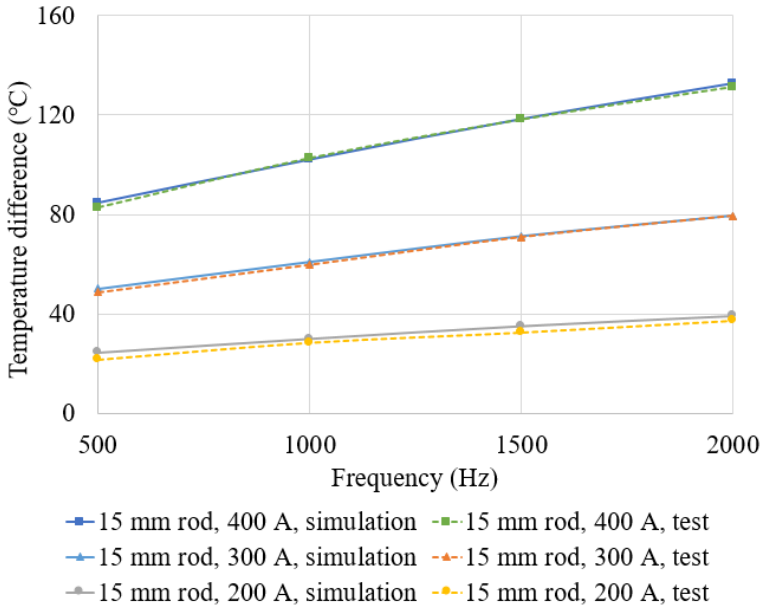

Figure 3.21 Comparison between simulation and test results of 15 mm rod.

Table 3.8 and Table 3.9 show the simulated AC resistance and calculated AC resistance for the 10 mm and 15 mm rods respectively at the simulated frequency and temperature according to the Standard IEC 60287-1-1. The difference is within 1%, meaning that the thermal model can accurately simulate the skin effect of the rod up to 2000 Hz. As the simulation conductor temperatures are consistent with the experiment results, it indicates that the thermal model can accurately simulate both the heat production and dissipation of the rods.

Table 3.8 Simulated and calculated AC resistance of 10 mm rod with 1 m length.

Current (A)	Frequency (Hz)	Simulated AC resistance (μΩ)	Calculated AC resistance (μΩ)	Percentage difference (%)
200	500	552.92	547.19	1.04
	1000	598.84	593.37	0.91
	1500	663.04	657.42	0.85
	2000	735.67	730.28	0.73
300	500	640.31	633.79	1.02
	1000	685.13	678.62	0.95
	1500	749.62	743.15	0.86
	2000	824.95	818.46	0.79

Table 3.9 Simulated and calculated AC resistance of 15 mm rod with 1 m length.

Current (A)	Frequency (Hz)	Simulated AC resistance (μΩ)	Calculated AC resistance (μΩ)	Percentage difference (%)
200	500	252.1	249.92	0.86
	1000	320.46	318.17	0.71
	1500	385.36	383.71	0.43
	2000	440.13	436.41	0.85
300	500	265.19	262.86	0.88
	1000	335.28	332.79	0.74
	1500	404.63	403.73	0.22
	2000	464.56	461.08	0.75
400	500	282.93	280.4	0.89
	1000	354.87	352.244	0.74
	1500	428.83	428.98	0.03
	2000	495.36	492.56	0.57

Horizontal Busbars

Figure 3.22 and Figure 3.23 present a comparison between the simulation and test results for the 25*3 mm busbar and 30*6 mm busbar, respectively. The test and simulation results present similar increasing trends. The temperature difference is increased by the increasing current and frequency in all cases. The difference is in the range of 3 ºC and 9 ºC for the 25*3 mm busbar and in the range 1 ºC and 5 ºC for the 30*6 mm busbar.

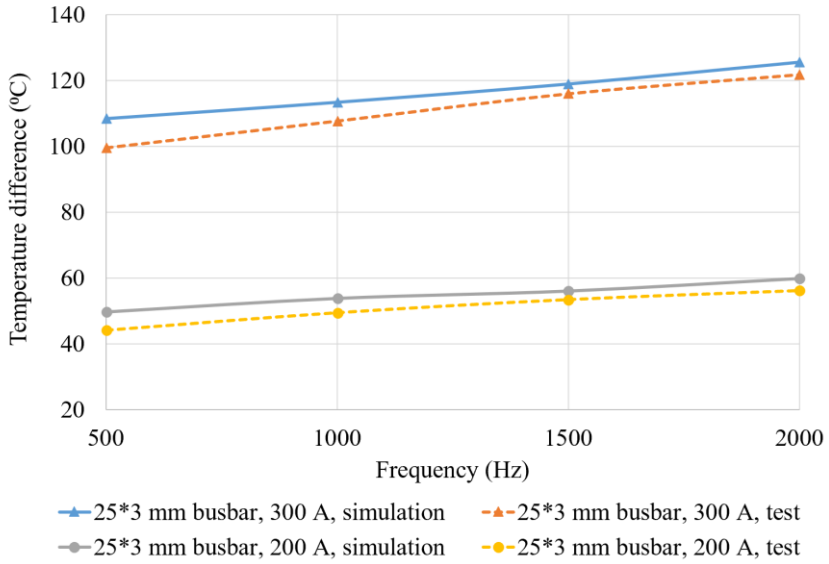

Figure 3.22 Comparison between simulation and test results for the 25*3 mm busbar.

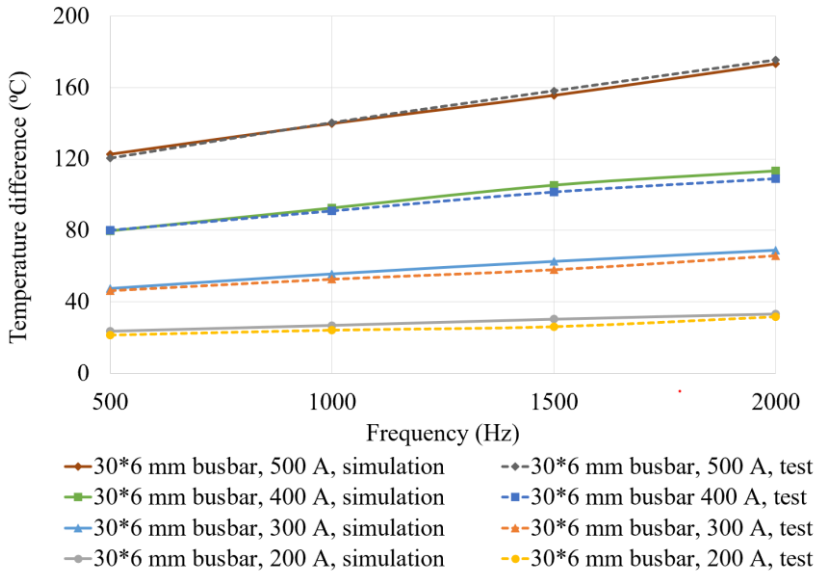

Figure 3.23 Comparison between simulation and test results for the 30*6 mm busbar.

Vertical Busbars

Figure 3.24 and Figure 3.25 show a comparison of the results for the 3*25 mm and 6*30 busbars under various frequencies and current levels. The test results are higher than the simulation results and the differences between test and simulation results increases with increasing current. For the 3*25 mm busbar, the difference is in the range of 2 ºC to 4 ºC at 200 A and 5 ºC to 8 ºC at 300 A. For the 6*30 mm busbar, the maximum difference between the simulation and test results is within 2 ºC at 200 A, 4 ºC at 300 and 400 A, and 9 ºC at 500 A.

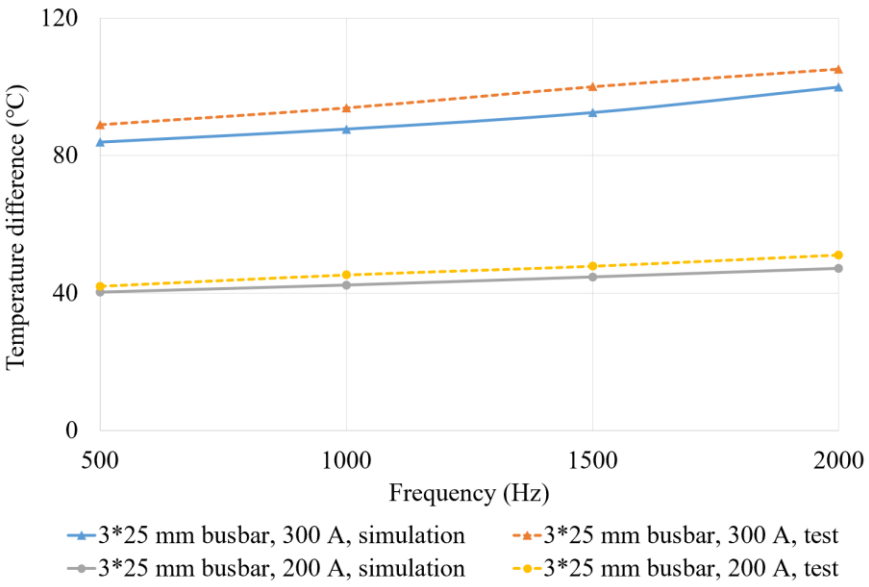

Figure 3.24 Comparison between simulation and test results of 3*25 mm busbar.

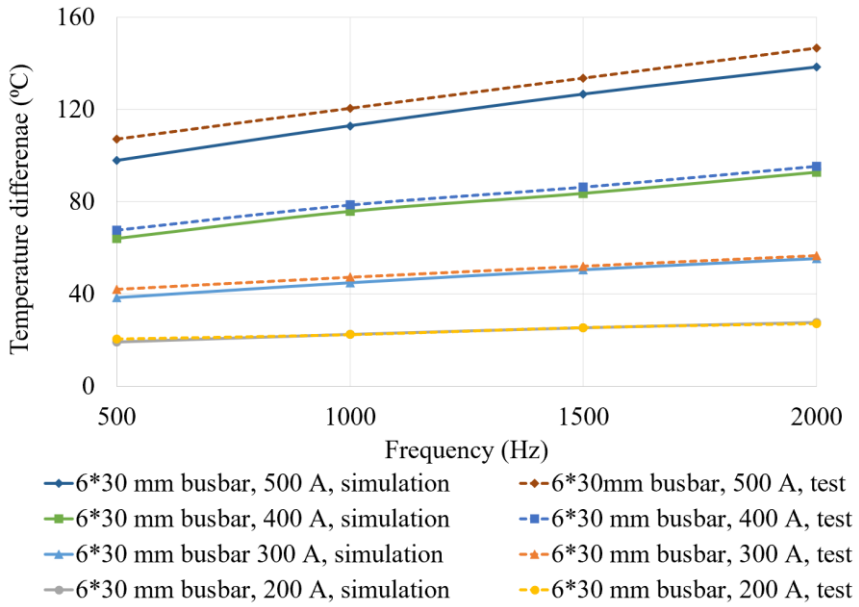

Figure 3.25 Comparison between simulation and test results of 6*30 mm busbar.

Based on the test and simulation results shown above, the maximum difference between the simulation and test results is 4 °C for rods, 9 °C for horizontal busbars and 9 °C for vertical busbars. The differences between the simulations and tests are caused by many factors, including uncertainty about the thermocouples and measurement equipment, thermal conduction from the contact part and thermal dissipation from the transformer.

By comparing the thermal performance of these samples, the samples with larger cross-section areas have a better thermal performance as expected. A rectangular conductor

has a lower conductor temperature than a circular conductor when the conductor has a similar cross-section area. The results also show that the position will affect temperature distribution. The vertical position has a larger convective heat transfer coefficient than the horizontal position, leading to a better thermal performance.

3.4.2 Model Validation under Low Pressures

To check the validity of the model under low pressures, a series of simulations were conducted to calculate the convective heat transfer coefficients of circular wires and compare the results with those reported by Milano [57]. The experiment Milano carried out consisted of three parts: electric wire, surrounding air and the vacuum cylindrical vessel. The wire was a single circular copper conductor with a diameter of 0.155 mm; the cylindrical vessel had a diameter of 0.53 m. The power applied to the conductor was varied to enable the conductor temperature to vary from 40 °C to 130 °C. The pressure was varied from 100 mbar to 1013 mbar. In the experiment, the heat flux lost by conduction through the wire ends was compensated by wrapping the wire with a hot guarded system. Thus, the heat was only dissipated by free convection with the surrounding air and radiation from the wire surface. The thermal model used the same geometry as the experiment. The ambient temperature was set as 20 °C, which was the same as the test conditions.

Figure 3.26 shows the comparison of the convective heat transfer coefficient as a function of ΔT and ambient pressure. The simulation results are in strong correlation with Milano's results. Under constant pressure, the convective heat transfer coefficient increased as the ΔT increased, while decreasing the ambient pressure at a constant temperature decreased the convective heat transfer coefficient. The radiative heat transfer coefficient was less than 1.2% of the total heat transfer coefficient for the range of temperatures and pressures simulated in this part of the study, indicating that the change in the convective heat transfer coefficient is one of the dominant factors affecting the thermal performance of the wire.

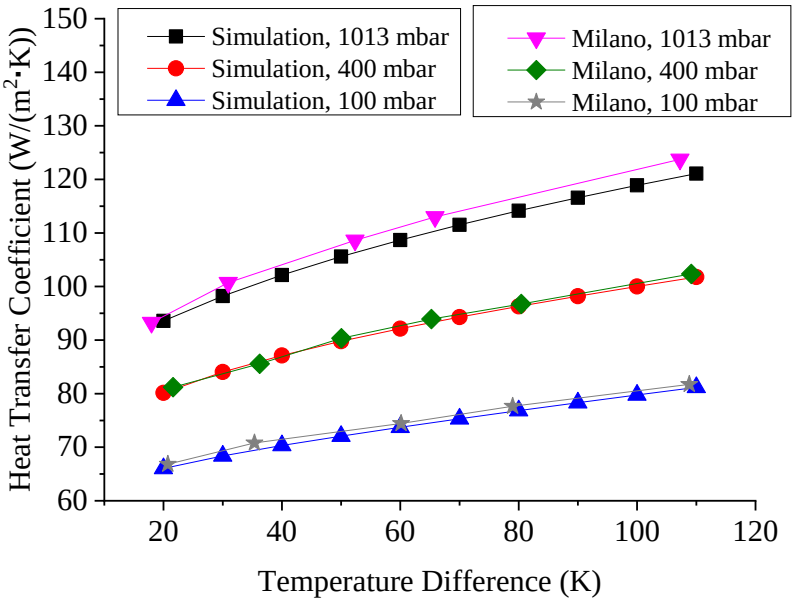

Figure 3.26 Comparison of the convective heat transfer coefficients extracted from the thermal model and the results reported by Milano [57].

3.5 Summary

In conclusion, this chapter described the development of a high-frequency (up to 2000 Hz) thermal test setup and a thermal model based on FEM to investigate the thermal performance of both rods and busbars under various frequencies and pressures. The conclusion of this chapter is summarised below:

- A resonant high-frequency current setup was built, which can be operated under a current up to 500 A and a frequency up to 2000 Hz.
- The thermal model based on FEM can simulate the thermal performance of both cables and busbars under high-frequency conditions with acceptable accuracy. The maximum difference between the simulation and test results was 4 °C for rods, 9 °C for horizontal busbars and 9 °C for vertical busbars under atmospheric pressure.
- The thermal model can be applied under low pressure at around 0.1 bar given its agreement with experimental results in published literature.

Chapter 4 Current Carrying Capacity Design

4.1 Introduction

The previous chapter showed that the verified FEM model could simulate the thermal performance of both cables and busbars under the operating conditions in future aircraft, including kilohertz frequency and lower pressures. Compared with experimental methods, the thermal model is lower cost when investigating the effect of geometry, material and operation condition on the current carrying capacity design.

This chapter investigates the thermal performance and current carrying capacity of both conventional aerospace cables and busbars under aircraft operating conditions. This chapter initially describes the FEM models for the current carrying capacity design, with the effect of parameters such as frequency, pressure and insulation thickness on the current carrying capacity of round cables then analysed. Finally, the parameters affecting thermal performance and current carrying capacity of busbars are investigated and compared to conventional aircraft cables.

4.2 Thermal Model Design

In this chapter, the thermal model for determination of current carrying capacity is based on FEM, which is similar to the verified thermal model described in Section 3.3. The differences in the current carrying capacity model are conductor size, insulation surrounding the conductor and the sample position in the air domain. In this model, the conductor size was set as AWG 4/0 (diameter is 11.68 mm) for round cables – this is the largest conductor size currently used in aircraft and for reasons associated with flexibility is not likely to increase further. For busbars, the cross-sectional area was the same as the cables, with the aspect ratio (w/t) varied to investigate the effect of aspect ratio on thermal performance. Only vertical busbars are simulated in this chapter because they have better thermal performance than horizontal busbars, as discussed in Chapter 3. To investigate the effect of insulation on thermal performance, the conductor was insulated with different PTFE thicknesses. Moreover, the sample was placed in the centre of the air domain. The geometry and dimensions of the insulated cables and insulated busbars are shown in Figure 4.1 and Table 4.1.

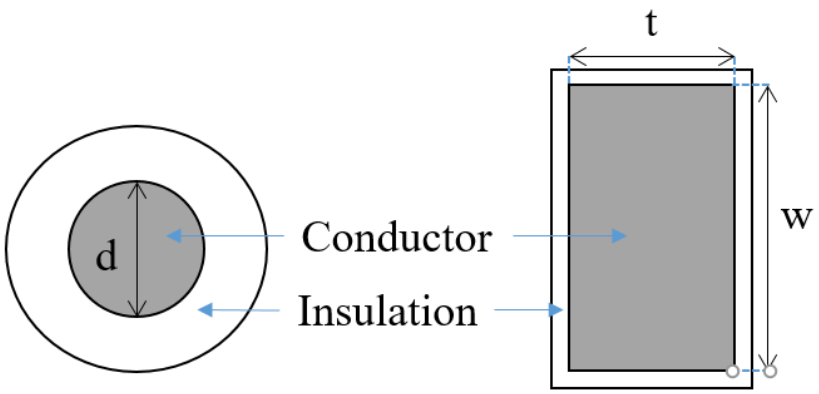

Figure 4.1 The geometry of the insulated cables and the insulated busbars.

Table 4.1 The conductor dimensions of various busbars.

Type	Cable	Busbar w/t=2		Busbar w/t=5		Busbar w/t=8	
Conductor Dimension (mm)	d	w	t	w	t	w	t
	11.684	14.64	7.32	23.15	4.63	29.29	3.66

In this model, both aluminium and copper were used as the conductor materials. The material properties of copper, aluminium and PTFE required for thermal model calculations are displayed in Table 4.2.

Table 4.2 Material properties for thermal simulation [41, 105, 115].

Material	Properties					
	Thermal conductivity (W/m·K)	Density (kg/m3)	Heat capacity (J/kg·K)	Surface emissivity	Temperature coefficient (K^{-1})	Conductivity (S/m)
Copper [41, 105]	400	8960	385	-	0.0039	$5.81*10^7$
Aluminium [41, 105]	238	2700	900	-	0.004	$3.53*10^7$
PTFE [115]	0.25	2200	1300	0.92	-	-

The ambient temperature was set at 40 °C and the minimum pressure was set at 0.238 bar for the current carrying capacity design according to the widely used standard for environmental testing of aerospace equipment, RTCA DO-160 [116]. The maximum operating temperature was set at 200 °C, which is the peak operating temperature of existing aircraft power transmission cables according to Nexans [29].

A sensitivity analysis was conducted to decide the mesh size and boundary size as shown in the validation model section. Simulations were run to calculate the maximum

temperature of the conductor for a circular cable with 5 mm of PTFE insulation with an applied current of 500 A at 1 kHz using each of the different present mesh sizes. The conductor maximum temperature is a parameter that can show the suitability of the mesh size. The value of the conductor temperature gradually becomes stable when the element size is above 3528. The "normal" mesh setting was found to be optimum, with finer meshes not having a significant impact on the results. The influence of the air domain length on the conductor temperature was also investigated when the current is 500 A at 1 kHz, insulation thickness is 5 mm and the mesh element number is 3528. When the air domain length is above 2 m, the effect of chamber size on the conductor temperature is negligible. Therefore, a 2 m chamber size length was chosen.

4.3 Round Cable Results

4.3.1 Effect of Material

The effect of conductor material on current carrying capacity and the value of current capacity/weight are presented in Table 4.3. Under atmospheric pressure and 1 kHz frequency, the current carrying capacity of a copper cable is around 20% higher than that of an aluminium cable when the insulation thickness is 2 mm. This is due to the resistivity of aluminium being 44% higher than copper according to the simulation results. However, the current to weight ratio of a copper cable is only half that of an aluminium conductor, meaning that an aluminium conductor can withstand a higher current level than copper when the cable weight is constant.

Table 4.3 The effect of conductor material on current carrying capacity for AWG 4/0 round cables when the insulation thickness is 2 mm under 1 bar and 1 kHz.

Material	Copper	Aluminium
Current Carrying Capacity (A)	634	530
Simulated resistance (Ω/m)	3.65×10^{-4}	5.24×10^{-4}
Heat generation (W/m)	147	147
Current Carrying Capacity /Weight (A/(kg/m))	551	1108

4.3.2 Effect of Insulation Thickness

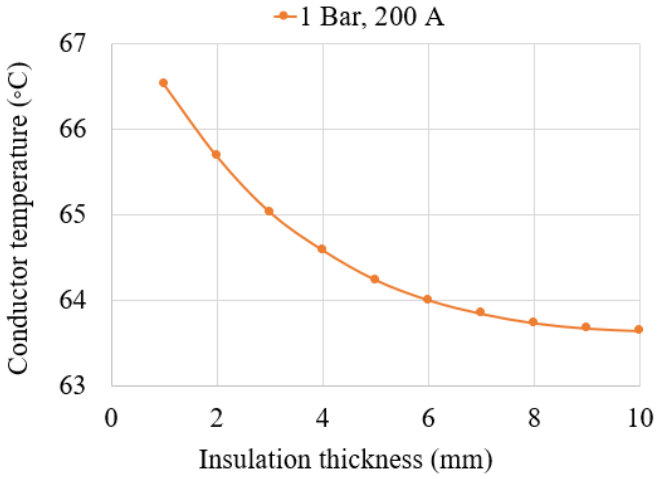

(a)

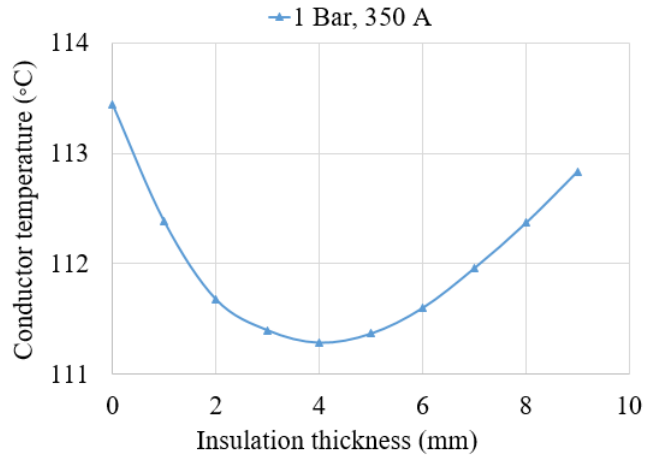

(b)

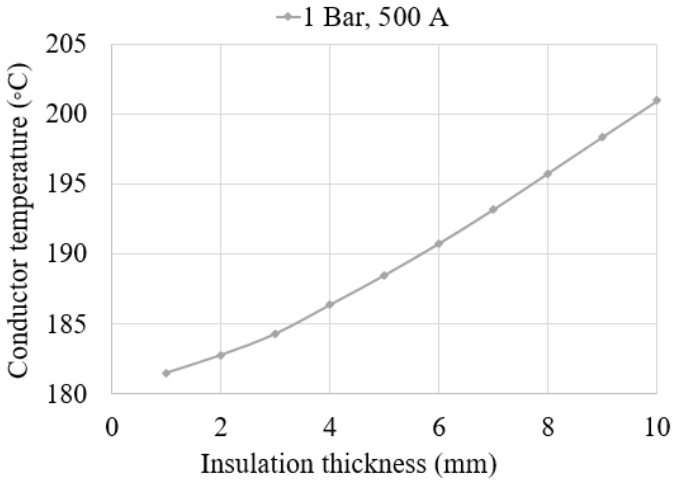

(c)

Figure 4.2 (a)-(c) Conductor temperature as a function of insulation thickness for the currents of 200 A, 350 A and 500 A at 1 kHz and a pressure of 1 bar.

Figure 4.2 shows the conductor temperature as a function of insulation thickness under atmospheric pressure when the current is 200 A, 350 A and 500 A, and the frequency is 1 kHz. When the current increases, the conductor temperature increases as expected. However, the trends of the maximum conductor temperature as a function of insulation thickness for 200 A, 350 A and 500 A are different. At lower levels of current and conductor temperature, increasing insulation thickness decreases the conductor temperature, something that is counterintuitive. In this case, the increased surface area of the cable increases the convective and radiative heat transfer rates that counteract the impact of the increased thermal resistance of the insulation itself. At higher conductor temperature levels, an increase in insulation thickness causes a steady rise in conductor temperature.

Figure 4.3 shows the insulation surface temperature as a function of insulation thickness for currents of 250 A, 350 A and 500 A at 1 kHz and 1 bar. When insulation thickness increases from 1 mm to 10 mm, the outer surface temperature of the insulation decreases in all three cases, caused by the increasing heat transfer capability of air.

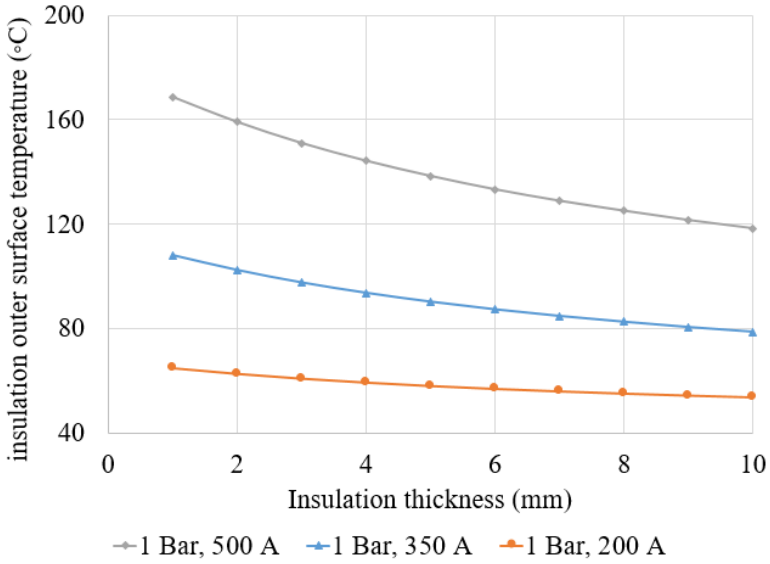

Figure 4.3 Insulation surface temperature as a function of insulation thickness for the currents of 200 A, 350 A and 500 A at 1 kHz and 1 bar.

The effect of insulation thickness on thermal performance can be analysed using the equivalent thermal resistance circuit shown in Figure 3.18. Figure 4.4 shows the insulation thermal resistance and air thermal resistance as a function of insulation thickness for currents of 200 A, 350 A and 500 A at 1 kHz and 1 bar. For all three cases, if the insulation thickness is increased, the thermal resistance of the insulation increases,

which coincides with Equation 3.26. The thermal resistance of air decreases due to the surface area increase, which satisfies Equation 3.28.

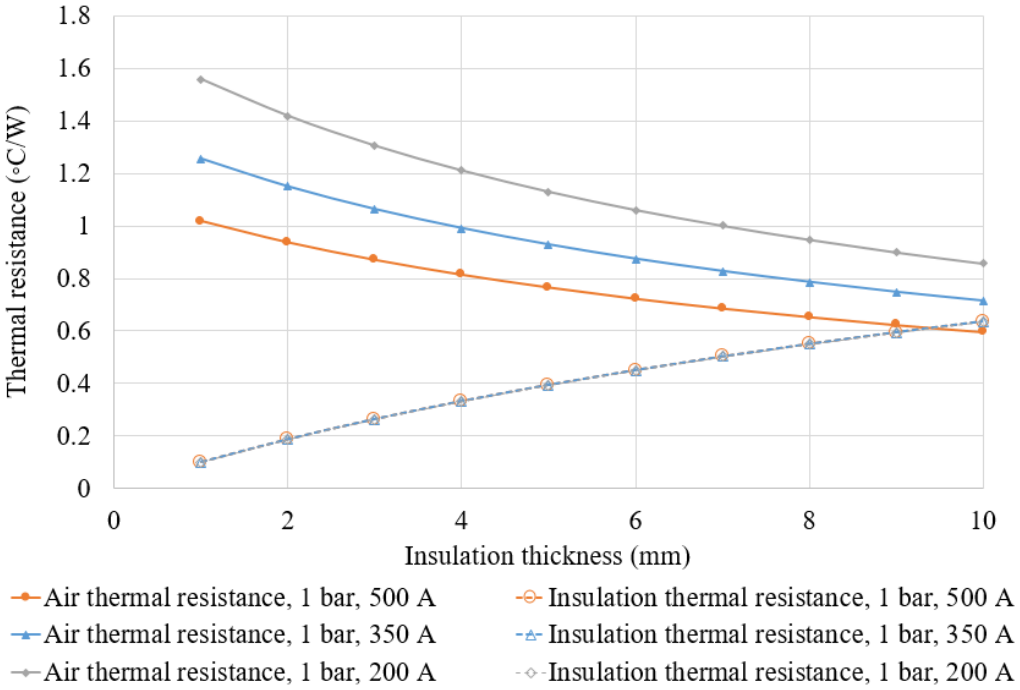

Figure 4.4 The thermal resistance of air and insulation as a function of insulation thickness for currents of 200A, 350A and 500 A at 1 kHz and 1 bar.

Figure 4.5 shows the total thermal resistance of insulation thickness as a function of insulation thickness for currents of 200 A, 350 A and 500 A at 1 kHz and 1 bar, which has the same tendency as Figure 4.2. When insulation thickness increases, the change in conductor temperature depends on the changing rate of both air thermal resistance and insulation thermal resistance. The conductor temperature is proportional to the total thermal resistance, which is a sum of insulation thermal resistance and air thermal resistance.

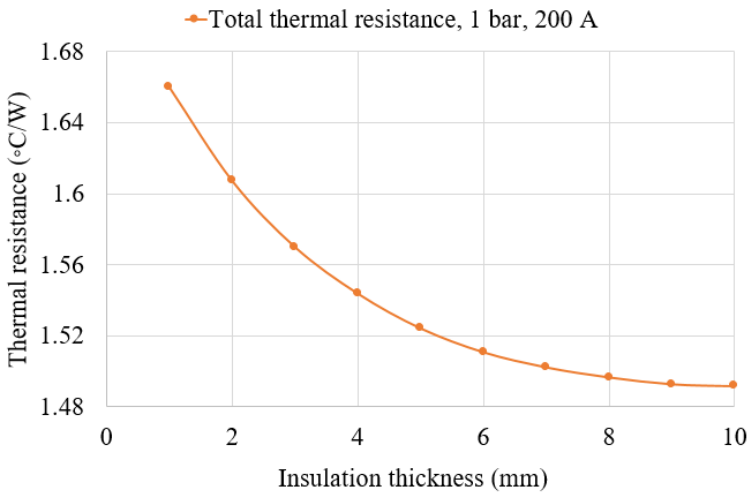

(a)

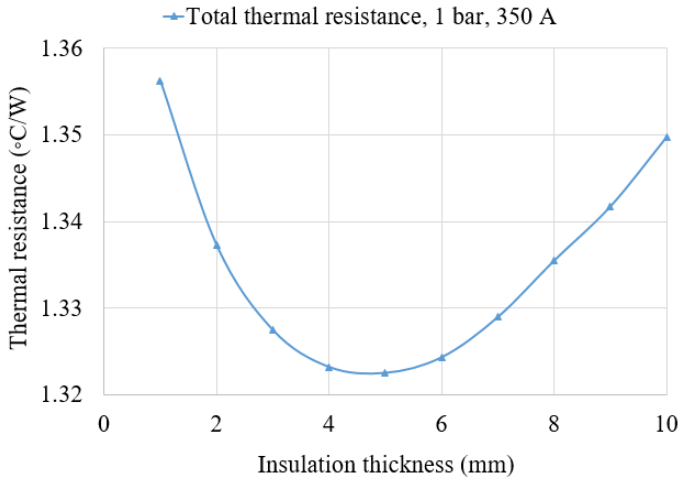

(b)

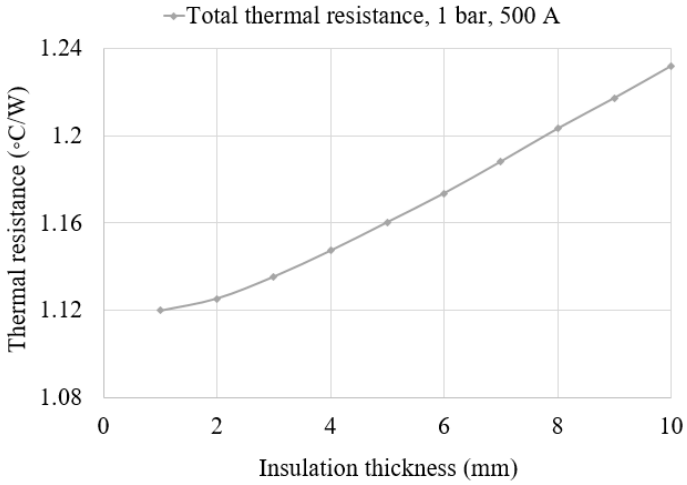

(c)

Figure 4.5 Total thermal resistance as a function of insulation thickness for the currents of 200 A, 350 A and 500 A at 1 kHz and 1 bar.

Figure 4.6 shows the effect of insulation thickness on the current carrying capacity of round cables with a size of AWG 4/0 under 1 kHz and atmospheric pressure. When the insulation thickness increases from 1 mm to 10 mm, the current capacity continuously decreases from 535 A to 498 A. As the maximum operating temperature of insulation material is set at 200 °C, the total thermal resistance continuously decreases with increasing insulation thickness, as explained and shown in Figure 4.3 - Figure 4.5. The insulation thickness in existing aircraft cables is usually around 1 mm and 2 mm. When the frequency increases from 1 mm to 5 mm, the current carrying capacity only decreases by approximately 3%. The insulation thickness does have an impact on the difference between the standard and simulation results, ambient a small one. In SAE AS50881 standard, the current capacity is 560 A for a round conductor. However, the difference between SAE values and simulation results may be mainly caused by frequency rather than insulation thickness. The results recommend there is no need to consider the effect of insulation thickness on the current carrying capacity when the insulation thickness is less than 5 mm.

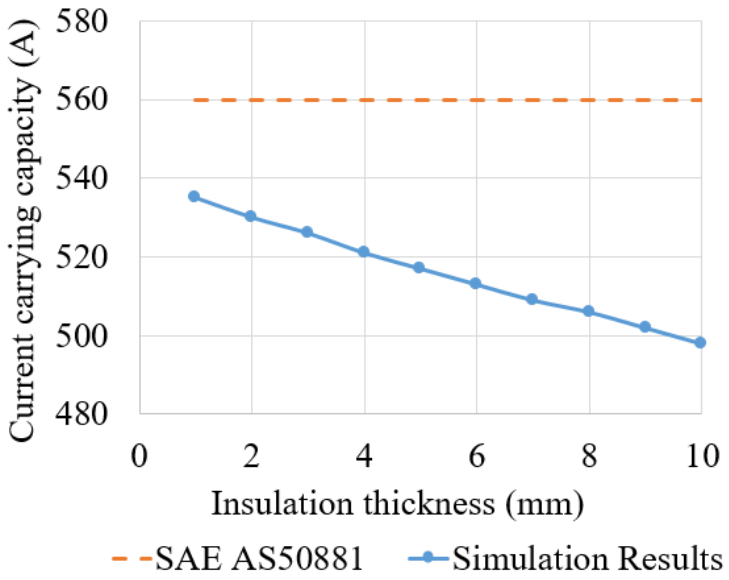

Figure 4.6 The effect of insulation thickness on current capacity for AWG 4/0 round cable under 1 kHz and atmospheric pressure.

4.3.3 Effect of Frequency

Figure 4.7 shows the effect of frequency on conductor temperature at 500 A and 1 kHz. The conductor temperature has a quasi-linear relationship with frequency. It increases around 47 °C from 500 Hz to 2000 Hz. When the frequency increases, the skin depth reduces, which leads to an increase of conductor resistance and conductor temperature.

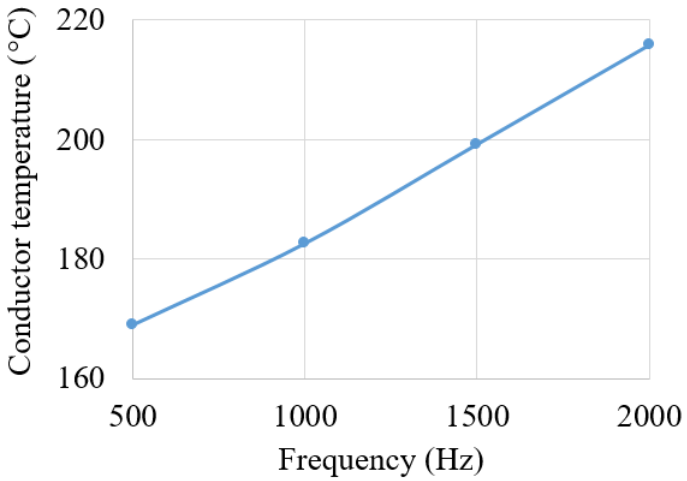

Figure 4.7 Conductor temperature as a function of frequency for AWG 4/0 round cable with an insulation thickness of 2 mm under a current of 500A and a pressure of 1 bar.

Figure 4.8 shows current carrying capacity as a function of frequency for a maximum conductor temperature of 200 °C. When the frequency increases from 500 Hz to 2000 Hz, the current carrying capacity decreases by approximately 5% each 500 Hz and 15% in total across that range. The SAE standard states that the standard is suitable for operating frequencies up to 800 Hz. However, according to the simulation results, a frequency under 800 Hz also has a pronounced effect on current capacity. The results suggest that SAE standard should have a correction factor considering effect of frequency on current carrying capacity when the skin depth is smaller than the conductor radius.

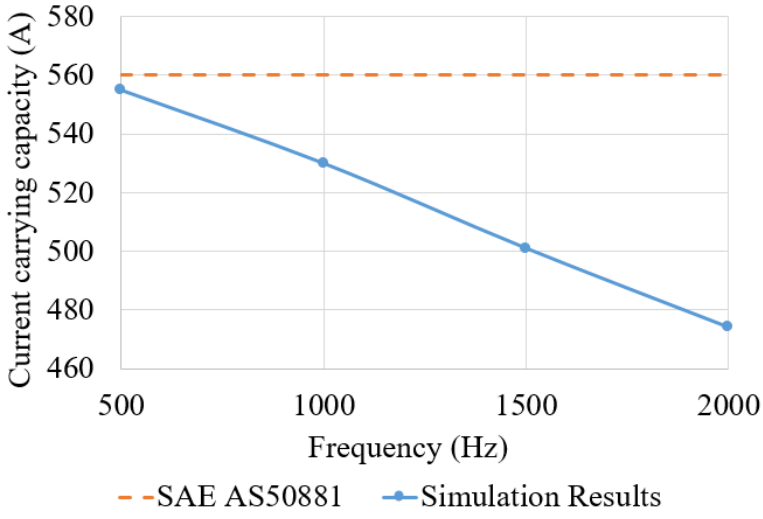

Figure 4.8 Current carrying capacity as a function of frequency for AWG 4/0 round cable with an insulation thickness of 2 mm under 1 bar.

4.3.4 Effect of Pressure

Figure 4.9 shows the influence of pressure on maximum conductor temperature for cylindrical cables when the current is 500 A and the frequency is 1 kHz. When the pressure decreases from 1 bar to 0.238 bar, the conductor temperature increases from 183 °C to 212 °C due to poorer thermal convection at lower pressures. The process of conduction through the insulation and radiation are unchanged, although radiation is obviously influenced by the surface temperature of the insulation so actually rises as a proportion of the heat transfer in air.

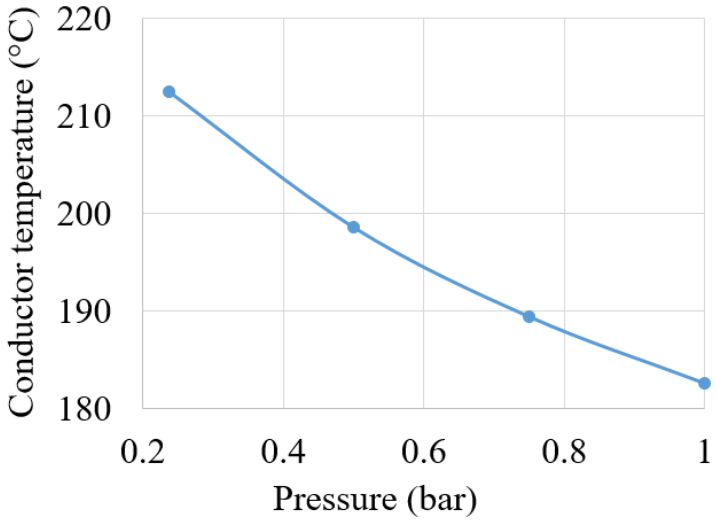

Figure 4.9 Conductor temperature as a function of pressure for AWG 4/0 round cable with an insulation thickness of 2 mm under a current of 500A and a frequency of 1 kHz.

Figure 4.10 shows the effect of pressure on current carrying capacity under both constant and various ambient temperatures. If the ambient temperature is constant at 40 °C, the current carrying capacity decreases from 530 A to 479 A when the pressure decreases from 1 bar to 0.238 bar (a decrease of approximately 10%). The SAE standard has a conservative margin for the derating factor that is affected by pressure, which is around 5% at 0.238 bar compared with the simulation results. The conservative margin increases with decreasing pressure, which is consistent with the results in [46]. The International Standard Atmosphere (ISA) sets an assumption of a decrease in air temperature of 1.98 °C when the altitude decreases 1000 m [117]. If the thermal model also considers the change of ambient temperature as a function of altitude (assuming an unheated environment such as wings), the current carrying capacity increases from 530 A to 545 A when pressure decreases from 1 bar to 0.238 bar. The results suggest that

the change of ambient temperature versus altitudes should also be accounted for the correction factor considering the effect of pressure on current carrying capacity.

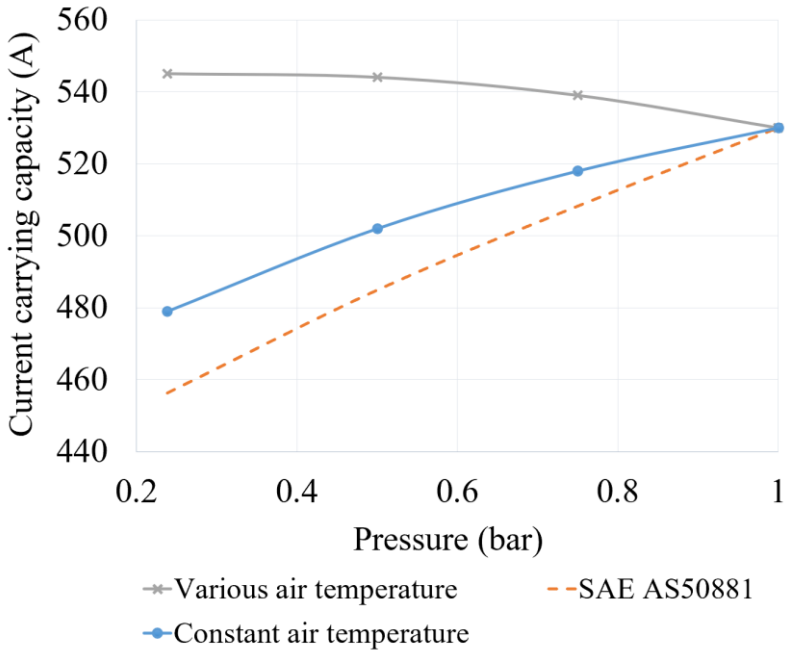

Figure 4.10 Current carrying capacity as a function of pressure for AWG 4/0 round cable with an insulation thickness of 2 mm under a frequency of 1 kHz.

Based on the discussion above, the effect of the insulation thickness, frequency and pressure on current capacity is summarised in Table 4.4. The simulation and standard only consider a single-phase current capacity scenario. Under three-phase conditions, the current capacity will be reduced due to two reasons: (1) the proximity effect caused by surrounding cables increasing the resistance of the cables and (2) the existing surrounding cables reducing the convective and radiative heat transfer capabilities. Therefore, for a three-phase cable design (or for any other design that uses some form of cable bundles), a de-rating factor needs to be considered. However, the effect of the parameters listed is not expected to change.

Table 4.4 Summary of effect of parameters on current capacity

Parameters	**Change tendency**	**Change tendency of Current Capacity**
Insulation thickness	↑	↑ or ↓
Frequency	↑	↓
Pressure	↑	↑

4.4 Busbar and Round Cable Comparison

4.4.1 Thermal Performances Comparison

When the input current is 500 A at 1 kHz, the relationships between maximum temperature and insulation thickness for various conductor shapes under 1 bar and 0.238 bar are shown in Figure 4.11 and Figure 4.12 respectively. When the insulation thickness increases from 1mm to 10 mm, the conductor temperature for all cables and busbars continuously increases under 1 bar. The conductor temperature for busbars with a w/t ratio of 2 is lower than that of a circular cable when the insulation thickness is less than 6 mm. After that, the conductor temperature between them is almost equal. For a busbar with a w/t ratio of 5, its maximum conductor temperature varies from 80% to 85% of a circular cable. For a busbar with a w/t ratio of 8, its maximum conductor temperature varies from 72% to 76% of that of circular cables. When the pressure is 0.238 bar, all busbars have a lower conductor temperature than circular cables as they have a higher surface area resulting in better convective and radiative thermal dissipations.

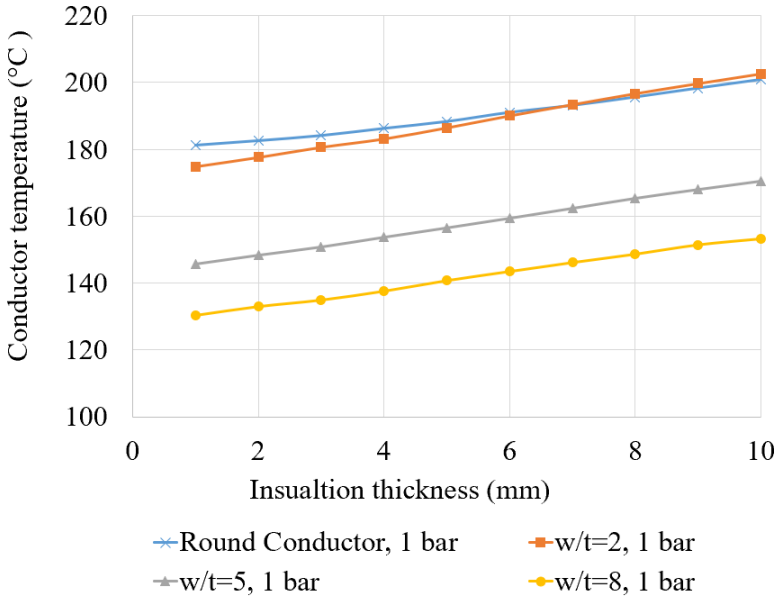

Figure 4.11 Conductor temperature as a function of insulation thickness when pressure is 1 bar.

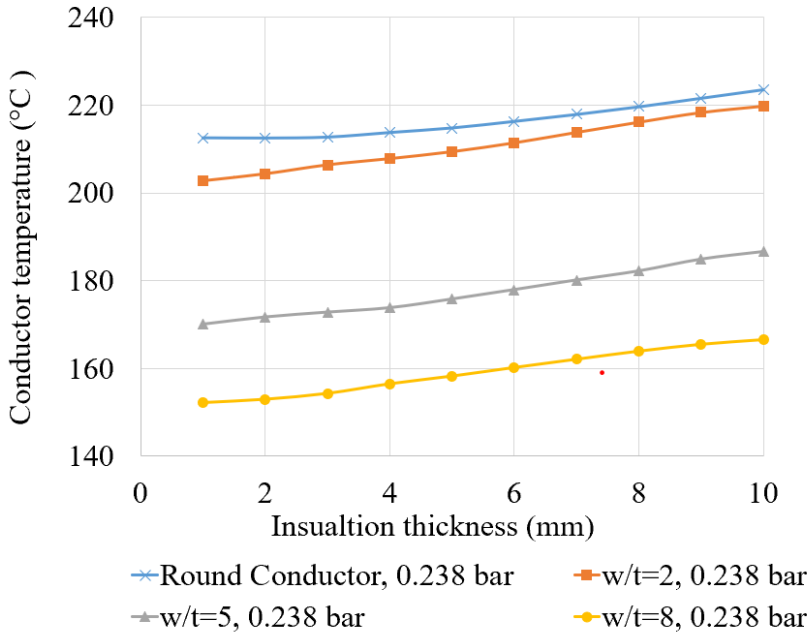

Figure 4.12 Conductor temperature as a function of insulation thickness when pressure is 0.238 bar.

4.4.2 Comparison of Current Carrying Capacity

The maximum currents that can be carried by a 4/0 AWG wire and similar cross-section area busbars under 1 bar and 0.238 bar are shown in Figure 4.13 and Figure 4.14. For a specific pressure, when the frequency increases from 500 Hz to 2 kHz, the maximum carried current decreases due to increasing resistance caused by the skin effect. For a specific frequency, when the pressure decreases from 1 bar to 0.238 bar, the maximum carried current decreases due to the decrease of the convective heat transfer coefficient of air.

As the ratio of w/t increases, the busbar can carry more current. It has a better thermal dissipation due to increasing surface area and a smaller conductor resistance as a result of the reduced impact of skin effect. When the aspect ratio is 2, the current capacity varies 2% to 4% higher than round cables. When the aspect ratio is 5, the current capacity varies 15% to 18% higher than round cables. When the aspect ratio is 8, the current capacity varies 23% to 29% higher than round cables. For all conductors, the maximum carried current at 0.238 bar and 500 Hz is larger than that at 1 bar and 2 kHz. The reason is that the skin effect caused by frequency between 500 Hz to 2000 Hz has a more pronounced effect than the convection heat transfer capability affected by pressure between 1 bar to 0.238 bar.

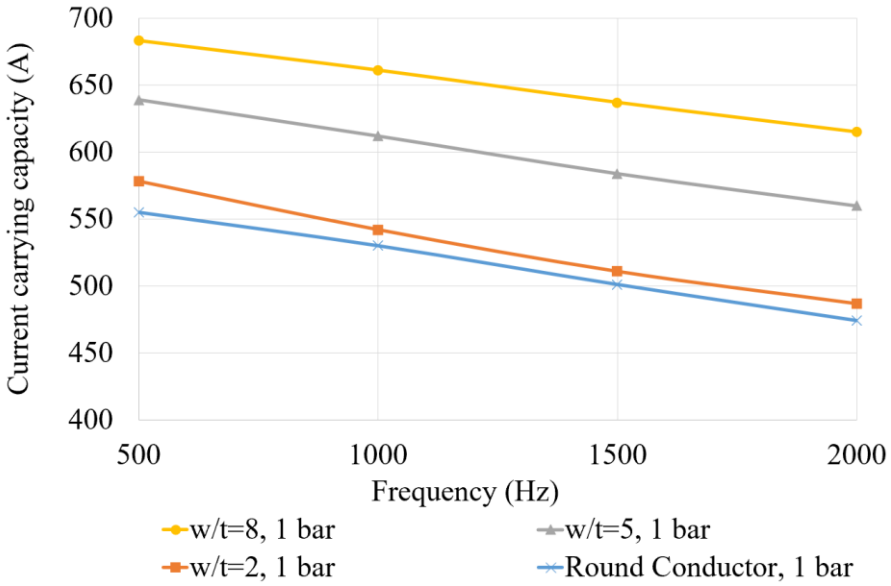

Figure 4.13 The maximum current carried by 4/0 AWG wire and rectangular conductors with various ratios as a function of frequency under 1 bar of pressure.

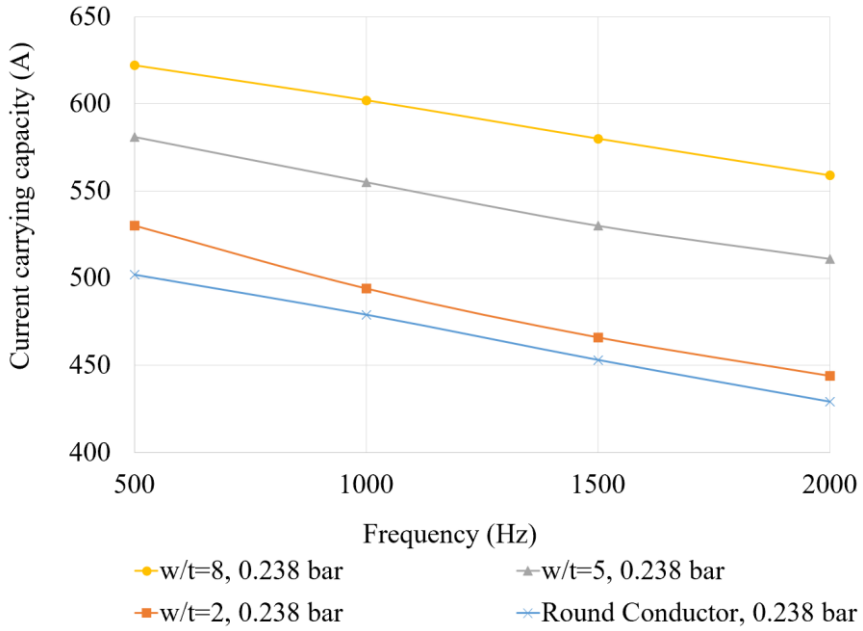

Figure 4.14 The maximum current carried by 4/0 AWG wire and rectangular conductors with various ratios as a function of frequency under 0.238 bar of pressure..

Table 4.5 shows the ratio of the maximum current at 2 kHz to the maximum current at 500 Hz as a function of pressure. As the w/t ratio increases, busbars are less affected by the skin effect. Thus, the current carrying capacity ratio of 2 kHz to 500 Hz increases.

Table 4.5 The ratio of the maximum current at 2 kHz and the maximum current at 500 Hz.

	Ratio of current capacity at 2 kHz to that at 500 Hz	
Conductor shape	Pressure 0.238 bar	Pressure 1 bar
Cable	0.85	0.85
Busbar, w/t=2	0.84	0.84
Busbar, w/t=5	0.88	0.88
Busbar, w/t=8	0.9	0.9

4.5 Summary

In this chapter, a FEM thermal model validated by experiments was used to investigate the thermal performances and current carrying capacity of circular cables and rectangular busbars under various conditions. Based on the results, the following conclusions are summarised:

- For an AWG 4/0 cable, copper conductors have an approximately 20% higher current carrying capacity than aluminium conductors under 1000 Hz. This is due to an aluminium conductor having a 44% higher resistivity than a copper conductor.
- Changing insulation thickness has less of an effect on the current carrying capacity. When the insulation thickness increases from 1 mm to 5 mm, the current carrying capacity only changes by approximately 3%.
- When the frequency increases from 500 Hz to 2000 Hz, the current carrying capacity decreases by around 15% for an AWG 4/0 cable. Compared with insulation thickness, frequency will be a more important consideration for the current carrying capacity design in future aircraft in an AC system (in a DC system, insulation thickness would remain the driver).
- The committee that develops the SAE standard would be recommended to consider the effect of frequency on current carrying capacity. They should also consider the impact of the change of ambient temperature versus altitude for the correction factor related to the change of pressure. There is no need to consider the effect of insulation thickness on current carrying capacity when the thickness is less than 5 mm.

- Busbars have a larger current carrying capacity than conventional aircraft cables for the same cross-sectional area under low and high pressures. When the aspect ratio is 5, the current carrying capacity of busbars is 15% higher at 500 Hz and 19% higher at 2000 Hz than cables. The current carrying capacity increases with the increasing aspect ratio. When the aspect ratio is 8, the current carrying capacity of busbars is 24% higher at 500 Hz and 30% higher at 2000 Hz than cables.

Chapter 5 Safe Operating Voltage Design

5.1 Introduction

So far the current carrying capacity design of both cables and busbars has been discussed, with the effect of geometry, material properties and operating conditions on current carrying capacity having been analysed. As discussed in Chapter 1, both voltage and current levels will increase to achieve a higher power level in future aircraft. The increasing voltage level increases the risk of partial discharge, which contributes to degrading the insulation system and potentially leading to permanent failures. Therefore, it is necessary to define the safe operating voltages of interconnection systems for future aircraft to improve their safety and avoid catastrophe.

In conventional aircraft, partial discharge does not usually take place when the voltage level is lower than Paschen's minimum. Additionally, as the dielectric strength of solid insulation is many times higher than that of air, if the voltage is increased, partial discharge would only take place in air gaps surrounding the insulation of unscreened cables, assuming the insulation material is void free. At present, the PDIV of existing aircraft cables under aerospace operating conditions has been widely calculated based on Halleck's method [75, 79]. This method is derived by applying air breakdown voltages from Paschen's curve to the theoretical voltage distribution between air and insulation material. The SAE AS50881 presents the relationship between PDIV and the ratio of insulation thickness to relative permittivity, which may be derived from Halleck's method due to the voltage distribution for unscreened cables being dependent on the thickness and relative permittivity of insulation materials under an AC system. However, it is unclear if this method is suitable for unscreened busbars and for cables with an increasing insulation thickness where the electric field becomes more non-uniform.

In this chapter, the PDIV of both unscreened cables and busbars will be calculated by implementing the streamer criterion method. It initially introduces the PDIV model and includes a description of the streamer criterion method, electric field simulation and the determination of effective ionisation. The simulation results are then compared with the experimental data to validate the predictive model. Finally, the effect of parameters such as geometry, insulation thickness and pressure on the PDIV for both unscreened cables and unscreened busbars will be analysed.

5.2 The Partial Discharge Inception Voltage Model

5.2.1 The Streamer Criterion Method

The streamer criterion method is based on the electron avalanche mechanism of gas. Free electrons accelerate along the electric field line and subsequently collide with other atoms or gas molecules. Thus, additional electrons are released and these electrons accelerate and collide, leading to a chain reaction generating more electrons. It is assumed that the streamer occurs along an electric field line when the electron density is higher than a critical value that leads to the electron avalanche. The criterion of self-sustained electron avalanche can be expressed using Equation 5.1 [78]:

$$\int_0^d \bar{\alpha}\, dx \geq K \tag{5.1}$$

where d is the distance travelled along an electric field line between the anode and cathode, $\bar{\alpha}$ is effective ionisation coefficient and K is critical constant.

The electrical discharge of gas is based on ionisation. This method introduces the effective ionisation coefficient $\bar{\alpha}$ firstly, which is the net rate production of free electrons, which can also be expressed as the ionisation rate minus the recombination and attachment rates. The value of the effective ionisation coefficient depends on *E/p* (electric field strength/pressure) and gas properties. The density of electrons increases along the electric field line when $\bar{\alpha} > 0$. K is an empirical constant to define the criterion of electron avalanche of gas. The advantage of this method is that it can be applied to the complex geometry with a non-uniform electric field such as busbars.

The PDIV simulation process is described as in the flowchart shown in Figure 5.1. The electric field distribution was simulated by the electrostatics model in COMSOL Multiphysics 5.4. The relationship beteen the effective ionisation coefficient for air under various electric field strengths and pressures was collected from previous research experiments [118, 119]. The K value was set as 6 and tested by insulated twisted wires from [78].

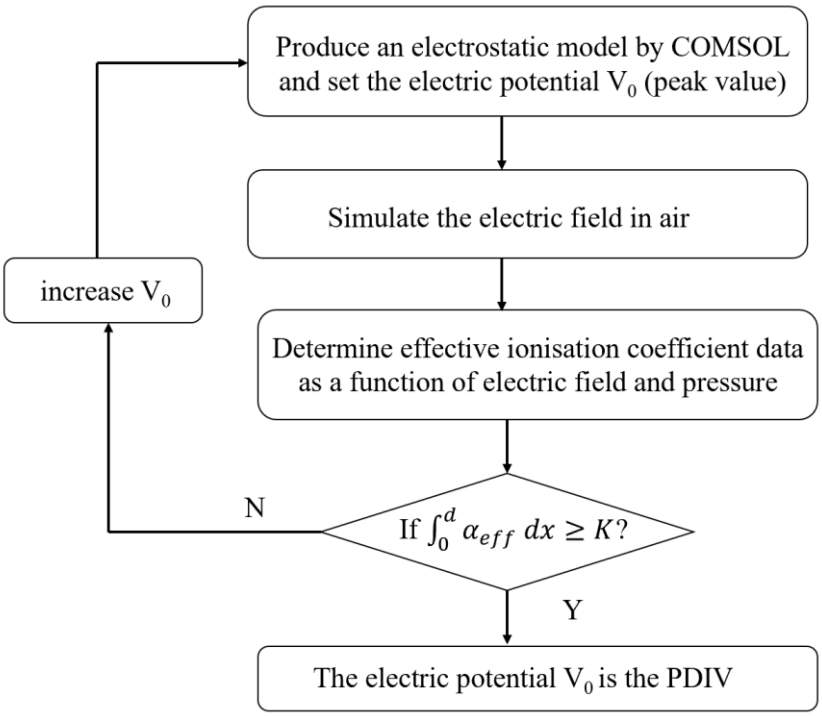

Figure 5.1 PDIV simulation process based on the streamer criterion method.

5.2.2 Electric Field Simulation

For the electric field simulation, the first step is defining the geometry. Both phase-ground and phase-phase geometries are considered because both are applied in aircraft interconnection systems. Figure 5.2 and Figure 5.3 show phase-phase and phase-ground geometries for both cables and busbars. It is noted that the distance in the simulation increases from 0 mm to find the minimum PDIV.

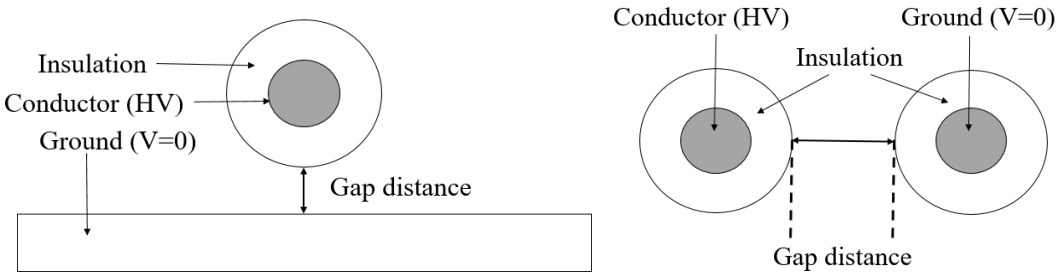

(a) (b)

Figure 5.2 (a) phase-ground geometry and (b) phase-phase geometry for cables

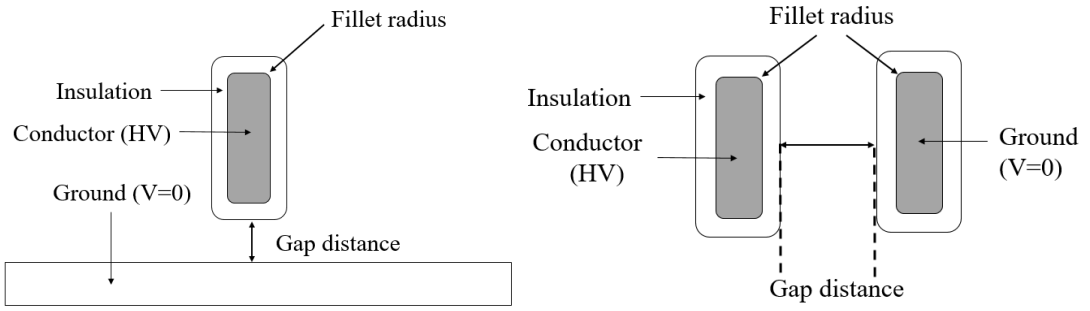

(a) (b)

Figure 5.3 (a) phase-ground geometry (b) phase-phase geometry for busbars

Four different conductor diameters (2.05 mm, 5.19 mm, 8.25 mm and 11.68 mm) were chosen for cables, these correspond to the conductor size used in existing aircraft cables varying between AWG 12 (2.05 mm diameter) and AWG 4/0 (11.68 mm diameter). Identical conductor cross-section areas were chosen for the busbars. The aspect ratio of the busbars varies from 2 to 10. In this study, the aspect ratio of busbars was chosen as 5. The insulation thickness range was from 1 mm to 10 mm to investigate the most suitable insulation thickness for future aircrafts.

In electrostatics mode, the effect of conductivity is negligible, with permittivity the only material property affecting both the electric field strength and distribution. The permittivity of the conductor and the air was set as 1 (the conductor value being irrelevant as this was set as a voltage boundary condition). The typical values of relative permittivity were set for the insulation material at 2.1 for PTFE and 4.5 for polyamide-imide (PAI), respectively.

For cable-ground and busbar-ground configurations, the potentials of the cable and busbar conductors were set as the applied voltage $V=V_0$. The potential of the ground electrode was set as V=0.

The governing equation in electrostatic model is expressed as Equation 5.2:

$$\nabla^2 V = \frac{\rho_V}{\varepsilon_0 \varepsilon_r} \tag{5.2}$$

where V is applied voltage (V), ρ_V is charge density (C/m^3), ε_0 is the permittivity of free space ($8.85*10^{-12}$ F/m), and ε_r is the relative permittivity.

Geometric mesh size is an important factor to ensure the accuracy of simulation results. A finer mesh should be applied to make sure that the simulation results are mesh independent in some important areas. In this study, the contact area between the cable/busbar and ground is the area of interest and in this location the relationship between the simulated electric field, the edge radius and the mesh size is strong. Figure 5.4 shows the four electric field lines of cable-ground geometry. A mesh refinement process was conducted to simulate the effect of increasing element number on the maximum electric field along the electric field lines under a constant applied voltage.

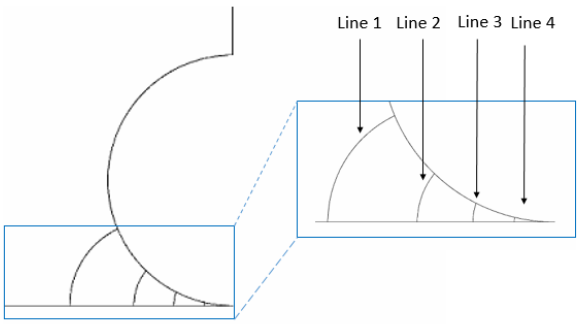

Figure 5.4 Electric field line distribution for cable-ground geometry.

Meshing is one of the most important steps to obtain accurate simulation results using FEM. It divides the geometry into a number of elements and nodes to solve the governing differential equations. The increasing element number increases the accuracy of simulation results but takes more computation sources. Thus, a suitable mesh size should be chosen by considering both accuracy and computation sources. Figure 5.5 presents the mesh refinement results. An increasing element number has a negligible effect on the maximum electric field of line 1. The electric fields of the other three lines vary with the increasing element number. When the element number is around 4580, all lines reach a stable electric field, with an increasing element number having no significant effect on the values. Therefore, this mesh size is selected for this geometry. Similar mesh refinement processes were conducted for all other geometries.

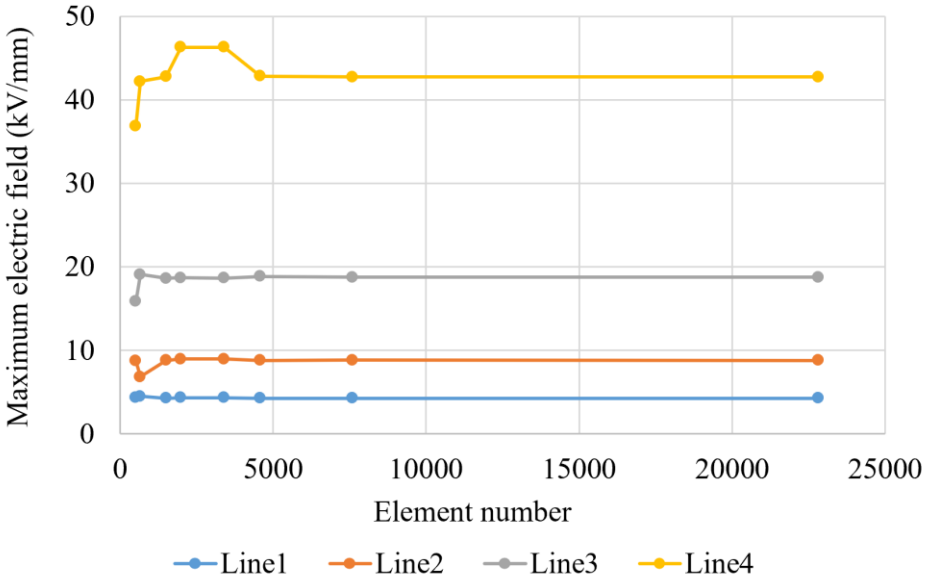

Figure 5.5 Maximum electric field as a function of element number.

Another important parameter investigated was the spacing between adjacent electric field lines. Figure 5.6 shows the effect of the distance between adjacent electric field lines for the conductor-ground geometry. The results indicate that the PDIV is stable when the distance is below 0.6 mm. Similar processes were conducted for the other geometries. It was found that a smaller distance was required when the conductor size decreased. Thus, the distance between the adjacent electric field lines applied in this model was 0.05 mm.

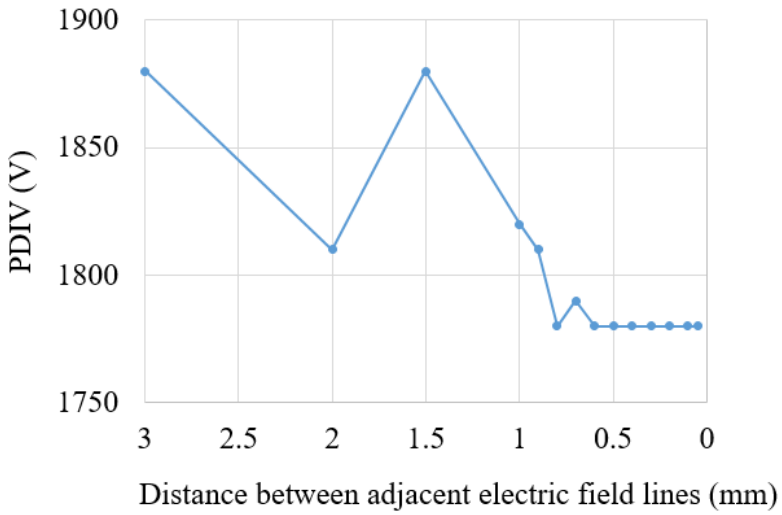

Figure 5.6 The effect of distance between adjacent electric field lines for cable-ground geometry with a conductor diameter of 11.68 mm.

5.2.3 Effective Ionisation Coefficient

In this study, the effective ionisation coefficient data of air as a function of pressure and electric field strength used the measurements results directly from Friedrich and Rao directly [118, 119]. When the range of *E/p* is between 2.588 and 5 kV/(mm.bar), the relationship between $\bar{\alpha}/p$ and E/p can be expressed as Equation 5.3 [118]:

$$\frac{\bar{\alpha}}{p} = C[\frac{E}{p} - (\frac{E}{p})_M]^2 + A \tag{5.3}$$

where C = 1.6053 mm.bar/kV^2

$(E/p)_M$ = 2.165 kV/mm.bar

A = - 0.2873 1/mm.bar

When the range of *E/p* is between 5 and 40 kV/mm.bar, the relationship between $\bar{\alpha}/p$ and *E/p* can be expressed as Equation 5.4 [119]:

$$\frac{\bar{\alpha}}{p} = C_1 * \frac{E}{p} + A_1 \tag{5.4}$$

where C1 = 17.188 1/kV

A1 = - 74.756 1/mm.bar

When the range of *E/p* is between 40 and 70 kV/mm.bar, the relationship between $\bar{\alpha}/p$ and *E/p* can be expressed as Equation 5.5 [119]:

$$\frac{\bar{\alpha}}{p} = C_2 * \frac{E}{p} + A_2 \tag{5.5}$$

where C2 = 9.1955 1/kV

A1 = 225.34 1/mm.bar

5.2.4 Streamer Criterion Model Validation

In [120], the PDIV of a twisted wire with a conductor diameter of 0.368 mm and an insulation thickness of 16 µm was tested and simulated under atmospheric pressure and room temperature (25 °C). The permittivity of the insulation material was 4.53 (given the study was focused on an electrical machine application). In order to validate the model applied in this study, a phase-phase geometry with the same conductor diameter and insulation thickness was simulated. Table 5.1 compares the PDIV results simulated by the model applied in this study with results from [78] , with the calculation based on

Halleck's method presented in section 2.4.2 and the standard AS50881. The PDIV simulated by this model has comparable results with that in existing research, which validates the accuracy of this model.

Table 5.1 PDIV results compared between different methods under atmospheric pressure.

Sample	PDIV (Peak)	Voltage difference compared with cable –ground simulation results (V)	Voltage difference percentage (%)
Simulation result (benchmark)	590	-	-
Test results in [78]	567	-23	- 3.9%
Simulation results [78]	580	-10	-1.7%
AS50881	580	-10	-1.5%
Halleck's method	591	-1	0.2%

5.3 Results

5.3.1 Comparison between Phase-phase and Phase-ground Geometry

Figure 5.7 compares the PDIV between a phase-ground geometry and a phase-phase geometries of cables with a conductor diameter of 11.68 mm and an insulation thickness of 1 mm. The pressure is 0.238 bar, which is the pressure at cruising altitudes for most commercial aircraft. As the gap distance increases, the PDIV initially decreases to a minimum value and then increases for both phase-phase and phase-ground geometries, which can be explained by Paschen's curve (although it is noted that in all cases an air gap exists but this is not in a straight line from the underside of the cable to the earthed conductor). The PDIV decreases with an increasing gap distance as it increases the acceleration distance of free electrons and the likelihood of an ionisation collision. Afterwards, increasing the gap distance reduces the electric field strength in the gap as the percentage of voltage in the gap does not increase at the same rate the size of the gap increases. This then results in a slower acceleration of electrons and a lower probability of an ionisation collision.

The minimum PDIV for phase-phase geometry is approximately 50% higher than that for phase-ground geometry, this correlates with the phase-phase geometry having twice

the insulation thickness. However, the PDIV calculated for phase-phase geometry is phase-phase voltage. If the phase-phase voltage is converted to an equivalent phase-ground voltage, it is around 14% lower compared to the PDIV of phase-ground geometry. Therefore, the safe operating voltage is determined by the phase-phase geometry of cables under the same design and operating conditions, which is consistent with the PDIV calculation results in [22].

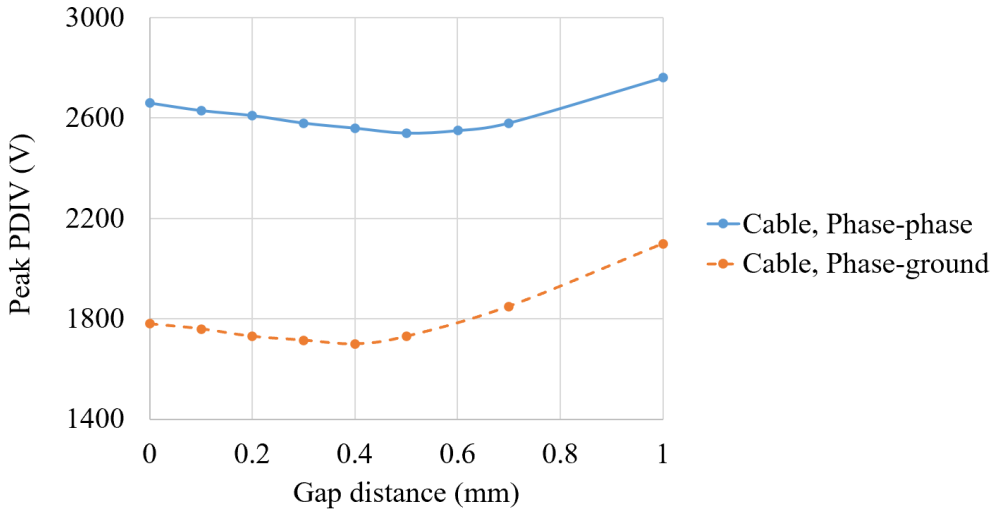

Figure 5.7 PDIV of an AWG 4/0 cable with 1 mm insulation thickness under 0.238 bar.

Figure 5.8 compares the PDIV between the phase-ground geometry and phase-phase geometries of busbars in vertical positions. The conductor cross-section area, insulation thickness and operating pressure of the busbar are the same as the cable in Figure 5.7. The busbar has an aspect ratio of 5 and a fillet radius of 0.1 mm. Compared to the PDIV for the phase-ground geometry, the minimum PDIV for the phase-phase geometry is approximately 50% higher. The minimum equivalent phase-ground PDIV for the phase-phase geometry is around 14% lower than the phase-ground geometry. These results indicate that the safe operating voltage of busbars is also determined by phase-phase geometry, a similar result to the cables.

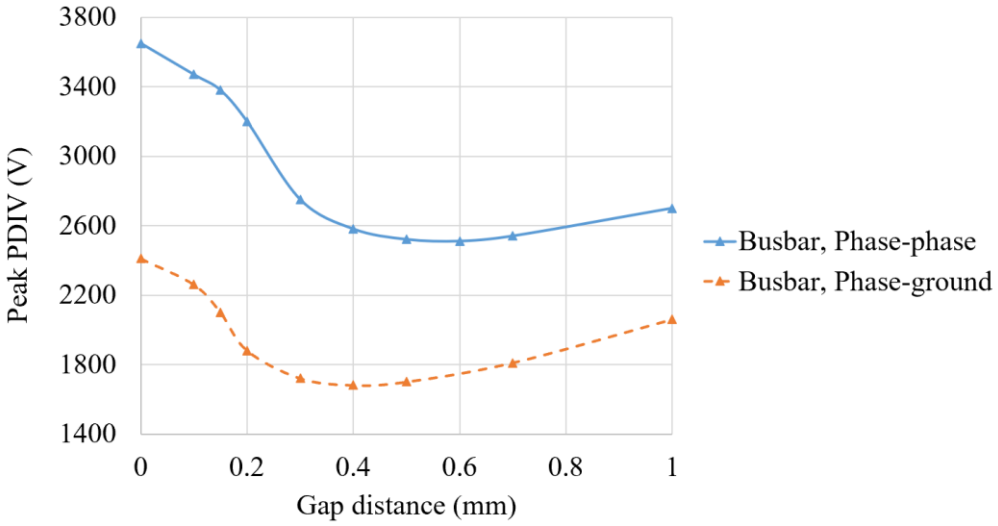

Figure 5.8 PDIV of a busbar (aspect ratio=5) with the same cross-section area of AWG 4/0 cable with 1 mm insulation thickness under 0.238 bar of pressure.

Figure 5.9 compares the equivalent phase-ground PDIV for the phase-phase geometry between cables and busbars. If there is no gap between the two phases, the busbar PDIV (2107 V) is around 37% higher than the cable (1536 V). In this scenario, partial discharge occurs at the air gaps around the corner of busbars. The fillet radius of the busbar is 0.1 mm. Therefore, the busbar corner can be regarded as two touched cables with a conductor diameter of 0.2 mm. When the conductor diameter increases, more of the electric field is distributed in the insulation material and less distributed in the air, leading to a larger PDIV. The effect of conductor diameter on the PDIV is discussed in detail in section 5.3.2.

The minimum PDIV for the busbar is approximately 1449 V and the minimum PDIV for the cable is around 1466 V. The difference between the minimum PDIV of the cable and the busbar can be negligible. Once the PDIV reaches the minimum, increasing the gap distance can increase the PDIV continuously and bring thermal aspect benefits, but require more space to do so.

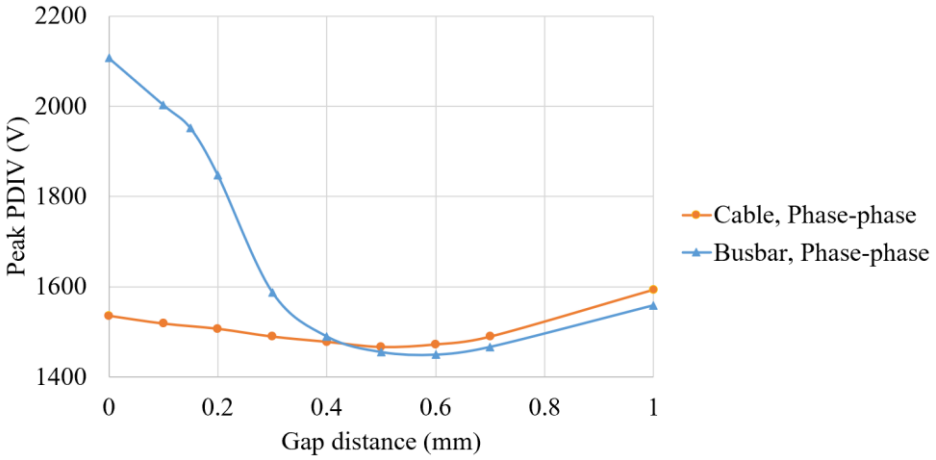

Figure 5.9 Comparison of equivalent phase-ground PDIV for phase-phase geometry of an AWG 4/0 cable and a busbar (aspect ratio=5) with the same cross-section area with 1 mm insulation thickness under 0.238 bar of pressure.

5.3.2 Effect of Conductor Geometry

In SAE AS50881, the PDIV is only forecast on the basis of an equivalent insulation thickness and operating environment. The effect of conductor diameter is not considered. Figure 5.10 shows effect of conductor diameter on the equivalent phase-ground PDIV of phase-phase geometry for cables. The insulation thickness is 1 mm and pressure is 0.238 bar. The results show that the PDIV versus gap distance has a similar trend for the four conductor sizes. At constant gap distances, the PDIV increases with a decreasing conductor diameter. When the conductor diameter is reduced from 11.68 mm to 8.25 mm, 5.19 mm and 2.05 mm, the minimum PDIV is increased by 1%, 2% and 8%, respectively.

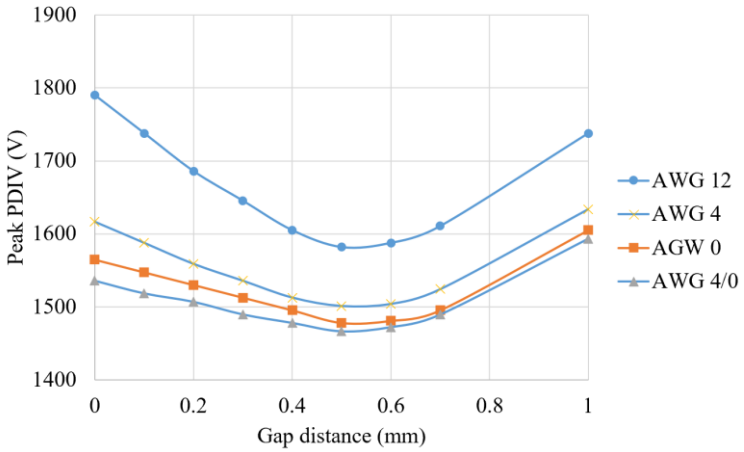

Figure 5.10 The effect of conductor size on cable PDIV with a thickness of 1 mm under a pressure of 0.238 bar.

Figure 5.11 displays the electric field distribution along a gap distance of 0.5 mm between two conductors when the applied equivalent phase-ground voltage is 1500 V and insulation thickness is 1 mm. When the conductor diameter decreases from 11.68 mm to 2.05 mm, the average electric field on the insulation increases from 0.86 kV/mm to 0.88 kV/mm and the average electric field on the air decreases from 1.77 kV to 1.64 kV/mm. Even though the reduced conductor diameter leads to a more non-uniform electric field, more electric field strength is seen in the insulation material. The decrease in electric field strength in air explains the increasing PDIV caused by the decreasing conductor diameter.

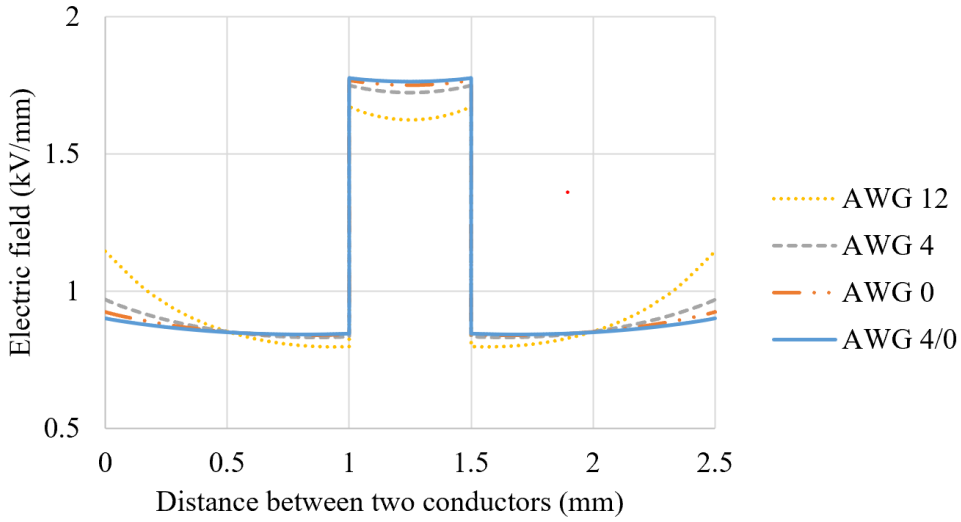

Figure 5.11 Electric field distribution between two conductors when the gap distance is 0.5 mm and applied equivalent phase-ground voltage is 1500 V.

Figure 5.12 shows the effect of conductor cross-section area on the PDIV of busbars. The four busbars have the same aspect ratio of 5, the same fillet radius of 0.1 mm and the same insulation thickness of 1 mm under 0.238 bar of pressure. When the gap distance is below 0.2 mm, partial discharge occurs at the edge of busbars. The PDIV of the AWG 12 busbar is up to 4% higher than other busbars. Even though four busbars have the same fillet radius, the electric field of the AWG 12 busbar is more non-uniform due to the thinner conductor. The non-uniform electric field leads to a higher PDIV, as more electric field is seen in the insulation material. Figure 5.13 displays the electric field distribution of busbars with an identical conductor cross-section area to AWG 12 and AWG 4/0. When the gap distance is above 0.2 mm, the location of partial discharge moves from the edge to the centre. The electric field around the busbar centre is not

affected by the conductor cross-section area. Therefore, the minimum PDIV is not affected by the cross-section area of busbars.

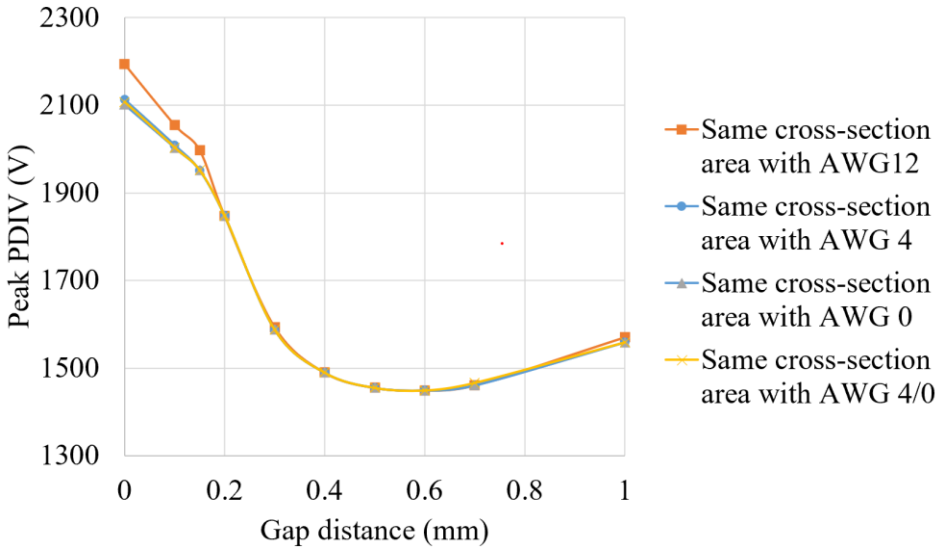

Figure 5.12 The effect of conductor cross-section area on the PDIV of busbars with an insulation thickness of 1 mm under a pressure of 0.238 bar.

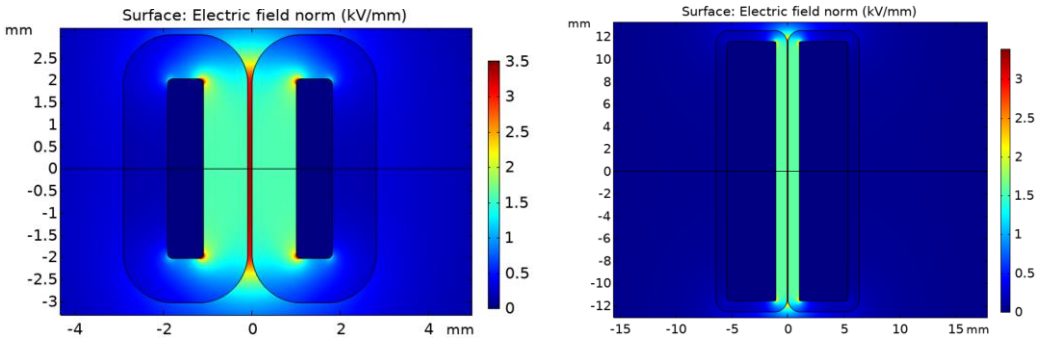

(a) (b)

Figure 5.13 Electric field distribution for busbars with the identical conductor cross-section area with (a) AWG 12 and (b) AWG 4/0 when the applied equivalent phase-ground voltage is 2000 V.

Figure 5.14 shows the effect of fillet radius on PDIV. The results indicate that increasing the fillet radius leads to a decrease in the PDIV when partial discharge occurs at the corner of busbars, which is counterintuitive. The reason is that the corners of busbars have a similar geometry to round cables. The increasing fillet radius of busbars is equivalent to increasing the conductor diameter of cables. The non-uniform concentration of electric field in the insulation reduces and the electric field strength in the air increases, which results in a lower PDIV. When the partial discharge occurs on the centre of busbars as the gap distance increases, the effect of the radius fillet on the

PDIV is negligible. Therefore, the minimum PDIV of busbars is not affected by fillet radius. However, it could still impact dielectric breakdown strength.

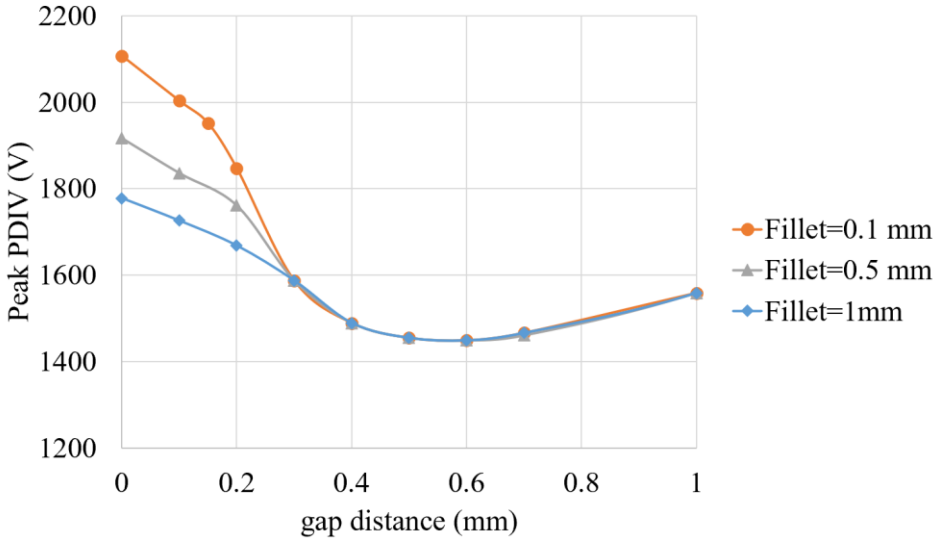

Figure 5.14 The effect of fillet size on busbar PDIV with an insulation thickness of 1 mm under a pressure of 0.238 bar.

5.3.3 Effect of Insulation Thickness and Permittivity

Figure 5.15 shows the effect of insulation thickness and permittivity on the minimum equivalent phase-ground PDIV for the phase-phase geometry of cables and busbars under 0.238 bar. The diameter of the cable is 11.68 mm. The busbar has the same cross-section area of the cable with a fillet radius of 0.1 mm. Increasing insulation thickness leads to a higher PDIV for both cables and busbars. When the insulation thickness increases from 1 mm to 5 mm, the percentage difference of PDIV between cables and busbars increases from 1% to 5%, which is much smaller than the percentage difference of current carrying capacity between them (approximately 19% at 2000 Hz). When insulation thickness is increased from 1 mm to 2 mm, the PDIV increases from 2510 V to 3980 V for busbars with a permittivity of 2.1. This means when the operating voltage is doubled, the insulation thickness should be more than double to ensure safe operation, leading to a higher volume and weight of the interconnection system.

The results also show that a lower permittivity provides a higher PDIV due to the higher percentage of voltage distributed in the air gap. When permittivity decreases from 4.5 to 2.1, the PDIV of the cable increases by approximately 60% for cables and busbars when the insulation thickness is 1 mm. Furthermore, lower permittivity provides a higher increasing slope for the relationship between PDIV and insulation thickness.

Therefore, insulation material with a lower permittivity, such as PTFE, can be applied to increase the safe operating voltage.

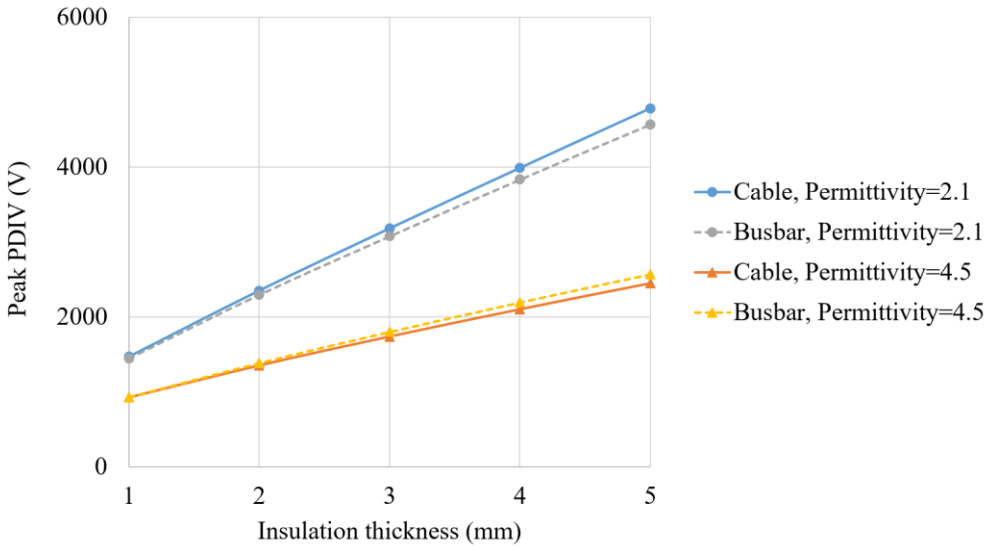

Figure 5.15 The effect of insulation thickness and permittivity on the PDIV of the AWG 4/0 cable and the busbar with the same conductor cross-section area and a fillet radius of 0.1 mm under 0.238 bar of pressure.

5.3.4 Effect of Pressures on PDIV

Figure 5.16 shows the effect of pressure on the minimum equivalent phase-ground PDIV for the phase-phase geometry of cables and busbars with an insulation thickness of 1 mm and a relative permittivity of 2.1. The results show that the PDIV increases with pressure regardless of conductor geometry. Decreasing pressure leads to a lower gas density and a longer free path between gas molecules, which means a lower voltage is needed to accelerate the electronics to an ionising velocity. Therefore, a lower electric field strength is required to initiate gas discharge and thus a lower PDIV.

As discussed in Section 5.3.2, increasing the conductor diameter results in a lower PDIV, with the effect of busbar geometry on the minimum PDIV being negligible. When the conductor increases from AWG 12 to AWG 4/0, the PDIV decreases by 7%. The PDIV of the AWG 4/0 cable is almost equivalent to the PDIV of the busbar. The SAE AS50881 has an approximately 8% higher PDIV when compared to the AWG 12 cable and 15% compared with the AWG 4/0 cable.

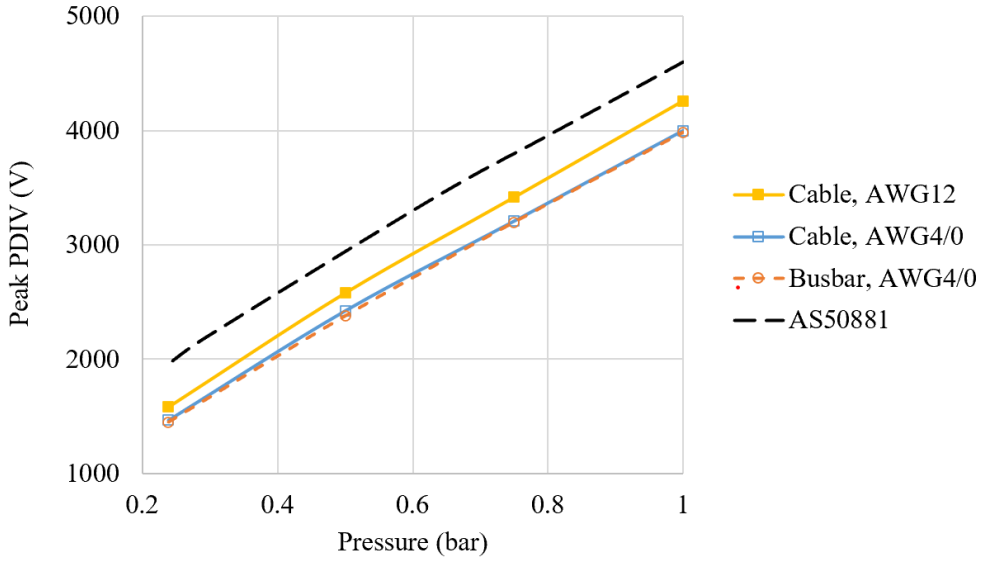

Figure 5.16 The effect of pressure on the PDIV of cables and busbars with an insulation thickness of 1 mm and a relative permittivity of 2.1 under 0.238 bar of pressure.

5.4 Summary

This chapter has described the simulation of the safe operation voltage of unscreened cables and busbars under various conditions. Both phase-phase and phase-ground geometries were compared. The effect of parameters on the PDIV, such as conductor geometry, insulation thickness, relative permittivity and pressure, were investigated. The limitation is a lack of experimental work to measure PDIV and compare them with simulation results. The contributions are summarised in the following:

- For both cables and busbars, the safe operating voltage is determined by the minimum PDIV of the phase-phase geometry. When the gap distance between phases increases, the PDIV initially decreases to a minimum value before increasing. In modelling using FEM techniques and the streamer electrification technique, it is therefore important to run the model at a range of gap distances.
- When the conductor diameter decreases from AWG 4/0 to AWG 12, the minimum PDIV increases by approximately 6% with an insulation of thickness of 1 mm under 0.238 bar of pressure. Concerning the busbars, the effect of conductor geometry on the minimum PDIV can be negligible.

- For both cables and busbars, increasing the relative permittivity of insulation results in a lower PDIV. However, due to the limited range of permittivity values, its sensitivity is not as large as the insulation thickness, especially under low pressures. Insulation thickness is the most sensitive parameter to determine the PDIV.
- The PDIV difference between the AWG 4/0 cable and the busbar with an equivalent cross-section area is within 5% under 0.238 bar of pressure.
- The SAE AS50881 has an approximately 8% higher PDIV at 0.238 bar when compared to the AWG 12 cable and 15% when compared with the AWG 4/0 cable when insulation thickness is 1 mm and relative permittivity is 2.1.
- Overall, the use of busbars as opposed to round cables does not appear to have any significant risk in terms of voltage rating. The benefit in current carrying capacity discussed in the previous chapter is not offset by a reduction in voltage rating.

Chapter 6 Stress Grading System for Screened Cables

6.1 Introduction

In conventional aircraft, unscreened cables are currently used to carry power due to their low voltage levels. As future aircraft will require higher voltage levels, screened cables may be considered as they can prevent partial discharge while keeping insulation thicknesses manageable (in terms of weight). However, the cable termination of a screened cable is a weak point because there is a sharp edge around the cable shield end, creating a high electric field. In order to avoid partial discharge and eventually insulation failure, the electric field around the cable termination should be controlled to a safe level. Stress grading, also denoted as electric field grading, refers to the active control of the electric field distribution and is the approach mainly applied in conventional power systems to manage the risk of failure associated with excessive longitudinal electric fields.

For ground power cables, several methods have been applied to achieve electric field grading at cable termination interfaces, such as geometrical stress control based on electrode contours, refractive stress control based on high permittivity material and resistivity stress control based on semiconductive coating or tape with specific resistance values [121]. However, the application of the stress grading design on aerospace cables has not been investigated. In aircraft, stress grading tape is a better choice than a geometric stress cone as weight/volume is an important factor during design. Since the working condition of both ground and aerospace cables differ, there are still research gaps on the influence of pressure, temperature and frequency in the design of stress grading systems.

The partial discharge inception electric field strength along the cable termination surface has been studied at power frequency and atmospheric pressure. The value of the longitudinal electric field suitable to avoid partial discharge is stated to be between 0.4 kV/mm and 0.6 kV/mm [121]. However, the value of the inception electric field under the aerospace environment has not been investigated and it seems logical that this should reduce as a function of pressure. In order to determine the suitable stress grading material properties for aircraft cables, the inception electric field under aerospace environment should be researched. This study investigates the partial discharge electric field along the cable termination surface in the aerospace environment and the effect of

stress grading material properties on the electric field strength and distribution around the cable termination. This chapter initially describes the test samples used in this study. The test samples are made of an aerospace cable, with nonlinear resistivity stress grading tape put on cable terminations. The partial discharge test setup and test procedures are then presented, followed by a description of the electric field simulation model to obtain the electric field distribution along the cable termination surface. After that, the effects of the stress grading system on the PDIV of cable terminations are presented and the partial discharge inception electric field under various frequencies and pressures is presented discussed. Finally, the effect of stress grading material properties on the electric field distribution are discussed.

6.2 Experimental Setup and Modelling of the Samples

6.2.1 Sample Preparation

The test sample is an unscreened ETFE-insulated cable from the company TE Connectivity. The diameter of the cable is 11 mm, insulation thickness is 1.5 mm and the cable length 400 mm. A single layer of aluminium tape was wrapped around the centre of the cable to simulate a screen layer. At the end of the metal tape, a single layer of the stress grading tape Vonroll SC 217.31 overlaps the metal tape layer as shown in Figure 6.1. An illustration of the test sample is presented in Figure 6.2.

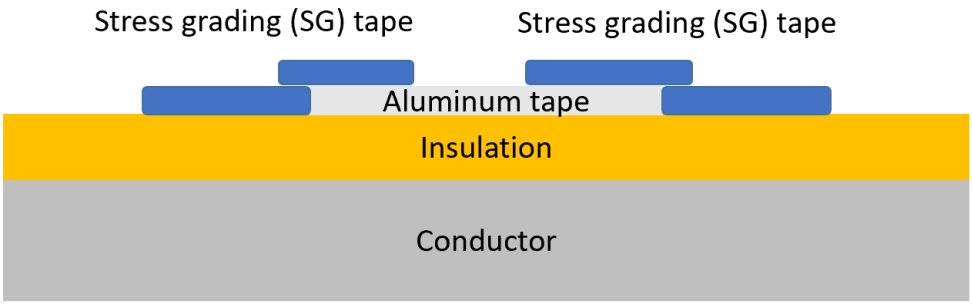

Figure 6.1 Diagram of the cable termination construction with a stress grading system.

Figure 6.2 Test sample configuration.

6.2.2 Electrical Conductivity Measurement under DC

The conductivity of a stress grading system is an important parameter affecting the electric field distribution. As it is not provided by the supplier, the conductivity needs to be measured to make sure the electric field simulation is accurate. Small samples of tape were used to understand its characteristics. Metal tape overlaps the stress grading tape ends and the distance between the metal tapes is set as 20 mm and 5 mm respectively to measure the conductivity under various DC electric fields as shown in Figure 6.3.

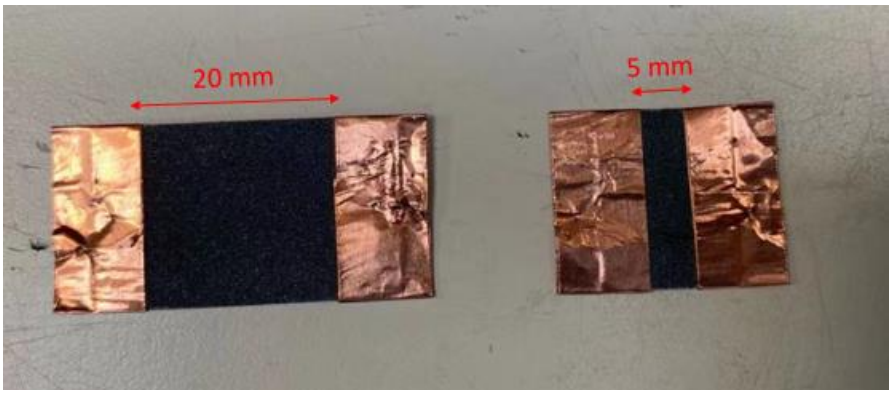

Figure 6.3 Diagram of conductivity measurement samples under DC.

The conductivity measurement circuit initially used is shown in Figure 6.4. The DC power source (Glassman FC30 with 0.1% accuracy) is used to provide variable voltages [122]. The voltage across the sample is measured by the HV probe (ratio 1000:1) and

the current through the sample is measured by a highly sensitive ammeter (Keithley 6485 with a current range between 2 nA and 20 mA with a 10^{-5} nA resolution) [123]. The maximum test voltage is 5 kV and a 270 kΩ resistor is used to protect the equipment by limiting the current above 19 mA. The conductivity of the stress grading material under various electric fields can be calculated by the measured V-I characteristics.

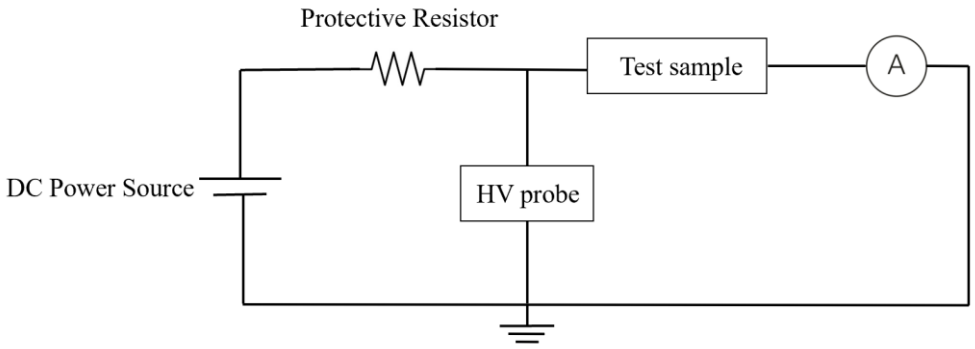

Figure 6.4 Conductivity measurement setup under DC.

6.2.3 Electrical Conductivity Measurement under AC

As the stress grading material operates under AC, it is also important to investigate if the voltage type and frequency affect the electrical conductivity of stress grading material. The conductivity of stress grading material is traditionally measured by applying an electric stress between two circumferential electrodes. The diagram of the conductivity measurement specimen is shown in Figure 6.5. Metal tapes overlapped the stress grading tape ends on a circumferential plastic tube (that is hollow to minimise the stray capacitance between the metallic electrodes). The diameter of the plastic tube is 25 mm and the distance between the metal tapes is set as 5 mm.

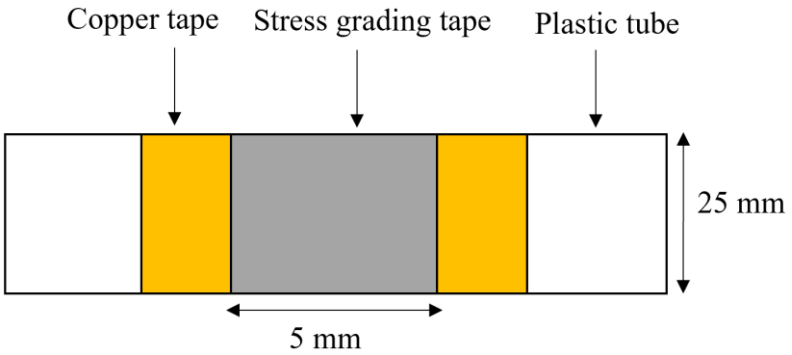

Figure 6.5 Diagram of conductivity measurement specimen under AC.

The conductivity measurement circuit under AC is shown in Figure 6.6. The AC power supply consists of a function generator controlled by LabVIEW and a high voltage

amplifier, which can generate voltages under various frequencies. The AC output is generated for a second to avoid overheating of test sample. The voltage across the sample is measured by the HV probe (ratio 10000:1) and the current through the sample is calculated by dividing the voltage through the current shunt and the resistance of them. The current shunt consists of three parallel 330 kΩ resistor and parallel with back to back Zener diodes to ensure the voltage being delivered into the oscilloscope is not excessive. A high sensitivity oscilloscope is used to measure and record the voltage value from the voltage divider and the current shunt.

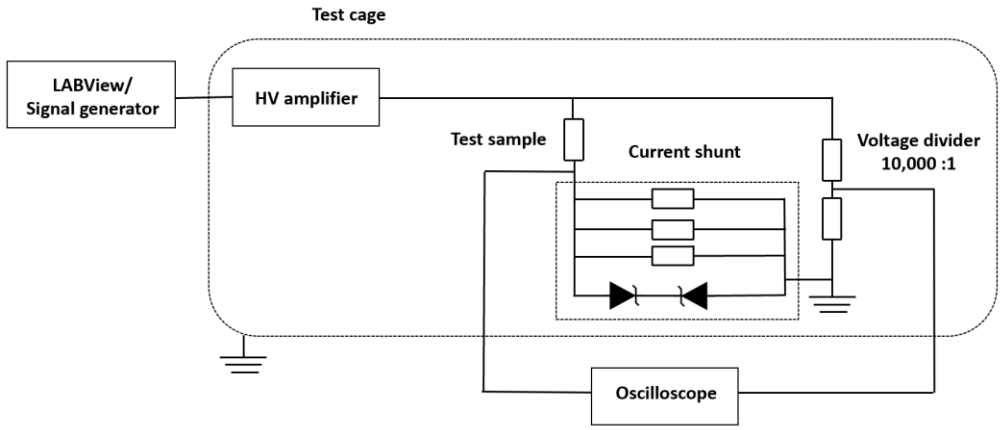

Figure 6.6 Conductivity measurement setup under AC.

6.2.4 Partial Discharge Measurement

As Figure 6.7 shows, the partial discharge experiment setup is composed of three parts: an environmental chamber, high voltage supply system and measurement unit. The size of the environmental chamber is 0.6m*0.6m*0.6m and can produce a low-pressure environment as low as 0.2 bar. The test sample was placed in the centre of the test chamber to avoid electric discharge between the high voltage conductor and the wall of the environment chamber. Before the partial discharge test commenced, the pressure was reduced to a required value and lasted for 5 minutes to make sure the pressure inside the chamber was stable.

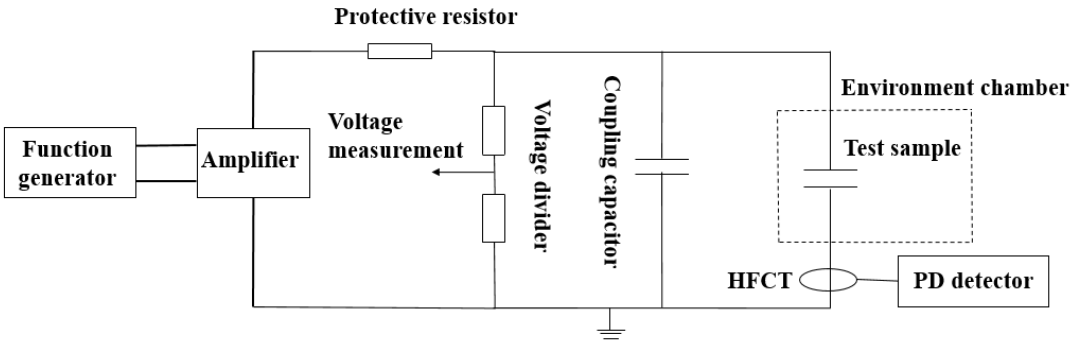

Figure 6.7 Partial discharge measurement setup.

The power supply consists of a function generator and an amplifier, which can provide voltages up to 4 kV rms at 50 Hz and 2 kV rms at 1000 Hz. This value being limited given the amplifier can produce a maximum of 10mA. A 1000 pF coupling capacitor was connected in parallel with the sample to provide a path for the pulse current signal caused by PD activities. A protective resistor was used to protect the circuit when breakdown occurs. To measure the voltage across the test sample, a capacitive divider with a ratio of 10,000:1 was connected in parallel with the test sample and the voltage signal obtained from an oscilloscope.

The commercial PD detector Omicron MPD 600 was connected with a high-frequency current transformer Omicron MCT120 to detect the PD activities. The centre frequency was 250 kHz and the bandwidth in the range between 100 kHz and 400 kHz, which is consistent with the standard IEC 60270-2010 [124]. The PD threshold was set as 15 pC due to the background noise being controlled around 7 pC.

Both temperature and humidity were recorded during the test. The temperature was in the range between 21 ^{o}C and 26 ^{o}C, with the humidity in the range between 50% and 52%. Thus, the effect of temperature and humidity variations on the partial discharge activity would be negligible. The test frequency was in the range between 50 Hz and 1000 Hz, and the test pressure in the range between 0.238 bar and 1 bar. The increasing voltage step was set as 100 V/s until continuous a PD signal was detected, which will be regarded as the PDIV. The time interval between each test was set as 1 minute. In order to ensure repeatability, five tests were conducted under the same test conditions and three stress grading tapes applied.

6.2.5 Numerical Simulation

In addition to the experimental tests, a COMSOL model was used to convert the results of the PDIV measurements to a longitudinal value of electric field. This section presents methods for simulating electric field along the stress grading system under various frequencies. The dimension of the model is shown in Figure 6.8. It represents the cable under test described in the earlier section.

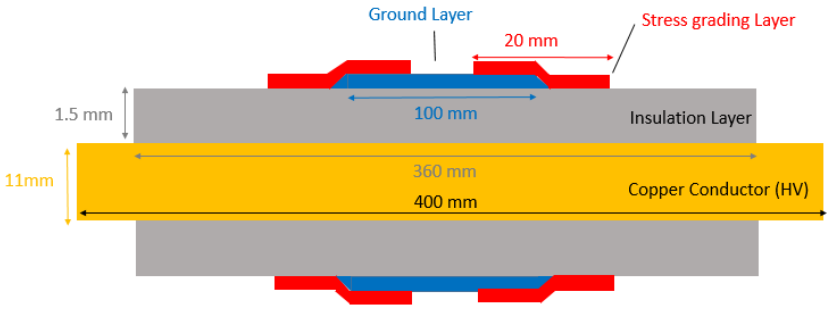

Figure 6.8 Dimension of cable termination with stress grading system.

As the test sample is coaxial-symmetric, a 2D model is used for the simulation as shown in Figure 6.9. The conductor is set as the high voltage potential. The ground layer is set as ground potential. In this study, interactive meshing was applied to generated finer mesh in the area with sharp edge, which makes it easier to control the size and elements of the mesh.

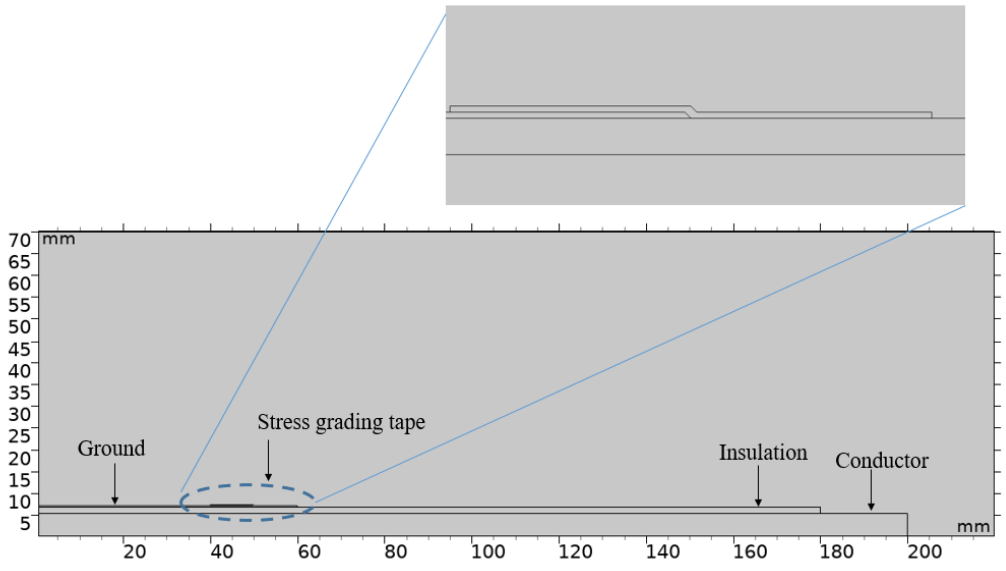

Figure 6.9 2-D model of stress grading system

The conductor, insulation and ground materials are copper, ETFE and aluminium, respectively. The cable is surrounded by air. The electric properties of these materials are shown in Table 6.1. The conductivity of stress grading tape depends on electric field. The values of σ_0 and α represent initial conductivity and nonlinear resistivity. The test setup for these values has been described in section 6.2.2 and the measurement results are shown in section 6.3.1.

Table 6.1 Material properties applied in the model

	Electric conductivity (S/m)	Relative permittivity
Copper [105]	$5.998*10^7$	1
ETFE [125]	10^{-14}	2.6
Aluminium [105]	$3.774*10^7$	1
Air	-	1
Stress grading tape	$\sigma(E) = \sigma_0 \exp(\alpha \times E)$	4.5

The simulation model solves the partial differential equations based on Maxwell's electromagnetic theory, which can be expressed using Equation 6.1 and Equation 6.2:

$$\nabla \times E = -\frac{\partial B}{\partial t} \tag{6.1}$$

$$\mathrm{J} = \sigma E + \frac{\partial D}{\partial t} + J_e \tag{6.2}$$

Where E is electric field (V/m), B is magnetic flux density (T), J is current density (A/m^2), σ is conductivity (S/m) and D is electric displacement (C/m^2).

6.3 Results

6.3.1 Conductivity of Stress Grading Tape

Using the stress grading tapes and setup shown in Figure 6.3 and Figure 6.4 respectively, the voltage and current of stress grading tape were recorded to analyse the electrical conductivity under DC voltages. Figure 6.10 and Figure 6.11 illustrate voltage-current measurement results for the two samples. As the voltage increases, the electric field strength across the stress grading tape increases linearly, with the conductivity of the stress grading tape increasing exponentially. Therefore, the current through the circuit increases exponentially.

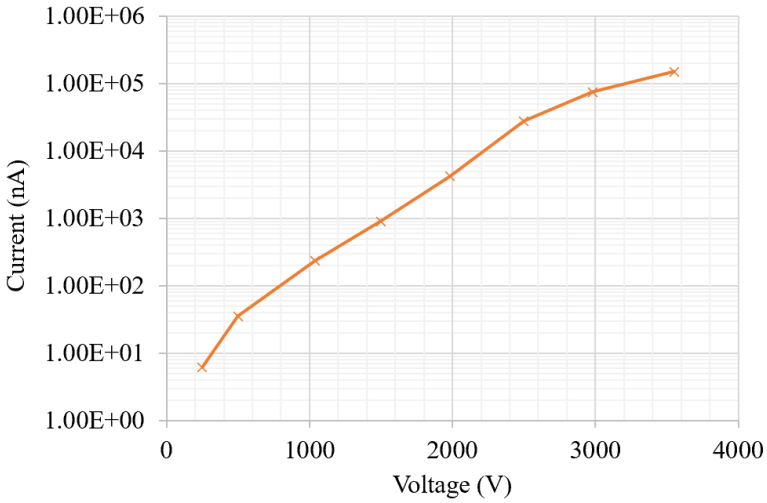

Figure 6.10 The relationship between voltage and current for the 5 mm stress grading tape.

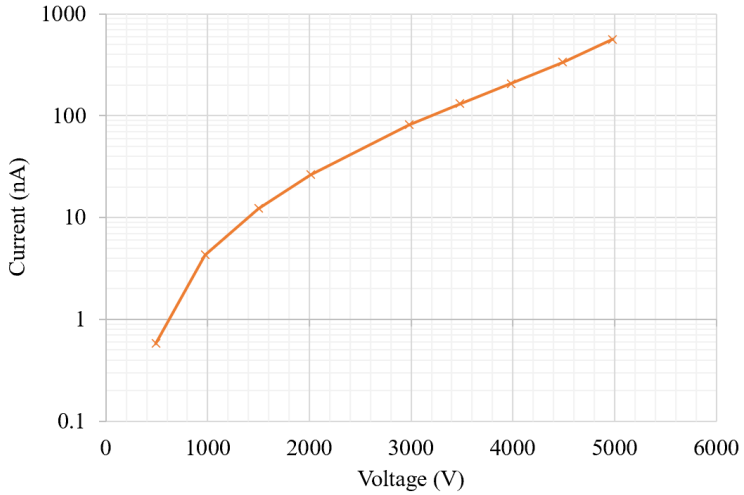

Figure 6.11 The relationship between voltage and current for the 20 mm stress grading tape.

Using the stress grading tapes and setup shown in Figure 6.5 and Figure 6.6 respectively, the voltage applied on the stress grading tape and the current shunt were then recorded for the AC case. The current through stress grading tape can be calculated by diving the voltage across the current shunt and the total resistance (110 kΩ). The electrical conductivity of stress grading tape under AC voltages was calculated by dividing the peak values of voltage by peak values of current across the stress grading material. Figure 6.12 shows the voltage and current under 50 Hz when the applied peak-peak voltage on stress grading increases from 1000 V to 7000 V. When the voltage increases from 1000 V to 7000 V, the phase difference between the voltage peak value and current peak value continuously decrease from 67 degree to 1 degree. The reason is that when the voltage increases, the conductivity of the stress grading material increases.

Therefore, the conductive current increases and accounts for a larger percentage of the apparent current that is consisting of resistive current and capacitive current. The non-sinusoidal current is a result of the conductivity change of stress grading material under various applied voltage levels.

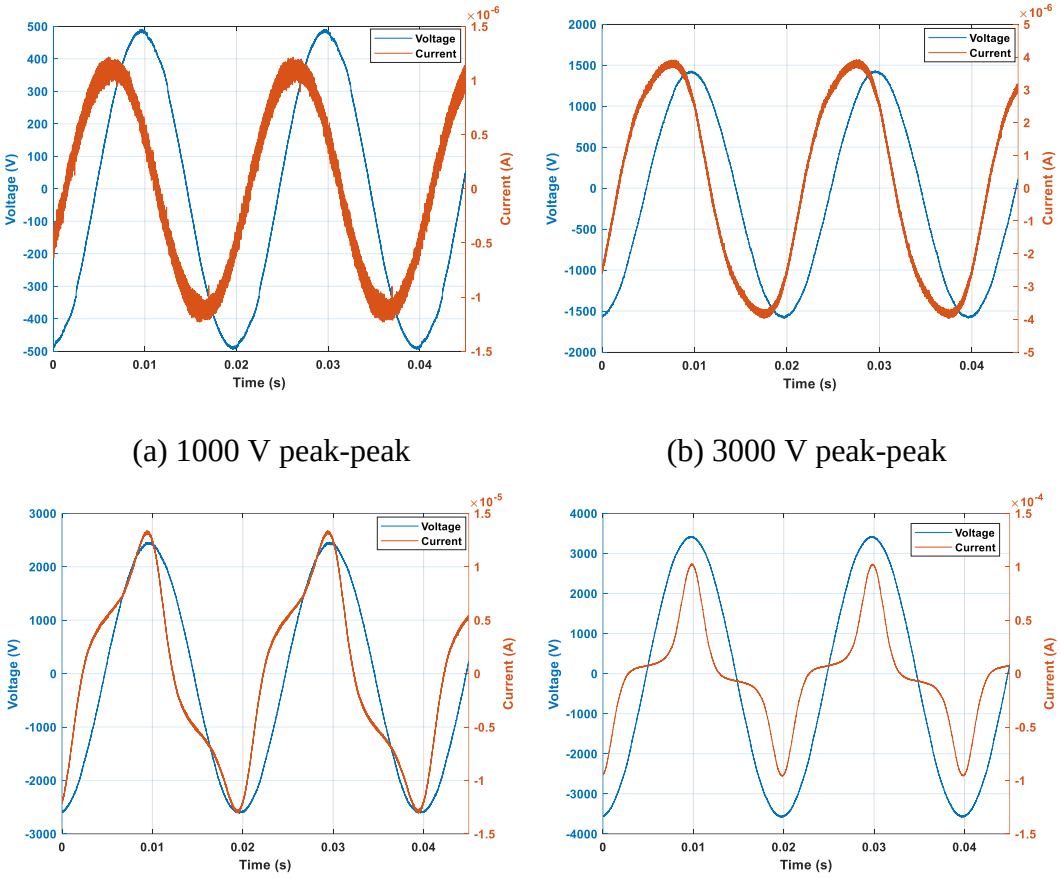

(a) 1000 V peak-peak

(b) 3000 V peak-peak

(c) 5000 V peak-peak

(d) 7000 V peak-peak

Figure 6.12 Voltage and current waveform under 50 Hz.

Figure 6.13 shows the voltage and current under 500 Hz when the applied peak-peak voltage on stress grading increases from 1000 V to 7000 V. When the voltage increases from 1000 V to 5000 V, the phase difference between the voltage peak value and current peak value keeps constant at around 67 degrees. When the voltage increases from 5000 V to 7000 V, the phase difference decreases from 67 degree to 1 degree. The reason may be that the conductivity of stress grading material keeps constant until the applied voltage is higher than 5000 V and then rapidly falls.

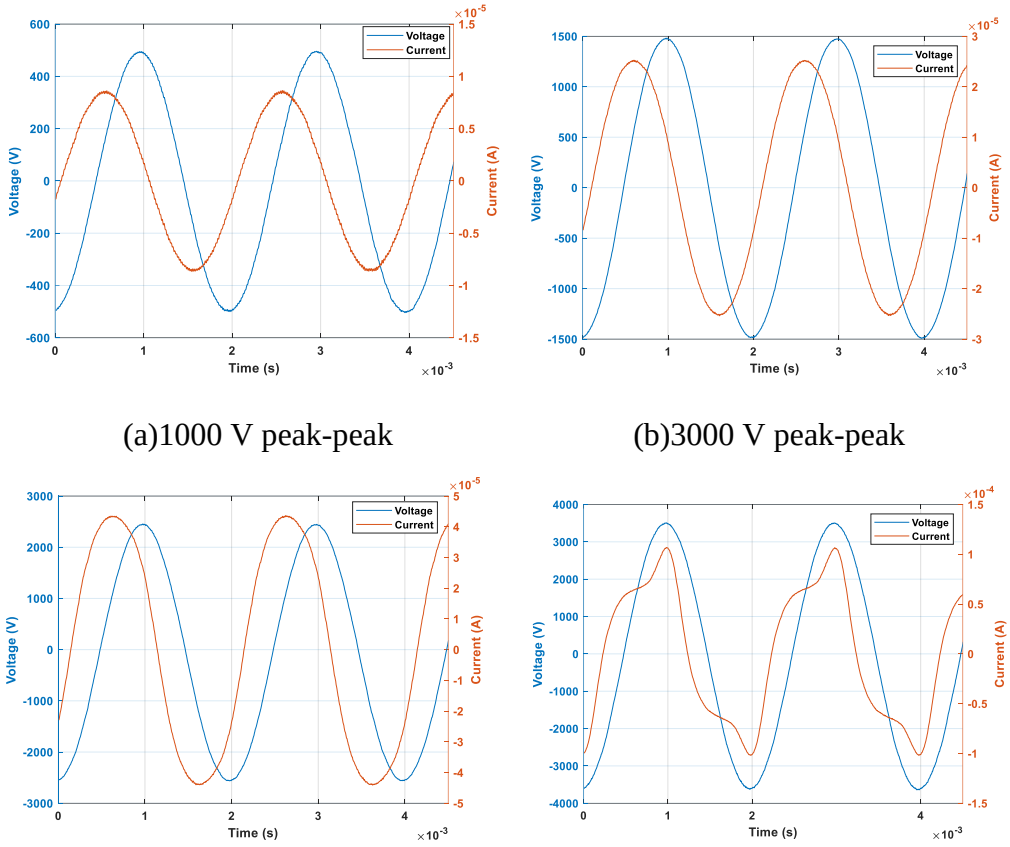

(a)1000 V peak-peak (b)3000 V peak-peak

(c) 5000 V peak-peak (d) 7000 V peak-peak

Figure 6.13 Voltage and current waveform under 500 Hz.

Figure 6.14 provides a summary of both the AC and DC conductivity as a function of electric field strength. The AC conductivity was calculated by considering the phase difference between voltage and current. When the electric field is above 0.5 kV/mm, the conductivity measured under DC is higher than that measured under AC. The likely reason is that the tape heats up under the DC continuous current and becomes more conductive under a high electric field. As such, the results from the AC tests are more likely correct in this region. The conductivity of stress grading material increasing with increasing temperature is shown in [94].

The conductivity under AC keeps constant firstly and then increases exponentially as a function of electric field. When the frequency increases, the constant values of conductivity increases as a result of higher capacitive current – this is consistent with the experimental values in previous research. The switching electric field where conductivity increases exponentially also increases with increasing frequency. It is not clear why this takes place based on a review of existing literature. However, it could be

associated with the difficulty in seeing an increase in resistive current flow when the capacitive current level is high.

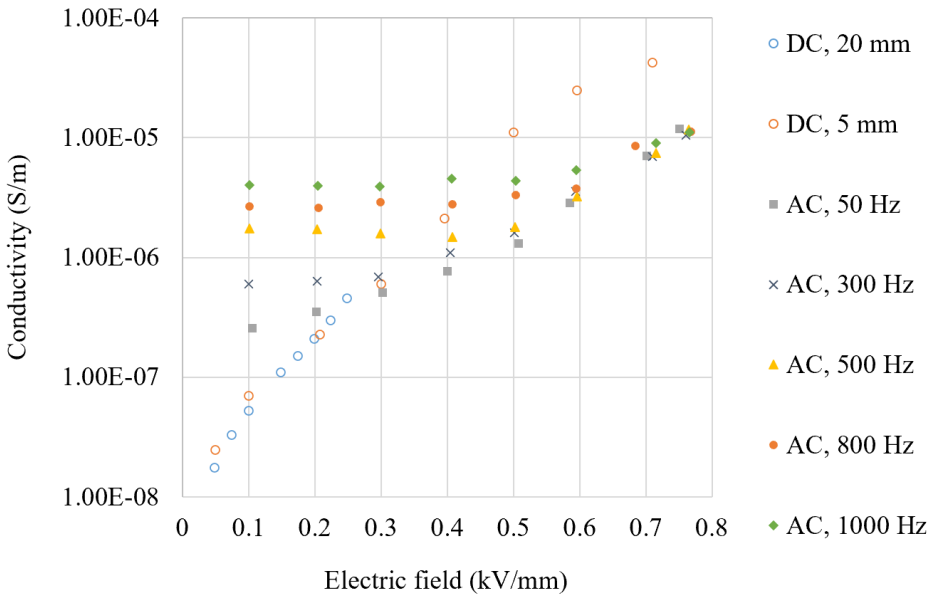

Figure 6.14 The relationship between conductivity and electric field for the stress grading tape under both DC and AC.

By removing the DC results above 0.3 kV/mm that may be affected by temperature and the AC values when the electric field is lower then the switching point, the fitting curve is shown in Figure 6.15 and it can be expressed as Equation 6.3.

$$\sigma(E) = 4 * 10^{-8} \exp(7.74 \times E) \tag{6.3}$$

where σ is conductivity (S/m) and E is electric field (kV/mm).

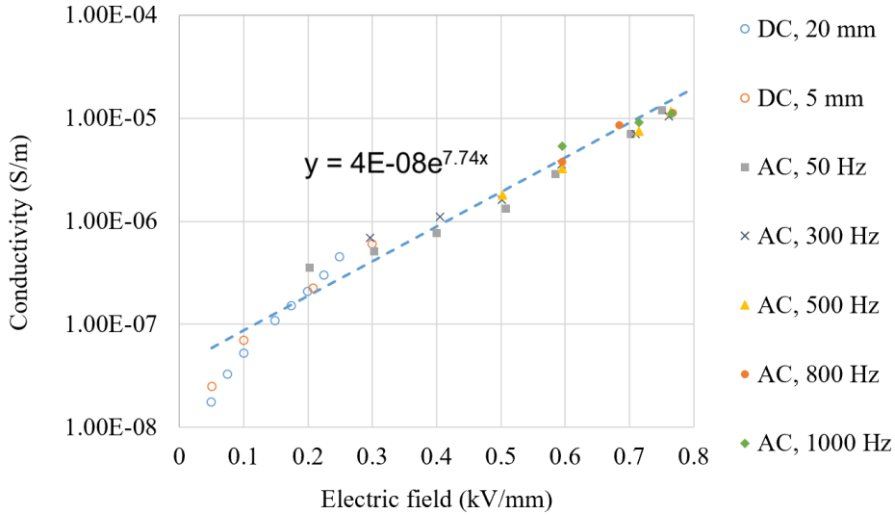

Figure 6.15 The fitting curve between conductivity and electric field for stress grading material.

6.3.2 Partial Discharge Inception Voltage

This section discusses the effect of pressure and frequency on the PDIV of cable terminations as measured in experiments with and without stress grading tape. Figure 6.16 compares the PDIV of cable terminations with and without stress grading tape under various frequencies and pressures. The experimental results show that the PDIV decreases when the pressure reduces from 1 bar to 0.238 bar in all cases. This suggests that the magnitude of the longitudinal electric field required for partial discharge to take place is reducing as a function of pressure.

When the frequency increases from 50 Hz to 1000 Hz, the PDIV without stress grading tape remains almost constant, while the PDIV with stress grading tape initially decreases rapidly and then changes slowly. The stress grading tape increases the PDIV between 26% and 55% under 1 bar, and between 15% and 30% under 0.238 bar.

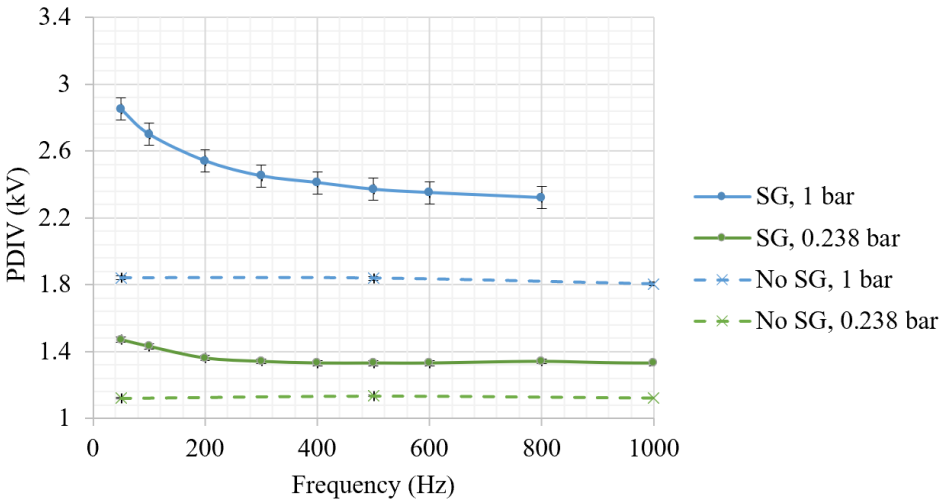

Figure 6.16 A comparison of PDIV between cable termination with and without stress grading tape.

The effect of frequency on the PDIV without stress grading material can be explained by the equivalent circuit shown in Figure 6.17. The voltage distribution between HV and the ground depends on impedance distribution. For the cable termination without a stress grading system, horizontal impedance depends on the air capacitor and vertical impedance on the insulation capacitor. When the frequency changes, the vertical impedance and horizontal impedance ratio remains constant. Thus, the electric field remains constant, which explains why the PDIV remains constant when the frequency changes.

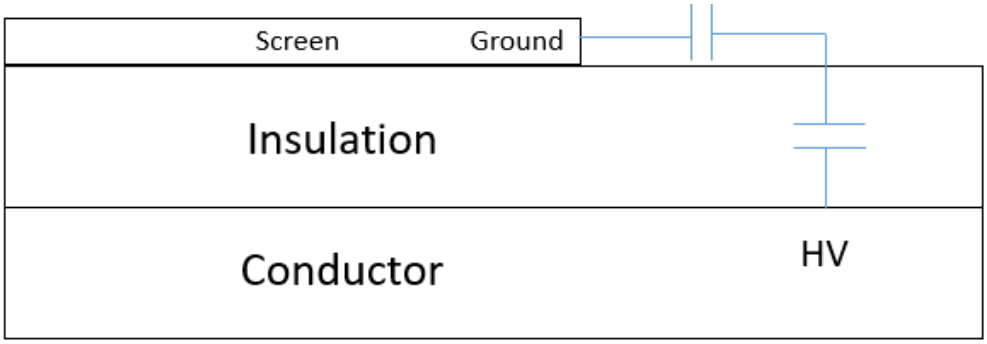

Figure 6.17 Equivalent cable termination circuit without a stress grading system.

Figure 6.18 shows the equivalent circuit for cable termination with stress grading material. The impedance of stress grading material consists of resistance and capacitance. When the frequency increases, the impedance ratio of the stress grading system to the insulation increases. Thus, the voltage distributed in the stress grading material and the electric field along the cable termination both increase, which explains the decreasing PDIV with increasing frequencies. The nonlinearity of the SGT material will partly compensate for frequency but there is still some impact.

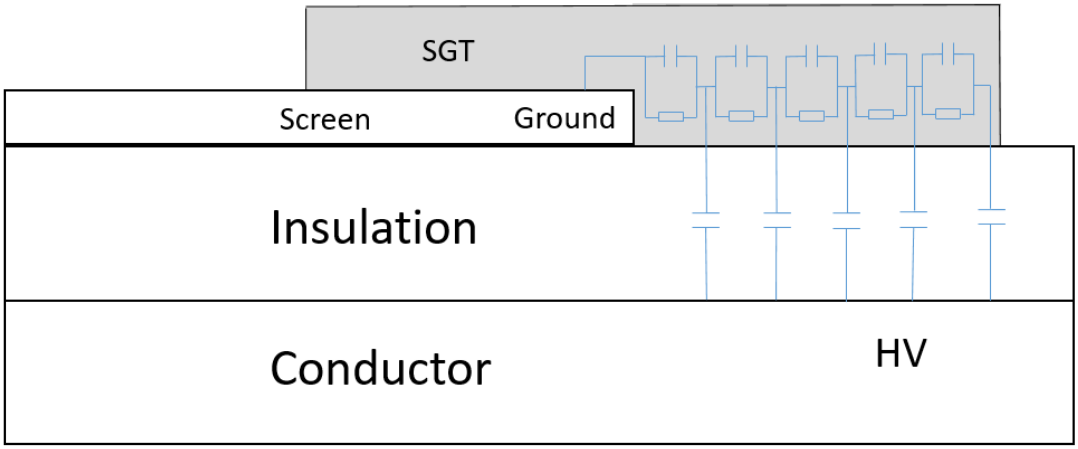

Figure 6.18 Equivalent cable termination circuit with a stress grading system.

6.3.3 Inception Electric Field Simulation

According to the CIGRE brochure namely field grading in electrical insulation systems, the PDIV of the surface discharge along cable termination is determined by the longitudinal electric field along the surface. Therefore, it is necessary to understand the longitudinal electric field under the PDIV to discuss the effect of pressure and frequency on partial discharge inception electric fields. The longitudinal electric field distributions along the stress grading surface at 1 bar, 0.5 bar and 0.238 bar are shown

in Figure 6.19 and Figure 6.20 respectively. These curves were generated by placing measured PDIV values into COMSOL stress grading model. The position of conductive layer is from 0 to 10 mm and the position of stress grading layer is from 0 to 20 mm. The field is more optimally graded in the 50Hz case where the peak values at the start and end of the SGT more evenly match, this is likely a result of the use of a tape designed for a 50Hz application.

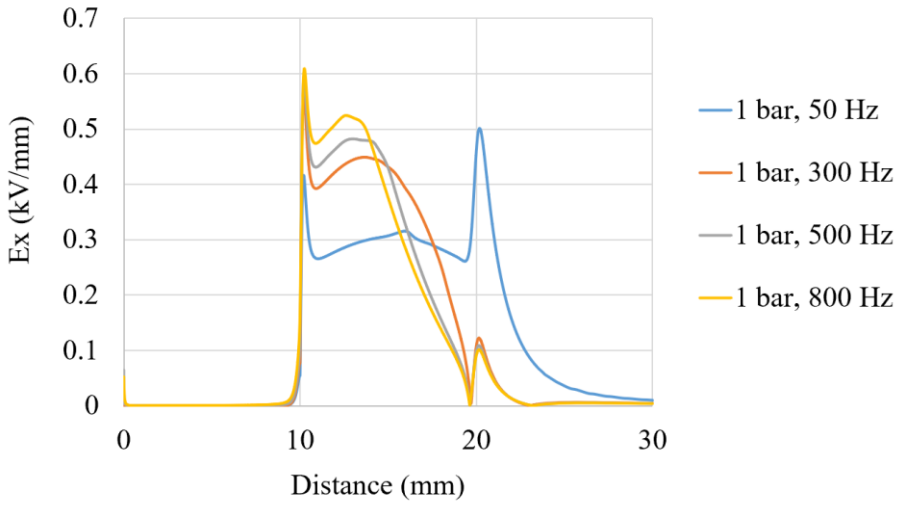

Figure 6.19 Electric field distribution along the SGT surface under 1 bar.

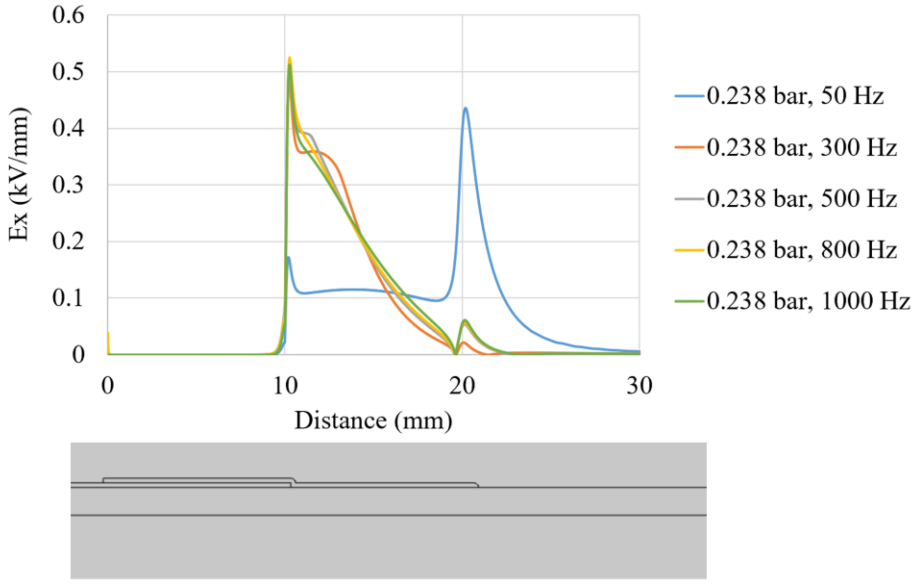

Figure 6.20 Electric field distribution along the SGT surface under 0.238 bar.

Figure 6.21 summarises the maximum longitudinal electric field along the stress grading system under various frequencies and pressures. When the frequency is ranges from 50 Hz to 800 Hz, the inception electric field strength decreases around 15% when

the pressure is reduced from 1 bar to 0.23 bar. The reduced inception electric field under low pressure is an important criterion that needs to be considered when designing stress grading material.

The effect of frequency on inception electric field strength has a similar tendency under both 1 bar and 0.238 bar. When the frequency increases from 50 Hz to 500 Hz, the maximum longitudinal electric field increases from 0.52 kV/mm to 0.6 kV/mm and from 0.45 kV/mm to 0.51 kV/mm under 1 bar and 0.238 bar respectively. Above 500Hz, the inception electric field keeps constant and is less affected by increasing frequency from 500 Hz to 1000 Hz. There may be something physically happening with discharges that means a higher electric field strength is required at higher frequencies. Another possible reason is that there is a measurement variance in the PDIV at low frequencies.

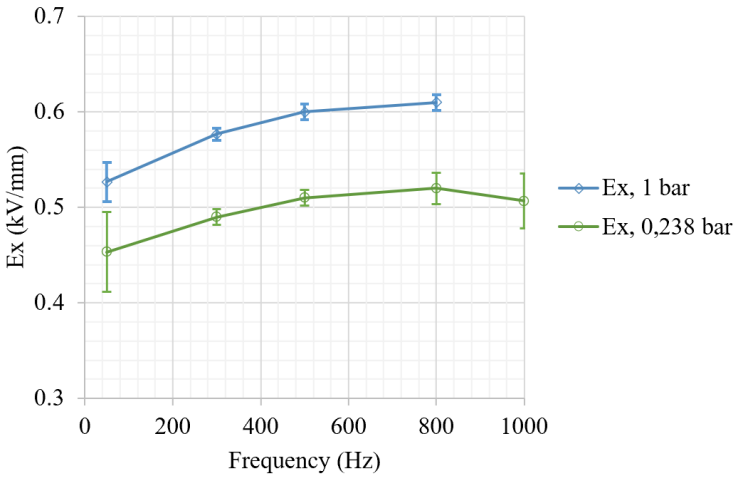

Figure 6.21 Maximum longitudinal electric field along the stress grading system.

6.3.4 Stress Grading System Characteristics

The experimental PDIV results and simulated longitudinal electric field under the PDIV have been discussed in Section 5.3.3. The results shows that stress grading tape can improve the PDIV of cable termination. Furthermore, the effect of pressure and frequency on both the PDIV and partial discharge inception electric field of cable termination with stress grading tape has been analysed. However, the effect of stress grading material properties on longitudinal electric field distribution has not been researched under an aerospace environment. Therefore, this section investigates the effect of stress grading material properties on the electric characteristics of stress

grading systems. The parameters, including initial conductivity, nonlinearity and permittivity, that may the electric field distribution will be analysed.

6.3.4.1 Effect of initial conductivity

Three types of initial conductivity of stress grading material were selected to investigate their effects on the electric field distribution as shown in Table 6.2.

Table 6.2 Initial conductivity

Initial conductivity	Value (S/m)
Low	$4*10^{-9}$
Measured	$4*10^{-8}$
High	$4*10^{-7}$

Figure 6.22 shows the electric field distribution on the stress grading surface when the applied voltage is 1350 V and frequency is 1000 Hz. The results indicate that the electric field along the stress grading system surface is reduced, while the electric field strength at the stress grading end is increased by increasing the initial conductivity. When conductivity increases, horizontal resistance decreases. Therefore, the voltage drop across the stress grading tape reduces, leading to decreasing electric field strength. However, when the initial conductivity is close to that of the conductor material, a strong electric field occurs at the end of the stress grading tape. There is an air gap between the stress grading end and insulation. When the resistance of the stress grading material is low, more voltage is distributed along this air gap, leading to a stronger electric field at the stress grading end.

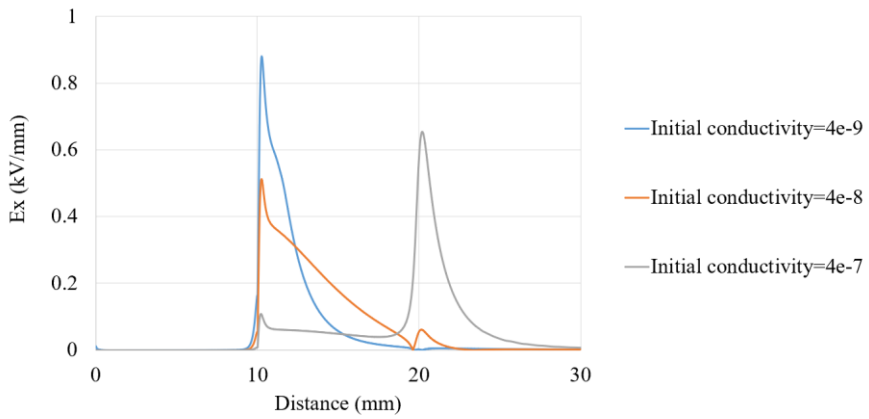

Figure 6.22 Electric field distribution along the stress grading system surface for various conductivity values under 1350 V and 1000 Hz.

6.3.4.2 Effect of nonlinearity

Three types of nonlinearity of stress grading material were selected to investigate their effect on electric field distribution. Figure 6.23 shows the effect of nonlinearity on electric field distribution. Results reveal that when nonlinearity increases, it has a similar phenomenon with increasing initial conductivity where the electric field along the stress grading system surface is reduced, while the electric field strength at the stress grading end is increased. The reason is that the conductivity is increased by either increasing initial conductivity or nonlinearity. It is not good to have a peak electric field at either the ground end or the stress grading end. In an optimal stress grading system, the electric field of the two ends is the same and a flat line of electric field is between the two ends.

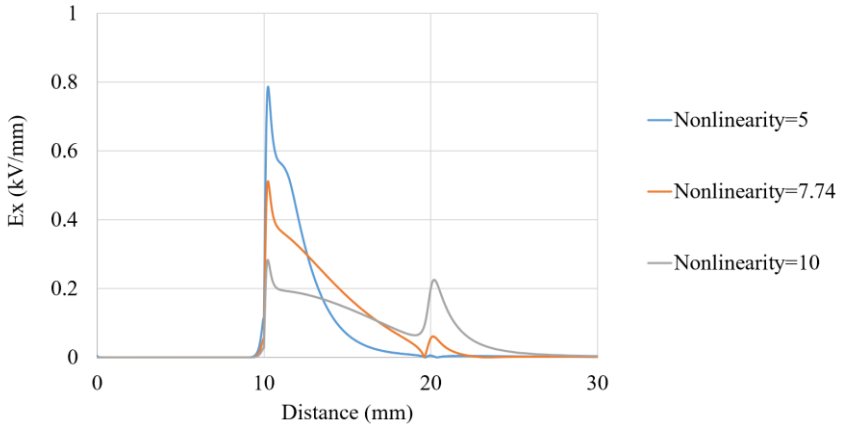

Figure 6.23 Electric field distribution along the stress grading system surface for various nonlinearity values under 1350 V and 1000 Hz.

6.3.4.3 Effect of relative permittivity

Figure 6.24 shows the effect of relative permittivity of stress grading material on electric field distribution. The results indicate that the maximum electric field only decreases by approximately 3% when permittivity increases from 2 to 10. Therefore, in a nonlinear stress grading system, the effect of the relative permittivity of stress grading material on electric field distribution is negligible, presumably as the low resistivity at high fields provides the dominant effect.

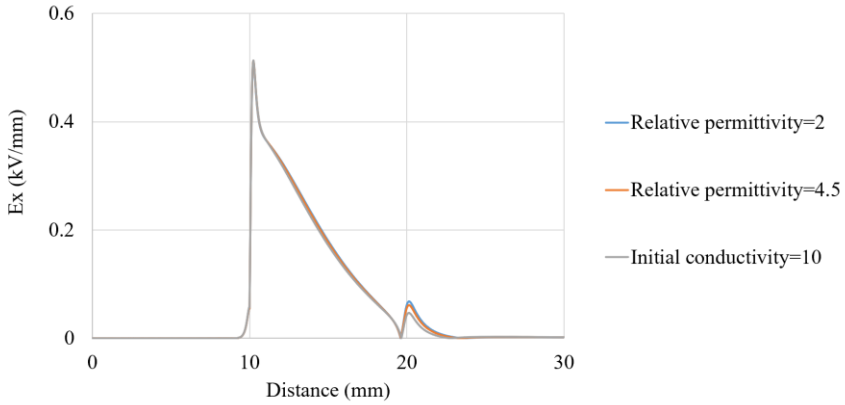

Figure 6.24 Electric field distribution along the stress grading system surface for various stress grading material permittivity under 1300 V and 1000 Hz.

6.4 Summary

This chapter tested the partial discharge inception voltage of screened cable terminations with and without a stress grading system under various frequencies and pressure to investigate the performance of stress grading material under aircraft operating conditions. A stress grading system model based on FEM was applied to simulate the longitudinal electric field strength of the stress grading system to determine the partial discharge inception electric field strength. The results are summarised below:

- The use of the selected stress grading materials on an example cable termination increases the PDIV up to 55% under atmospheric pressure and 30 % in an aerospace environment.
- For cable termination without a stress grading system, the PDIV was independent of frequencies. For cable termination with a stress grading system, the PDIV decreases with increasing frequencies. When the frequencies increased from 50 Hz to 500 Hz, the PDIV decreased by approximately 20% under atmospheric pressure and 10% in an aerospace environment.
- Partial discharge inception electric field was decreases at approximately 15% from 1 bar to 0.23 bar. It increases with increasing frequency and then saturates when the frequency is above 500 Hz.
- Increasing initial conductivity and nonlinearity of stress grading material may decrease the maximum electric field strength along the stress grading system surface but it may increase the electric field strength at the stress grading system end.

Chapter 7 Power Carrying Capacity Comparison

7.1 Introduction

With the increasing power level in future aircraft, the interconnection systems will need to withstand higher power levels while ensuring safe operation. The maximum power level of interconnection systems is determined by the safe operating voltage and current carrying capacity. In addition, the weight of interconnection systems is an important factor that needs to be considered for weight-constrained aircraft. While increasing conductor size and insulation thickness can improve the current carrying capacity and safe operating voltage, the weight of the interconnection systems is also increased. There is a trade-off between power carrying capacity and weight to achieve an optimal interconnection system design.

This chapter compares the power carrying capacity among unscreened cables, unscreened busbars and screened cables in an aerospace environment using the results that have been described in the previous chapters. The effect of interconnection systems, such as conductor size and insulation thickness, on their power carrying capacity will be analysed. Furthermore, their power/weight ratios will be compared to provide guidance for optimal interconnection system designs in future electric aircraft.

7.2 Methodology

7.2.1 Interconnection Systems Properties and Operating Conditions

Three types of interconnection systems (unscreened aircraft cables, unscreened busbars and screened cables) will be investigated and compared. The geometry and dimensions of these interconnection systems are shown in Figure 7.1 – Figure 7.3. For unscreened cables and screened cables, four conductor sizes (AWG 12, AWG 4, AWG 0 and AWG 4/0) are used, covering the size range of existing aircraft cables. Four equivalent conductor cross-section areas are selected for unscreened busbars, which are similar to these of cables. Typical aspect ratios (5 and 8) are used to investigate the effect of aspect ratio on the power carrying capacity, with the fillet radius of busbars set as 0.1 mm. The insulation thickness in current aircraft is between 1 mm and 2 mm. In future aircraft, thicker insulation will be required to withstand higher voltage levels. The chosen insulation thickness is between 1 mm and 10 mm to help discuss the effect of insulation thickness on power carrying capacity.

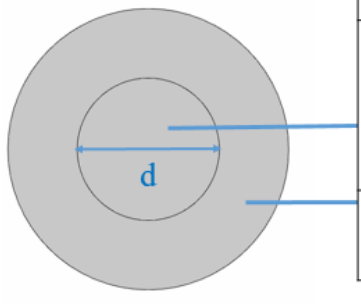

Unscreened cable	
Conductor diameter (Aluminium)	AWG12 (d=2.05 mm) AWG 4 (d=5.19 mm) AWG 0 (d=8.25 mm) AWG 4/0 (d=11.68 mm)
Insulation thickness (PTFE)	1 mm – 10 mm

Figure 7.1 Geometry of unscreened cables.

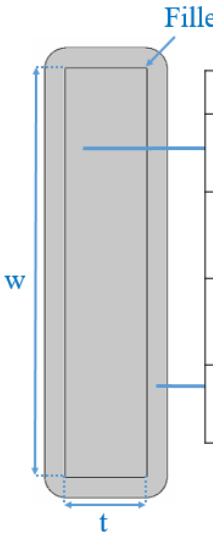

Unscreened busbar					
Equivalent conductor cross-section area		AWG 12	AWG 4	AWG 0	AWG 4/0
Aspect ratio w/t=5 (Aluminium)	w	4.06 mm	10.28 mm	16.35 mm	23.14 mm
	t	0.81 mm	2.06 mm	3.27 mm	4.63 mm
Aspect ratio w/t=8 (Aluminium)	w	5.14 mm	13.01 mm	20.68 mm	29.28 mm
	t	0.64 mm	1.63 mm	2.58 mm	3.66 mm
Insulation thickness (PTFE)	1 mm – 10 mm				

Figure 7.2 Geometry of unscreened busbars.

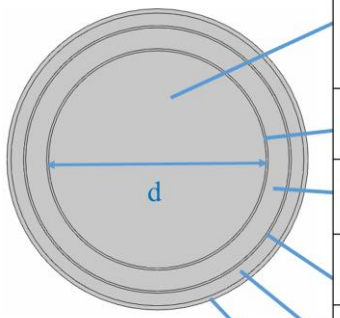

Screened cable	
Conductor diameter (Aluminium)	AWG 12 (d=2.05 mm) AWG 4 (d=5.19 mm) AWG 0 (d=8.25 mm) AWG 4/0 (d=11.68 mm)
Semiconductor screen thickness	0.1 mm
Insulation thickness (PTFE)	1 mm – 10 mm
Semiconductor screen thickness	0.1 mm
Metal screen (Aluminium)	0.6 mm
Protective sheath (PTFE)	0.2 mm

Figure 7.3 Geometry of screened cables.

The chosen conductor material is aluminium. The key advantage of aluminium over copper is that it has a lower current/weight ratio (as discussed in Chapter 4). As there is no effect of the conductor material on the safe operating voltage, an aluminium interconnection system has a lower power/weight ratio than a copper interconnection system when the conductor cross-section area is the same. The insulation material is PTFE, which is commonly applied in existing aircraft cables. The material properties of the interconnection system applied in both thermal and electrical models to calculate the current carrying capacity and safe operating voltage respectively have been described in Chapter 4, Chapter 5 and Chapter 6. The material properties of stress grading material were obtained from the CIGRE brochure on field grading in electrical insulation systems. Its initial conductivity is 2.5×10^{-6} S/m and its nonlinearity is 1.7 [126].

The geometry and material properties have been described in the previous section. Concerning operating conditions, the pressure is set as 0.238 bar, which is the pressure at common cruise altitude of most commercial aircraft (35,000 feet). The operating frequency is set as 1000 Hz. The ambient temperature for the current carrying capacity determination is 40 ^{o}C to simulate the worst conditions in an aircraft cabinet.

It is assumed for screened cable, the sheath is only grounded at one end, so there is no current circulating through the sheath. The effect of temperature on the PDIV is theoretically managed by a change in the equivalent pressure. When the temperature changes from 25 ^{o}C to 40 ^{o}C, the equivalent pressure decreases from 0.238 bar to 0.227 bar, leading to a change in the PDIV. Therefore, the effect of 15 ^{o}C difference on the PDIV calculation is negligible and is ignored in this analysis.

7.2.2 Optimal Design Process

Figure 7.4 shows the procedure of optimal design process by comparing the power/weight ratio of interconnection systems. An optimal interconnection system is one that can deliver the required power capacity and has the maximum power/weight ratio. In Chapter 3 and Chapter 4, a thermal model to simulate the current carrying capacity of interconnection systems under aerospace environments has been developed and validated. In Chapter 5, the streamer criterion method has been applied to calculate PDIV of unscreened cables and busbars. In Chapter 6, the longitudinal partial discharge inception electric field under low pressures and high frequencies has been obtained by

the electric field simulation model, which can be used as the criterion to determine the PDIV of screened cable terminations. By combing all work in Chapter 3 – Chapter 6 together, the current carrying capacity and safe operating voltage of three types of interconnection systems (unscreened cables, unscreened busbars and screened cables) can be simulated under various designs including geometry and insulation thickness. Therefore, the power/ratio of these interconnection systems can be compared to obtain the optimal design.

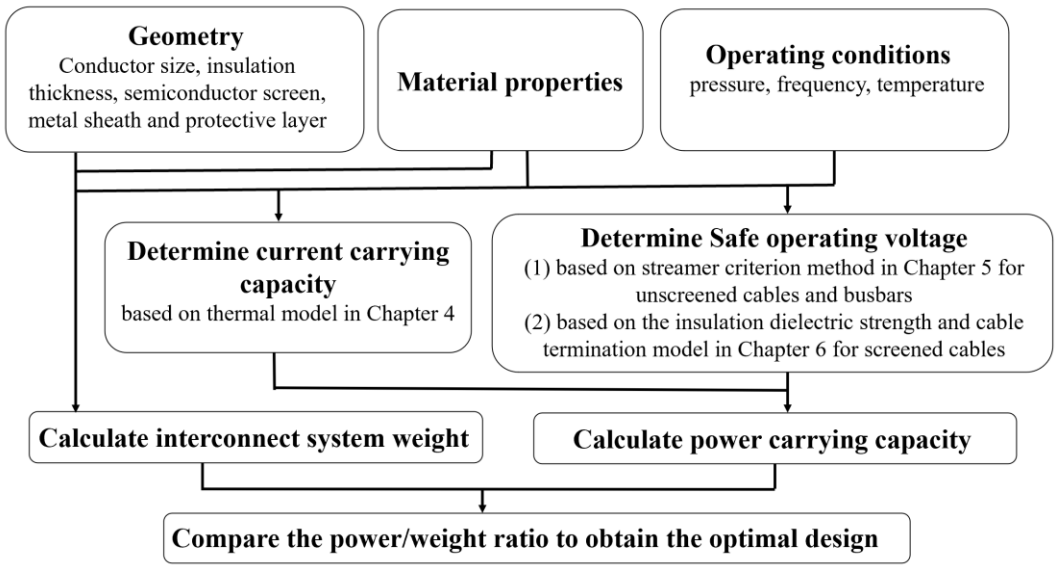

Figure 7.4 Optimal design procedure.

The details of the procedures for the determination of current carrying capacity, safe operating voltage and power to weight ratio are described as follows:

- The thermal model described in Chapter 4 is used to determine the maximum current carrying capacity. It needs to be noted that the current carrying capacity is determined based on a single cable or busbar in free air. Thermal interaction, such as conduction and radiation, and the proximity effect caused by adjacent interconnection systems, are not considered. The maximum conductor temperature is set as 200 ^{o}C, which is determined by the maximum operating temperature of PTFE.
- The safe operating voltage of unscreened cables and busbars is determined by the minimum PDIV of phase-phase geometry based on the streamer criterion method described in Chapter 5. The safe operating voltage of the screened cable is determined by both insulation dielectric strength and the longitudinal electric field

strength along the cable termination described in Chapter 6. The inception electric field strength of cable termination with a stress grading system is set as 0.5 kV/mm.

- For a screened cable without considering termination, the safe operating voltage depends on the dielectric strength of insulation material if the cable system is assumed to be free of gas-filled voids and the electric field between the conductor and ground is uniform. The maximum electric field strength should be lower than the dielectric strength of PTFE. The dielectric strength of PEFE is obtained from [127]. The safe operation voltage can be calculated by:

$$V_b = E_{max} \times R_a \, ln\left(\frac{R_a + R_b}{R_a}\right) \tag{7.1}$$

where R_a is the conductor radius (m), R_b is the insulation thickness (m), V_b is the applied voltage on the cable (V) and E_{max} is the maximum electric field strength in the insulation material that is equal to the dielectric strength of the insulation material (V/m).

- The single-phase power rating is calculated by multiplying the RMS value of the maximum current carrying capacity and single-phase safe operating voltage. The load factor is assumed as 1. The weight of the interconnection system is calculated based on one meter length. In a real three-system, the maximum current capacity may reduce due to the proximity of the adjacent interconnect systems.

7.3 Results

7.3.1 Effect of Conductor Cross-section Area

Figure 7.5 shows the maximum current carrying capacity as a function of the conductor cross-sectional area for different types of interconnection systems with an insulation thickness of 1 mm. The current carrying capacity of all interconnection systems increases with the conductor cross-sectional area because the conductor area results in a lower resistivity and better thermal dissipation due to a larger surface area. When the conductor cross-sectional area increases from 3.3 mm^2 to 107.2 mm^2, the current carrying capacity of an unscreened cable increases from 53 A to 480 A, which is the lowest among the four interconnection systems. Compared to an unscreened cable, the current carrying capacity of a screened cable is 11% higher with a 3.3 mm^2 conductor area and 3% higher with a 107.2 mm^2 conductor area. The current carrying capacity of

an unscreened busbar with an aspect ratio of 5 is between 9% and 17% higher than an unscreened cable. The current carrying capacity increases with an increasing aspect ratio for unscreened busbars. When the aspect ratio is 8, its current carrying capacity is between 17% and 27% higher than unscreened cables.

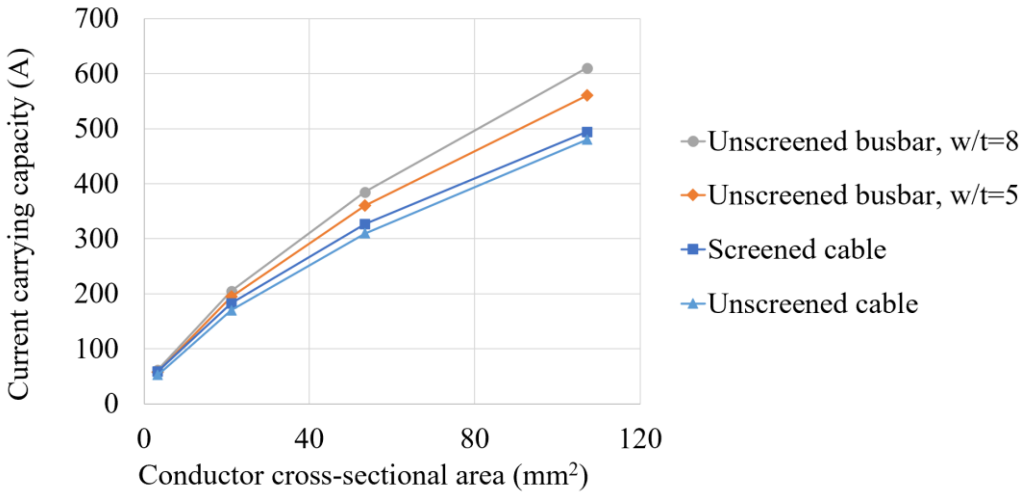

Figure 7.5 Current carrying capacity versus conductor cross-sectional area.

Figure 7.6 compares the safe operating voltages between various interconnection systems with an insulation thickness of 1 mm. The safe operating voltage is unaffected by the conductor cross-sectional area for screened cables and unscreened busbars. For unscreened cables, the safe operating voltage is reduced by 100 V when the conductor size is increased from AWG 12 to AWG 4/0. The screened cable has the largest safe operating voltage and the unscreened busbar the lowest safe operating voltage.

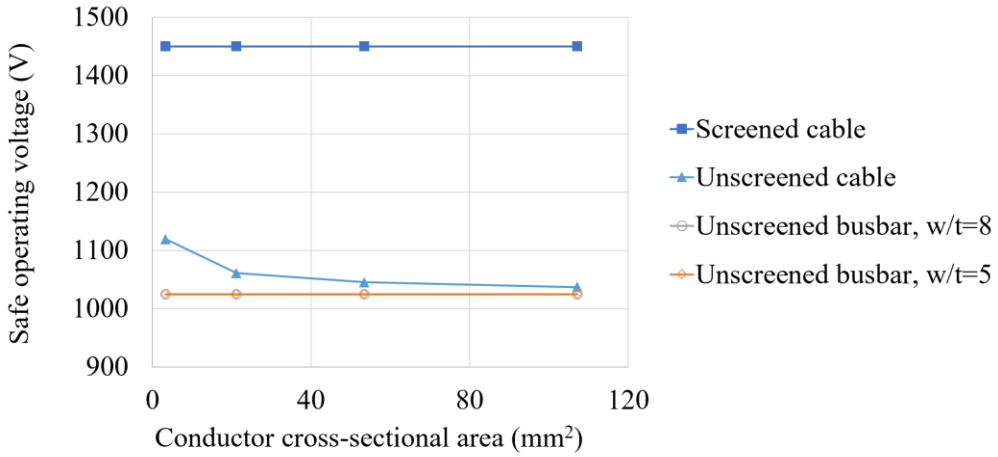

Figure 7.6 Safe operating voltage versus conductor cross-sectional area.

Figure 7.7 shows the relationship between power rating and conductor cross-sectional area with an insulation thickness of 1 mm. The power rating increases with conductor cross-sections area for all interconnection systems. When the conductor size is in the range between AWG 4 and AWG 4/0, screened cable has the maximum power rating and the unscreened cable has the minimum power rating. The busbar power rating increases with the increasing aspect ratio because increasing the aspect ratio increases the current carrying capacity but does not affect the safe operating voltage.

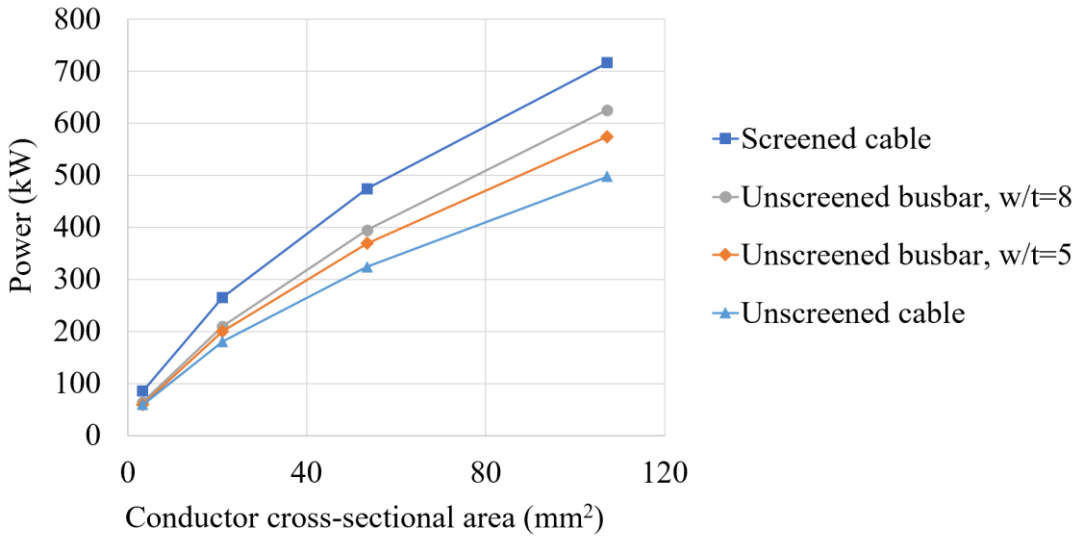

Figure 7.7 Maximum power carrying capacity versus conductor cross-sectional area.

Figure 7.8 compares the interconnection system weight versus conductor cross-section area for different interconnection systems. Screened cables are the heaviest due to their complex structure that includes screen layers and a protective sheath. Unscreened busbars are heavier than screened cables due to their larger insulation area. When the conductor size increases from AWG 12 to AWG 4/0, the insulation weight of an unscreened busbar is between 33% and 47% higher than that of an unscreened cable when the aspect ratio is 5 and between 52% and 73% higher when the aspect ratio is 8.

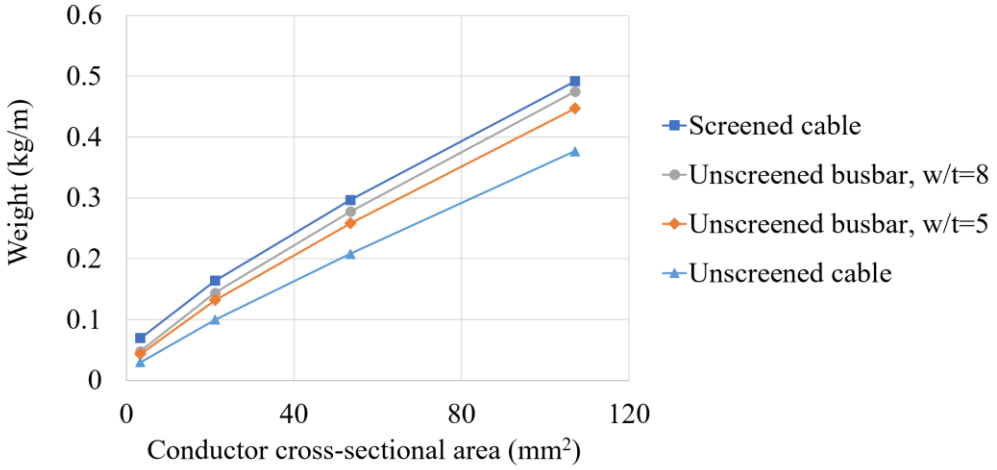

Figure 7.8 Weight versus conductor cross-sectional area.

Figure 7.9 compares the power/weight ratio versus conductor cross-sectional area for different interconnection systems. When the conductor cross-sectional area increases from AWG 12 to AWG 4/0, the power/weight ratio of the unscreened cable decreases from 1978 kW/kg · m to 1321 kW/kg · m. The unscreened cable has the largest power/weight ratio among all interconnection systems when the conductor size is AWG 12 and AWG 4/0. For an screened cable, its power/weight ratio increases from 1231 kW/kg · m to 1618 kW/kg · mm, before decreasing to 1456 kW/kg · m. The screened cable has the largest power/weight ratio among all interconnection systems when the conductor size is AWG 0 and AWG 4/0. For unscreened busbars with an aspect ratio of 5, its power/weigh ratio increases from 1375 kW/kg · m to 1517 kW/kg · m, before decreasing to 1283 kW/kg · m. Unscreened busbars with different aspect ratios have an approximately equal power/weight ratio. The increasing aspect ratio not only increases the power rating but also increases the weight of busbars due to the increasing insulation area. The difference between the busbars with aspect ratios of 5 and 8 is within 4%.

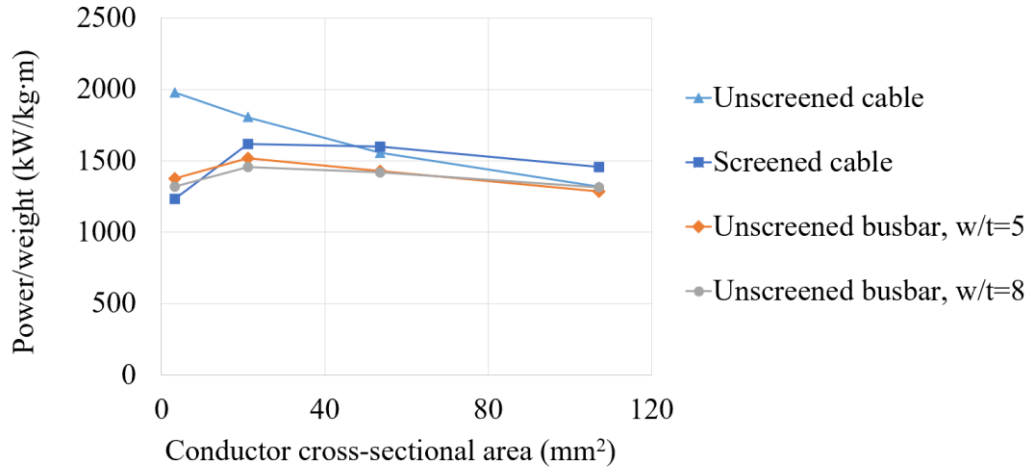

Figure 7.9 Power/weight ratio versus conductor cross-sectional area.

The safe operating voltage of screened cable is determined by both dielectric strength of insulation material and the minimum PDIV of the cable termination. If the electrical discharge occurring at the cable termination of screened cable is not considered, the safe operating voltage, power rating and power/weight ratio of screened cable compared with other interconnection system designs are shown in Figure 7.10, Figure 7.11 and Figure 7.12 respectively. The safe operating voltage of screened cable is above 20 kV when only considering the dielectric strength of the insulation material. Its power rating is above 10 times higher than that of other interconnection systems as it has a high magnitude of safe operating voltage. Even though the screened cable has the maximum weight, its power/weight ratio is still much higher that other interconnection system designs. This shows the importance of the management of electric field at the end of the screened cable. With this management taking place it is clear that a screened cable would provide a more power dense solution for an aircraft operating at higher voltage.

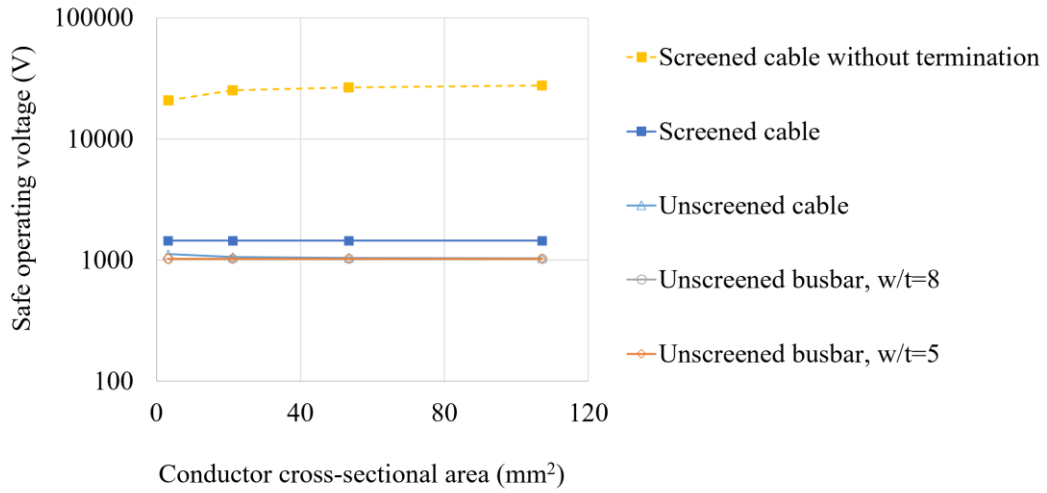

Figure 7.10 Safe operating voltage of the screened cable without considering the effect of termination.

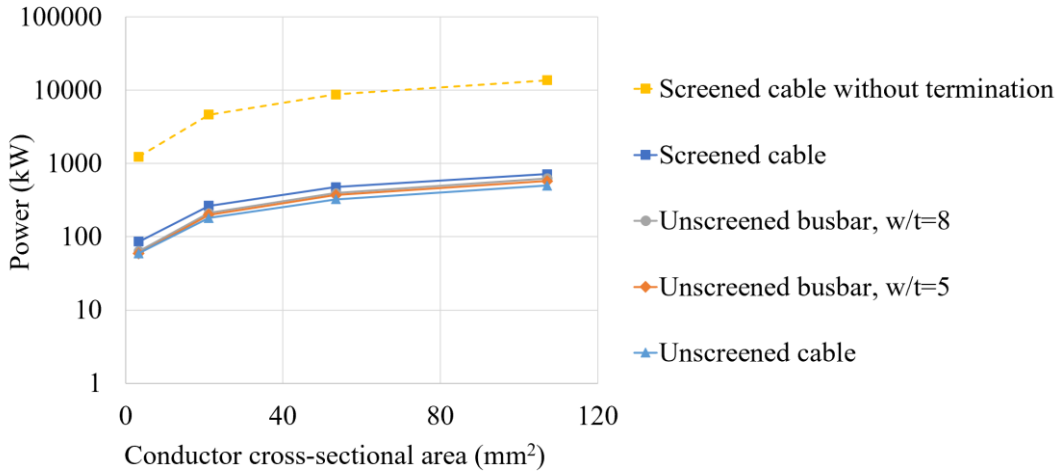

Figure 7.11 Maximum power carrying capacity versus conductor cross-sectional area of the screened cable without termination.

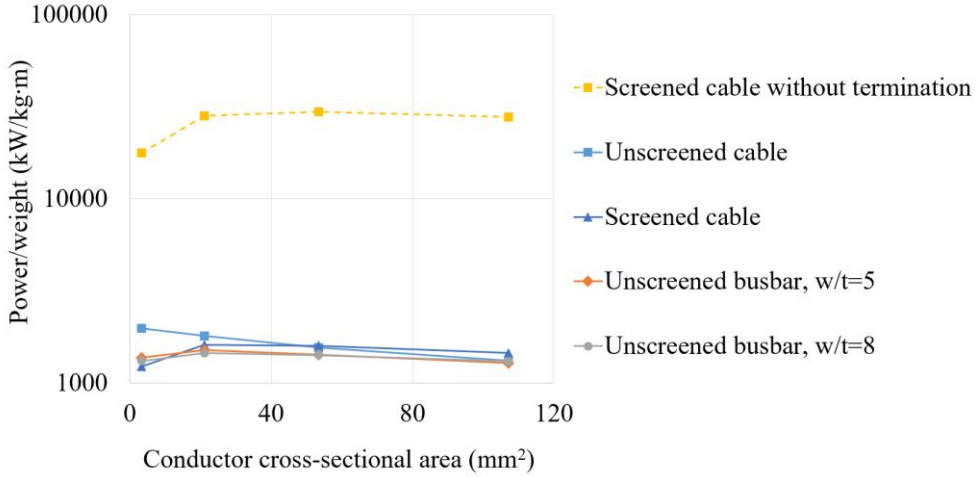

Figure 7.12 Power/weight ratio versus conductor cross-sectional area of the screened cable without termination.

7.3.2 Effect of Insulation Thickness

Figure 7.13 shows the maximum current carrying capacity as a function of insulation thickness for different types of interconnection system when the conductor size is AWG 4/0. The current carrying capacity decreases with increasing insulation thickness for all interconnection systems because increasing insulation thickness leads to a larger total thermal resistivity (as discussed in Chapter 4). Unscreened busbars have a larger rate of decrease than both unscreened and screened cables. The unscreened cable has the lowest current carrying capacity among the four interconnection systems and the unscreened busbar with an aspect ratio of 8 has the largest current carrying capacity. When the insulation thickness is increased from 1 mm to 10 mm, the difference between the unscreened cable and unscreened busbar with an aspect ratio of 8 decreases from 27% to 16%.

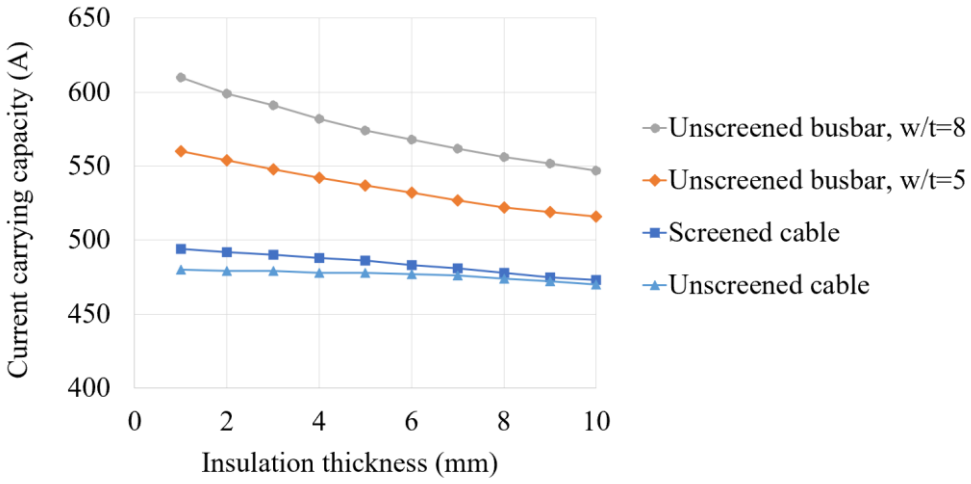

Figure 7.13 Maximum current carrying capacity versus insulation thickness.

Figure 7.14 compares safe operating voltages between various interconnection systems. It can be seen that the safe operating voltage increases with insulation thickness for all interconnection systems. When the insulation thickness is less than 3 mm, the screened cable has the largest safe operating voltage. When the insulation thickness increases, the unscreened cable has the largest safe operating voltage, which is slightly higher than that of unscreened busbars, which increases from 1% to 7% higher when the insulation thickness increases from 1 mm to 10 mm. The safe operating voltage of busbars is unaffected by the aspect ratio. This analysis again is based on the limitations imposed by the cable termination.

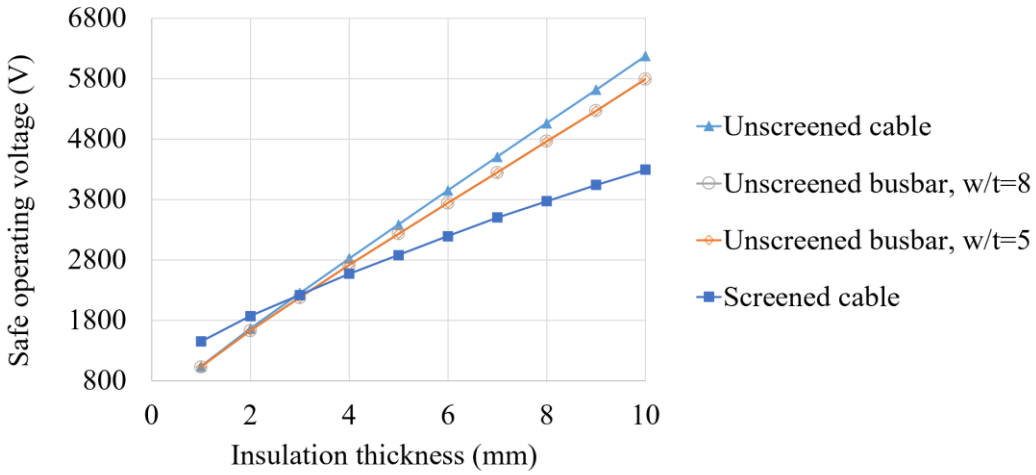

Figure 7.14 Safe operating voltage versus insulation thickness

Figure 7.15 shows the power carrying capacity as a function of insulation thickness. The power rating increases with insulation thickness for all interconnection systems. Even increasing insulation thickness leads to a decreasing current carrying capacity, with the increasing percentage of safe operating voltage higher than the decreasing percentage of the current carrying capacity. The screened cable has the maximum power rating when the insulation thickness is 1 mm. The unscreened busbar has the highest power carrying capacity when the insulation thickness is above 2 mm, with the power rating increasing with the aspect ratio.

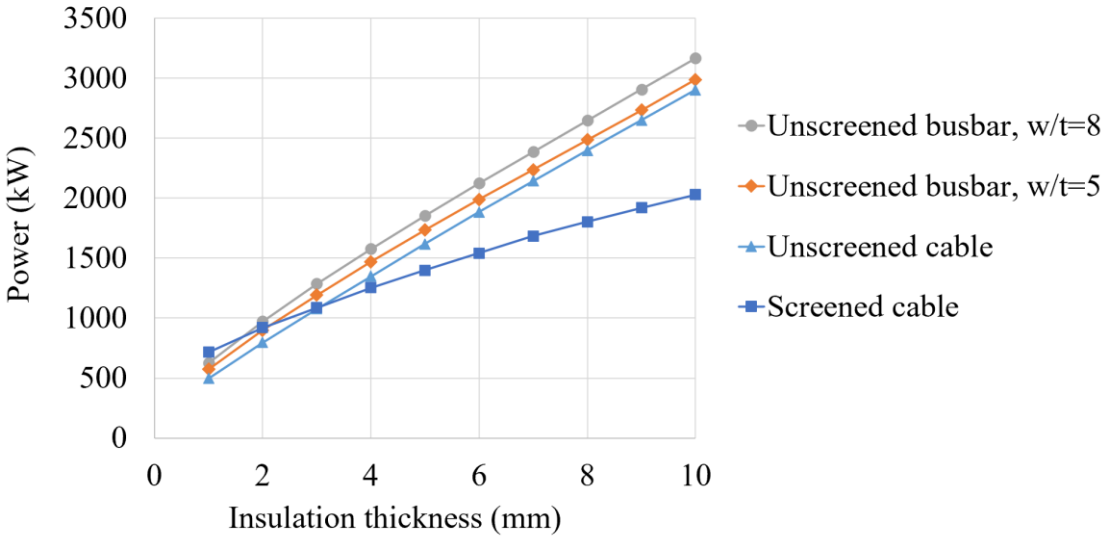

Figure 7.15 Maximum power carrying capacity versus insulation thickness

Figure 7.16 compares weight versus insulation thickness for the different systems. When the insulation thickness is 1 mm, the unscreened cable has the largest weight.

When the insulation thickness is increased, the unscreened busbar has the largest weight and the unscreened cable the lowest. The difference between the unscreened cable and screened cable remains constant, while the difference between them and unscreened busbar increases in tandem with the insulation thickness.

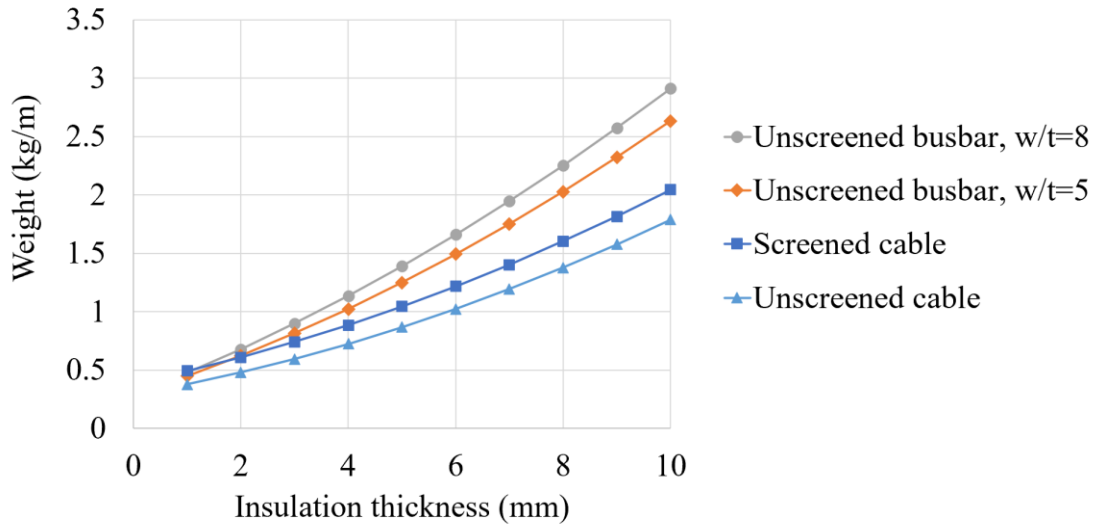

Figure 7.16 Weight versus insulation thickness.

Figure 7.17 compares the power/weight ratio versus insulation thickness for the different interconnection systems. When the insulation thickness increases, the power/weight ratio increases to a maximum value and then decreases. The optimal insulation thickness is approximately 5 mm for an unscreened cable under a safe operating voltage of around 3400 V. It has the largest power/weight ratio for the entire insulation thickness range, which is around 1870 kW/kg·m. The optimal weight/aspect ratio for both busbars is around 1450 kW/kg·m under a safe operating voltage of around 2200 V. The optimal weight/aspect ratio for screened cable is around 1500 kW/kg·m and its safe operating voltage is around 1900 V.

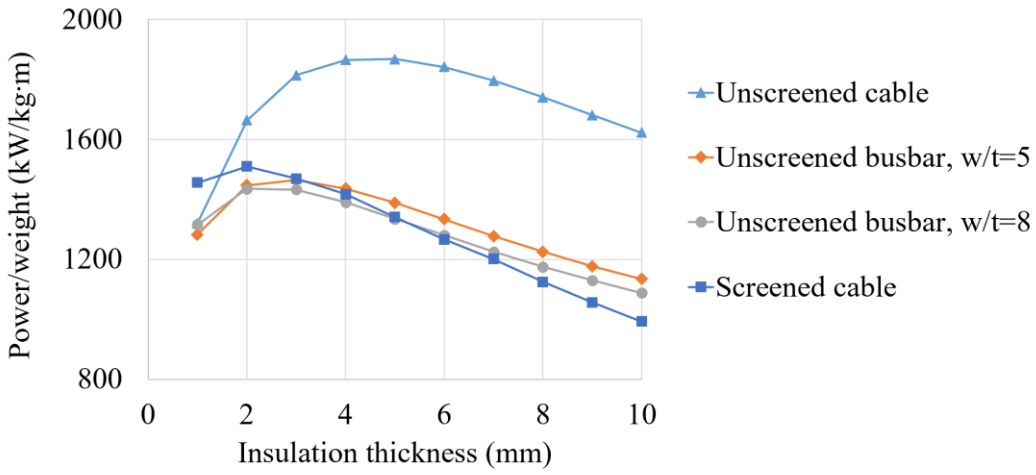

Figure 7.17 Power/weight ratio versus insulation thickness.

7.4 Summary

This chapter calculated the power carrying capacity based on the current carrying capacity and safe operating voltage for unscreened cables, unscreened busbars and screened cables. The power/weight aspect was also analysed using various conductors sizes and insulation thicknesses. The conclusions are summarised below for the cases where a screened cable is considered limited by the electric field at a termination:

- When the insulation thickness is 1 mm and conductor size increases from AWG 12 to AWG 4/0, screened cable has the highest the power carrying capacity and unscreened cable has the lowest power carrying capacity.
- When the insulation thickness is 1 mm and conductor size increases from AWG 12 to AWG 4/0, the power to weight ratio of unscreened cables continuously decreases, while the power to weight ratio of unscreened busbars and screened cables increases initially before decreasing. The unscreened cable has the largest power/weigh ratio among all interconnection systems when the conductor size is AWG 12 and AWG 4. The screened cable has the largest power/weigh ratio among all interconnection systems when the conductor size is AWG 0 and AWG 4/0.
- When the conductor size is AGW 4/0 and insulation thickness increases from 1 mm to 10 mm, screened cable has the maximum power rating when the insulation thickness is 1 mm. The unscreened busbar with an aspect ratio of 8

has the highest power carrying capacity when the insulation thickness is above 2 mm

- When the insulation thickness increases, the power/weight ratio increases to a maximum value and then decreases. The optimal insulation thickness is approximately 5 mm for an unscreened cable and 2 mm for both an unscreened busbar and screened cable. Screened cable has the largest power/weight ratio when the insulation thickness is 1 mm. When the insulation thickness is above 2 mm, an unscreened cable has the largest power/weight ratio
- Screened cables have the potential to increase their power rating and power/weight ratio significantly if the safe operation voltage of cable termination can be increased.

Chapter 8 Conclusion and Future Research

8.1 Conclusions

The increasing power level in future aircraft brings challenges to interconnection systems that will be required in terms of how they will handle accompanying thermal and electrical stresses. To improve reliability and reduce the weight of interconnection systems, this PhD project has investigated the current carrying capacity and safe operation voltage of conventional aircraft cables, screened cables and unscreened busbars under future aircraft operating conditions. Furthermore, the power carrying capacity of different interconnection systems have been analysed and compared. The conclusions of this research are presented below.

Current Carrying Capacity Design

In order to validate the thermal model under future aircraft operating conditions, a high-current (up to 500 A) and high-frequency (up to 2000 Hz) thermal test setup was developed to simulate the thermal performance of both cables and busbars under practical currents conditions in future electric aircraft. The maximum difference between simulation and test results was 4 °C for rods and 9 °C for busbars. The thermal model based on FEM was used to analyse the effect of parameters, including conductor geometry, material, insulation thickness, frequency and pressure, on current carrying capacity. This model considered the effect of frequency on conductor resistance, which was ignored in existing standard. Moreover, it can be applied to simulate thermal dissipation performance with complex geometries such as busbars under low pressures. The results showed that for an AWG 4/0 cable, copper conductors had an approximately 20% higher current carrying capacity than aluminium conductors under 1000 Hz. In addition, when the frequency increased from 500 Hz to 2000 Hz, the current carrying capacity decreased by around 15% for an AWG 4/0 cable. When the frequency increased from 1 mm to 5 mm, the current carrying capacity only changed by approximately 3%. Compared with insulation thickness, frequency is more important for current carrying capacity design in future aircraft. By comparing cables and busbars, the current carrying capacity of a busbar with an aspect ratio of 5 was 15% higher at 500 Hz and 19% higher at 2000 Hz than both cables. It also showed that the current carrying capacity increased with an increasing aspect ratio. When the aspect ratio was 8, the current carrying capacity of busbars was 24% higher at 500 Hz and 30% higher

at 2000 Hz than the cables. For an AWG 4/0 cable, the SAE AS50881 presented an approximately 5% conservative margin at 0.238 bar, with the conservative margin increasing with decreasing pressure.

Safe Operating Voltage Design

The streamer criterion method was applied to investigate the effect of conductor diameter, insulation thickness, relative permittivity and pressure on the safe operating voltage of both unscreened cables and unscreened busbars. The results indicated that for both cables and busbars, the safe operating voltage is determined by the minimum PDIV of the phase-phase geometry. When the gap distance between phases increased, the PDIV decreased first to a minimum value before increasing. It was found that conductor size only affected the safe operation voltage of cables and had no effect on busbars. When the conductor diameter decreased from AWG 4/0 to AWG 12, the minimum PDIV increased by approximately 6% with an insulation thickness of 1 mm under 0.238 bar of pressure. The PDIV difference between the AWG 4/0 cable and the busbar with an aspect ratio of 5 was within 5% under 0.238 bar, while the current carrying capacity of the busbar was between 15% and 19% higher than that of cables under a frequency range of 500 Hz and 2000 Hz. For both cables and busbars, increasing the relative permittivity of insulation resulted in a lower PDIV. However, due to the limited range of permittivity values, its sensitivity was not as large as the insulation thickness, especially under low pressures. The results suggest that insulation thickness is the most sensitive parameter for determining the PDIV. By comparing PDIV between unscreened cables and busbars, it was concluded that the use of busbars as opposed to round cables did not appear to have any significant risk in terms of voltage rating.

Stress Grading System Modelling

The PDIV of a cable termination with and without stress grading material was measured under various frequencies and pressures to investigate the performance of stress grading material in aerospace environments. It was found that tress grading material on cable termination increases the PDIV up to 55% under atmospheric pressure and 30 % in an aerospace environment. It was also found that for cable termination without a stress grading system, the PDIV was unaffected and independent of frequency. For cable termination with a stress grading system, the PDIV decreased with increasing

frequencies. When the frequency was increased from 50 Hz to 500 Hz, the PDIV decreased by approximately 20% under atmospheric pressure and 10% in an aerospace environment. A stress grading model was developed to simulate the longitudinal electric field strength along cable termination. The results showed that the partial discharge inception electric field was decreases by approximately 15% from 1 bar to 0.23 bar. It increased with increasing frequency and then saturated when the frequency is above 500 Hz. The effect of initial conductivity and nonlinearity of stress grading material on electric field strength was also investigated, finding that increasing initial conductivity and nonlinearity reduced the electric field strength of the stress grading system surface but increased the electric field strength of stress grading system end.

Power Carrying Capacity Comparison

Based on the thermal model for current carrying capacity, the streamer criterion method for PDIV of unscreened cables and busbars, and the stress grading system model for safe operating voltage of screened cables, an optimal design procedure was proposed by comparing the power carrying capacity and the power to weight ratio between unscreened cables, unscreened busbars and screened cables. It was found when the insulation thickness was 1 mm and conductor size increased from AWG 12 to AWG 4/0, the screened cable had the maximum the power carrying capacity and unscreened cable had the minimum power carrying capacity under the same conductor cross-section area. As the screened cable had the maximum weight and unscreened cable had the minimum weight under the same conductor cross-section area. The unscreened cable had the largest power/weigh ratio among all interconnection systems when the conductor size was AWG 12 and AWG 4. The screened cable had the largest power/weigh ratio among all interconnection systems when the conductor size was AWG 0 and AWG 4/0. When the conductor size was AWG 4/0 and insulation thickness increases from 1 mm to 10 mm, the power/weight ratio increased to a maximum value and then decreases. The optimal insulation thickness is approximately 5 mm for an unscreened cable and is around 2 mm for both an unscreened busbar and screened cable.

8.2 Future Research

This research has investigated both the thermal and electrical performance of interconnection systems in future aircraft. The following topics are still necessary for further investigation.

For current carrying capacity investigation

This study only considered the current carrying capacity of a single cable or busbar. In a three-phase interconnection system or a cable bundle, the proximity effect should be considered in current carrying capacity design.

This study investigated the thermal performance under a steady-state condition. In aircraft, the power level changes during flight, with insulation material able to withstand a temperature higher than the operational temperature for a short time. The transient thermal model can predict the temperature of interconnection systems and thus be used to design a more accurate current carrying capacity model.

For safe operating voltage calculation

Air is the only insulation gas considered in this study. It would be interesting to investigate the feasibility to use other gases, such as $SF_{6,}$ with higher dielectric strength as the insulation material because it may help increase the safe operating voltage.

For stress grading systems

This study only considered electric characteristics under room temperature. The effect of temperature may affect the stress grading material properties and change its electrical characteristics. Accordingly, it would be worth undertaking a comprehensive investigation of the performance of the stress grading system under different temperatures.

References

[1] IATA, “Aircraft Technology Roadmap to 2050,” 2019.
[2] IATA, "Annual Review 2019," 2019.
[3] IATA, "IATA 20-Year Air Passenger Forecast," 2017.
[4] B. Graver, K. Zhang, and D. Rutherford, "emissions from commercial aviation 2018," 2019.
[5] T. RÖTGER, “Aviation’s carbon footprint reduction through sustainable alternative fuels,” *ICAO Environmental Report 2016: On Board A Sustainable Future*, pp. 168–171, 2016.
[6] V. Madonna, P. Giangrande, and M. Galea, "Electrical power generation in aircraft: Review, challenges, and opportunities," *IEEE Transactions on Transportation Electrification*, vol. 4, no. 3, pp. 646-659, 2018.
[7] A. Barzkar and M. Ghassemi, "Electric power systems in more and all electric aircraft: A review," *IEEE Access*, vol. 8, pp. 169314-169332, 2020.
[8] X. Roboam, B. Sareni, and A. D. Andrade, "More electricity in the air: Toward optimized electrical networks embedded in more-electrical aircraft," *IEEE industrial electronics magazine*, vol. 6, no. 4, pp. 6-17, 2012.
[9] J. Rosero, J. Ortega, E. Aldabas, and L. Romeral, "Moving towards a more electric aircraft," *IEEE Aerospace and Electronic Systems Magazine*, vol. 22, no. 3, pp. 3-9, 2007.
[10] P. Wheeler and S. Bozhko, "The more electric aircraft: Technology and challenges," *IEEE Electrification Magazine*, vol. 2, no. 4, pp. 6-12, 2014.
[11] B. Sarlioglu and C. T. Morris, "More electric aircraft: Review, challenges, and opportunities for commercial transport aircraft," *IEEE transactions on Transportation Electrification*, vol. 1, no. 1, pp. 54-64, 2015.
[12] M. Sinnett, "787 no-bleed systems: saving fuel and enhancing operational efficiencies," *Aero Quarterly*, vol. 18, pp. 6-11, 2007.
[13] W. Cao, B. C. Mecrow, G. J. Atkinson, J. W. Bennett, and D. J. Atkinson, "Overview of electric motor technologies used for more electric aircraft (MEA)," *IEEE transactions on industrial electronics*, vol. 59, no. 9, pp. 3523-3531, 2011.
[14] Volocopter, "VOLOCITY design speficifations," 2019.
[15] Airbus, "CityAirbus NextGen." Accessed:April-2022. [Online]. Available: https://www.airbus.com/en/innovation/zero-emission/urban-air-mobility/cityairbus-nextgen
[16] Volocopter, "VOLOCITY." Accessed:April-2022. [Online]. Available: https://www.volocopter.com/solutions/volocity/
[17] Airbus, "Airbus, Rolls-Royce, and Siemens team up for electric future Partnership launches E-Fan X hybrid-electric flight demonstrator," 2017.
[18] W. Electric, " Home - Wright Electric," Accessed:April-2022. [Online]. Available: https://weflywright.com/
[19] IEA, "World Energy Outlook 2018," 2018.
[20] M. Borghei and M. Ghassemi, "Insulation Materials and Systems for More-and All-Electric Aircraft: A Review Identifying Challenges and Future Research Needs," *IEEE Transactions on Transportation Electrification*, vol. 7, no. 3, pp. 1930-1953, 2021.
[21] M. Bagshaw and P. Illig, "The aircraft cabin environment," *Travel medicine*, Elsevier, 2019.

[22] I. Christou, "*Optimisation of high voltage electrical systems for aerospace applications*," PhD Thesis, The University of Manchester, 2011.
[23] H. Xu, R. Lowndes, I. Cotton, "Power Capacity of High Voltage Cables for Future Electrical Aircraft", *Electrical Insulation Conference (EIC)*, 2021.
[24] Carlisle Interconnect Technologies, "Tufflite® Aluminum - TLA." Accessed:April-2022. [Online]. Available: https://www.carlisleit.com/prod-info/tufflite-aluminum-tla/
[25] Habia Cable, "Zeroarc® - for medium to high voltage cable solutions." Accessed:April-2022. [Online]. Available: https://www.habia.com/custom-cables-harnesses/medium-high-voltage-cable-solutions-zeroarc/
[26] V. Hinrichsen, D. Bachellerie, J. Das, L. Donzel, and M. Haddad, "Field grading in electrical insulation systems," *CIGRE WG D1. 56 Technical Brochure*, no. 794, 2020.
[27] Siemens. "Energy and data successfully put on track SIVACON 8PS busbar trunking systems." 2019.
[28] D. A. Burley, "Ship Installation Of Insulated Bus Pipe," in *NSRP Meeting Newport News*, Virginia, 2011.
[29] Nexans, "Aircraft Wires and Cables.", 2003.
[30] F. Bouvier, D. Dhenin, O. Pinto, "Innovative cables and cabling solutions for next-generation Aerospace - Aerospace White Paper," 2015.
[31] Nexans, "Innovative cables and cabling solutions for next-generation Aerospace Aerospace White Paper," 2015.
[32] *BS EN 3475-100:2010 Aerospace series — Cables, electrical, aircraft use — Test methods Part 100: General*, 2010.
[33] M. H. Tooley and D. Wyatt, *Aircraft electrical and electronic systems: principles, operation and maintenance*. Routledge, 2009.
[34] H. Schefer, L. Fauth, T. H. Kopp, R. Mallwitz, J. Friebe, and M. Kurrat, "Discussion on electric power supply systems for all electric aircraft," *IEEE Access*, vol. 8, pp. 84188-84216, 2020.
[35] F. Dricot and H. Reher, "Survey of arc tracking on aerospace cables and wires," *IEEE transactions on dielectrics and electrical insulation*, vol. 1, no. 5, pp. 896-903, 1994.
[36] AIR7502 Aircraft Electrical Voltage Level Definitions, SAE committee, 2021.
[37] A. Shekhar *et al.*, "Impact of dc voltage enhancement on partial discharges in medium voltage cables—An empirical study with defects at semicon-dielectric interface," *Energies*, vol. 10, no. 12, p. 1968, 2017.
[38] R. Lowndes and I. Cotton, "Forecasting the Partial Discharge Inception Voltage (PDIV) of Insulated Busbars for Future Aircraft Power Distribution Systems," *2021 IEEE Electrical Insulation Conference (EIC)*, pp. 189-192, 2021.
[39] K. Hollaus, S. Bauer, M. Leumüller, and C. Türk, "Measurement and modeling of effective cable parameters of unshielded conductors," *COMPEL-The international journal for computation and mathematics in electrical and electronic engineering*, 2022.
[40] M. Alsharif, P. Wallace, D. Hepburn, and C. Zhou, "FEM modelling of electric field and potential distributions of MV XLPE cables containing void defect," in *Excerpt from the Proceedings of the COMSOL Conference in Milan*, 2012.
[41] D. Chapman and T. Norris, *Copper for Busbars: Guidance for Design and Installation*. Copper Development Association, 2014.
[42] R. Worth, M. Islam, and C. Smith, "Insulated Bus Pipe (IBP) for power utility applications," *IEEE 11th International Conference on Transmission & Distribution Construction, Operation and Live-Line Maintenance*, 2006.

[43] A. A. Kostin and O. I. Taranenko, "ADVANTAGES OF BUSBAR SYSTEMS OVER CABLE SYSTEMS," in *Engineering and natural sciences*, pp. 36-38, 2020.
[44] SAE Standard AS50881, “Wiring aerospace vehicle,” USA: SAE International, 2010
[45] R. T. Coneybeer, W. Black, and R. Bush, "Steady-state and transient ampacity of bus bar," *IEEE Transactions on Power Delivery*, vol. 9, no. 4, pp. 1822-1829, 1994.
[46] R. V. Benthem, E. Bloem, F. Albero, and L. Azemard, "Flat cable derating tests and thermal modelling for weight reduction of aircraft engine harness designs," 2019.
[47] R. V. Benthem, W. D. Grave, F. Doctor, K. Nuyten, S. Taylor, and P. Jacques, "Thermal analysis of wiring for weight reduction and improved safety," in *National Aerospace Laboratory NLR. NLR-TP. AIAA/ICES Conference*, Portland, Oregan, USA, pp. 18-21, 2011.
[48] M. Schach, "Continuous current and temperature rise in aircraft cables," *Transactions of the American Institute of Electrical Engineers, Part II: Applications and Industry*, vol. 71, no. 4, pp. 197-203, 1952.
[49] S. Rickman and C. Iannello, "Heat transfer analysis in wire bundles for aerospace vehicles," *WIT Transactions on Engineering Sciences*, vol. 106, pp. 53-63, 2016.
[50] S. L. Rickman, "Re-Architecting the NASA Wire Derating Approach," in *Electrical Wiring Science and Technology Meeting*, 2021.
[51] S. Zhao, “Measurement and Prediction of temperature-rise in Switching Cabinet,” Master Thesis, Liverpool University, 2018.
[52] A. Plesca, "Thermal analysis of busbars from a high current power supply system," *Energies*, vol. 12, no. 12, p. 2288, 2019.
[53] T. J. Hughes, "Environmental controls on the state of HV cables under the seafloor," PhD Thesis, University of Southampton, 2016.
[54] D. W. Knight, “Components and material,” From Transmitter to Antenna, G3YNH,. 2014
[55] F. Loos, "Joule Heating in Connecting Structures of Automotive Electric Devices-Modelling, Simulation and Optimization," PhD Thesis, Universitätsbibliothek der Universität der Bundeswehr München, 2014.
[56] J. P. Holman, *Heat Transfer Tenth Edition*, McGraw-Hill Education, 2009
[57] G. Milano, "Some experimental results of free convection from horizontal heated wires below atmospheric pressure," in *International Heat Transfer Conference*, vol. 49422, pp. 183-192, 2010.
[58] M. Fujii, T. Fujii, and T. Honda, "Theoretical and experimental studies of the free convection around a long horizontal thin wire in air," in *International Heat Transfer Conference Digital Library*, 1982.
[59] D. Collis and M. Williams, "Two-dimensional convection from heated wires at low Reynolds numbers," *Journal of Fluid Mechanics*, vol. 6, no. 3, pp. 357-384, 1959.
[60] V. T. Morgan, "The overall convective heat transfer from smooth circular cylinders," in *Advances in heat transfer*, vol. 11, pp. 199-264, 1975.
[61] J. Kyte, A. Madden, and E. L. Piret, "Natural-convection heat transfer at reduced pressure-spheres and cylinders," *Chemical Engineering Progress*, vol. 49, no. 12, pp. 653-662, 1953.
[62] R. Van Benthem, W. d. Grave, F. Doctor, K. Nuyten, S. Taylor, and P. Jacques, "Thermal analysis of wiring for weight reduction and improved safety," 2011.
[63] F. P. Incropera, D. P. DeWitt, T. L. Bergman, and A. S. Lavine, *Fundamentals of heat and mass transfer*. Wiley New York, 1996.
[64] R. W. Lewis, P. Nithiarasu, and K. N. Seetharamu, *Fundamentals of the finite element method for heat and fluid flow*. John Wiley & Sons, 2004.

[65] A. Sedaghat and F. De Leon, "Thermal analysis of power cables in free air: Evaluation and improvement of the IEC standard ampacity calculations," *IEEE Transactions on power delivery*, vol. 29, no. 5, pp. 2306-2314, 2014.
[66] L. Xiong, Y. Chen, Y. Jiao, J. Wang, and X. Hu, "Study on the effect of cable group laying mode on temperature field distribution and cable ampacity," *Energies*, vol. 12, no. 17, p. 3397, 2019.
[67] S. Kim *et al.*, "Coupled finite-element-analytic technique for prediction of temperature rise in power apparatus," *IEEE Transactions on Magnetics*, vol. 38, no. 2, pp. 921-924, 2002.
[68] J. K. Kim, S. C. Hahn, K. Y. Park, H. K. Kim, and Y. H. Oh, "Temperature rise prediction of EHV GIS bus bar by coupled magnetothermal finite element method," *IEEE Transactions on Magnetics*, vol. 41, no. 5, pp. 1636-1639, 2005.
[69] J. H. Yoon, H. S. Ahn, J. Choi, and I.-S. Oh, "An estimation technology of temperature rise in GIS bus bar using three-dimensional coupled-field multiphysics," in *Conference Record of the 2008 IEEE International Symposium on Electrical Insulation*, 2008: IEEE, pp. 432-436.
[70] H. Jahangiri-Haghighi, "Ageing and Failure Mechanisms of Electrical Materials for High Voltage Systems in Aerospace Applications," PhD Thesis, The University of Manchester, 2020.
[71] I. Cotton, A. Nelms, and M. Husband, "Higher voltage aircraft power systems," *IEEE Aerospace and Electronic Systems Magazine*, vol. 23, no. 2, pp. 25-32, 2008.
[72] F. Alrumayan, I. Cotton, and A. Nelms, "Partial discharge testing of aerospace electrical systems," *IEEE Transactions on Aerospace and Electronic Systems*, vol. 46, no. 2, pp. 848-863, 2010.
[73] A. Woodworth, E. E. Shin and M. Lizcano, "High voltage insulation for electrified aircraft", *Proc. EnergyTech IX Center*, pp. 1-2, 2018.
[74] M. Abdel-Salam, *High-voltage engineering: theory and practice, revised and expanded*. CRC Press, 2018.
[75] M. Halleck, "Calculation of corona-starting voltage in air-solid dielectric systems," *Transactions of the American Institute of Electrical Engineers. Part III: Power Apparatus and Systems*, vol. 75, no. 3, pp. 211-216, 1956.
[76] I. Christou, A. Nelms, I. Cotton, and M. Husband, "Choice of optimal voltage for more electric aircraft wiring systems," *IET Electrical Systems in Transportation*, vol. 1, no. 1, pp. 24-30, 2011.
[77] R. Rui and I. Cotton, "Impact of low pressure aerospace environment on machine winding insulation," in *2010 IEEE International Symposium on Electrical Insulation*, 2010: IEEE, pp. 1-5.
[78] L. Lusuardi, A. Cavallini, M. G. de la Calle, J. Martínez-Tarifa, and G. Robles, "Insulation design of low voltage electrical motors fed by PWM inverters," *IEEE Electrical Insulation Magazine*, vol. 35, no. 3, pp. 7-15, 2019.
[79] P. Collin, "Design, taking into account the partial discharges phenomena, of the electrical insulation system (EIS) of high power electrical motors for hybrid electric propulsion of future regional aircrafts," Université Paul Sabatier-Toulouse III, 2020.
[80] G. Baş, "Electric field anaysis in stress controlled high voltage cables," Master Thesis, Middle East Technical University, 2005.
[81] J. C. Wheeler, "Effects of converter pulses on the electrical insulation in low and medium voltage motors," *IEEE Electrical Insulation Magazine*, vol. 21, no. 2, pp. 22-29, 2005.

[82] R. Schmerling, F. Jenau, S. Kempen, and F. Pohlmann, "Parameter studies on surface partial discharge inception of polluted, tangential electrically stressed boundary surfaces," *Electrical Insulation Conference (EIC)*, pp. 115-119, 2011.
[83] A. Eigner and S. Semino, "50 years of electrical-stress control in cable accessories," *IEEE Electrical Insulation Magazine*, vol. 29, no. 5, pp. 47-55, 2013.
[84] R. Strobl, W. Haverkamp, G. Malin, and F. Fitzgerald, "Evolution of stress control systems in medium voltage cable accessories," *IEEE/PES Transmission and Distribution Conference and Exposition. Developing New Perspectives* vol. 2: IEEE, pp. 843-848, 2001.
[85] M. Secklehner, R. Hussain, and V. Hinrichsen, "Tailoring of new field grading materials for HVDC systems," *13th International Electrical Insulation Conference (INSUCON)*, pp. 1-6, 2017.
[86] E. Martensson, B. Nettelbled, U. Gafvert, and L. Palmqvist, "Electrical properties of field grading materials with silicon carbide and carbon black," *Proceedings of the 6th International Conference on Conduction and Breakdown in Solid Dielectrics*, pp. 548-552, 1998.
[87] C. Onneby, E. Martensson, U. Gafvert, A. Gustafsson, and L. Palmqvist, "Electrical properties of field grading materials influenced by the silicon carbide grain size," *Proceedings of the IEEE 7th International Conference on Solid Dielectrics*, pp. 43-45, 2001.
[88] X. Yang, J. He, and J. Hu, "Tailoring the nonlinear conducting behavior of silicone composites by ZnO microvaristor fillers," *Journal of Applied Polymer Science*, vol. 132, no. 40, 2015.
[89] L. Donzel, F. Greuter, and T. Christen, "Nonlinear resistive electric field grading Part 2: Materials and applications," *IEEE Electrical Insulation Magazine*, vol. 27, no. 2, pp. 18-29, 2011.
[90] K. Kimura and S. Hirabayashi, "Improved potential grading methods with silicon carbide paints for high voltage coils," *IEEE Transactions on Electrical Insulation*, no. 3, pp. 511-517, 1985.
[91] V. Kogan, F. Dawson, G. Gao, and B. Nindra, "Surface corona suppression in high voltage stator winding end turns," *Electrical Electronics Insulation Conference and Electrical Manufacturing & Coil Winding Conference*, pp. 411-415, 1995.
[92] C. Staubach, T. Hildinger, and A. Staubach, "Comprehensive electrical and thermal analysis of the stress grading system of a large hydro generator," *IEEE Electrical Insulation Magazine*, vol. 34, no. 1, pp. 37-49, 2018.
[93] C. Stauback and T. Hildinger, "Advanced Techniques for Electrical and Thermal Analysis of the Stress Grading System using the Example of a 20 kV Large Hydro Generator."
[94] E. Sharifi-Ghazvini, "Analysis of electrical and thermal stresses in the stress relief system of inverter fed medium voltage induction motors," 2011.
[95] C. Staubach and R. Merte, "Direct electrical field strength distribution determination on electrical apparatus by means of an electro-optical miniature field sensor," *19th International Symposium on High Voltage Engineering, Pilsen, Czech Republic*, pp. 23-28, 2015.
[96] D. Burley. “Ship Installation Of Insulated Bus Pipe,” presented at NSRP Meeting Newport News, Virginia October 5, 2011.
[97] Z. Zhang, W. Rao, L. Ruan, J. Zhao, Zhao, S. Meng and F. Yang, “Research on the temperature rise characteristic of 10 kV fully insulated busbar system.” In Proceedings of the 2016 China International Conference on Electricity Distribution (CICED), Xi’an, China, pp. 1–4, August 2016.

[98] P. Taklaja, I. Kiitam, P. Hyvönen and J. Klüss, "Test setup for measuring medium voltage power cable and joint temperature in high current tests using thermocouples", *IEEE Electrical Insulation Conference*, June 2016.
[99] S. Roychoudhury, A. Deb, G. Sarkar and J. Bera, "Virtual. Laboratory for Performing Tests on a Single-Phase Power Transformer", *IETE Journal of Education*, vol. 55, no. 1, pp. 11-25, 2014.
[100] K. F. Fadhil, "Pressure and temperature effects on corona onset voltage in electrostatic precipitators," *International Journal of Physical Sciences,* vol. 12, no. 5, pp. 52-59, 2017.
[101] American Audio, "V-01 Plus Series User Instructions," 2008.
[102] National Instrument, "NI 9215 Datasheet," 2016.
[103] National Instrument, "NI 9263 Datasheet," 2016.
[104] RS, "Thermocouple Slection Guide".
[105] W. M. Haynes, CRC Handbook of Chemistry and Physics. CRC press, 2014.
[106] CROPICO, "Microhmmeter Type DO5000 Series Operating Instructions," 2011.
[107] Ness Engineering, "NESS ENGINEERING TECHNICAL DATA METAL/ALLOY RESISTIVITY," Accessed:April-2022. [Online]. Available: http://nessengr.com/techdata/metalresis.html#metal
[108] R. A. Dias, G. R. S. Lira, E. G. Costa, R. S. Ferreira and A. F. Andrade, "Skin effect comparative analysis in electric cables using computational simulations", *2018 Simposio Brasileiro de Sistemas Eletricos (SBSE)*, pp. 1-6, 2018.
[109] B. Tabei, A. Ametani, A. M. Gole and B. Kordi, "Study of skin and proximity effects of conductors for mtl-based modeling of power transformers using fem", *2020 IEEE Power Energy Society General Meeting (PESGM)*, pp. 1-5, 2020.
[110] A. Payne, "The ac Resistance of Rectangular Conductors", 2016.
[111] IEC 60287-1-1:2006 Electric cables – Calculation of the current rating – Part 1-1: Current rating equations (100% load factor) and calculation of losses – General, 2006.
[112] The Engineering ToolBox, Air - Dynamic and Kinematic Viscosity, Accessed:April-2022. [Online]. Available: https://www.engineeringtoolbox.com/air-absolute-kinematic-viscosity-d_601.html
[113] The Engineering ToolBox, Air - Thermal Diffusivity, Accessed:April-2022. [Online]. Available: https://www.engineeringtoolbox.com/air-thermal-diffusivity-d_2011.html
[114] S. W. Churchill and H. H. Chu, "Correlating equations for laminar and turbulent free convection from a vertical plate," *International journal of heat and mass transfer*, vol. 18, no. 11, pp. 1323-1329, 1975.
[115] The Engineering ToolBox, PTFE Properties, Accessed:April-2022. [Online]. Available: https://www.engineeringtoolbox.com/
[116] H. Haghighi, I. Cotton, R. Gardner, and B. Sauvage, "Definitions of Test Conditions for High Voltage Aerospace Systems Using the IAGOS Atmospheric Dataset," *SAE Technical Paper,* 2018.
[117] M. Cavcar, "The International Standard Atmosphere (ISA)," Anadolu Univ. Turkey, pp. 1–7, 2000.
[118] W. Zaengl, S. Yimvuthikul, and G. Friedrich, "The temperature dependence of homogeneous field breakdown in synthetic air," IEEE Transactions on Electrical Insulation, vol. 26, no. 3, pp. 380–390, 1991
[119] C. R. Rao and G. R. G. Raju, "Growth of ionization currents in dry air at high values of E/N", *J. Phys. D: App. Phys.*, vol. 4, pp. 494-503, 1971.
[120] L. Lusuardi and A. Cavallini, "The problem of altitude when qualifying the insulating system of actuators for more electrical aircraft", *2018 IEEE International*

Conference on Electrical Systems for Aircraft, Railway, Ship Propulsion and Road Vehicles & International Transportation Electrification Conference (ESARS-ITEC), pp. 1-4, Nov. 2018.
[121] R. Pietsch, "Materials and Emerging Test Techniques," *Electricity Supply Systems of the Future*: Springer, pp. 569-609, 2020.
[122] Glassman High Voltage, Accessed: March-2022. [Online]. Available: https://www.vicomtrade.cz/pdf/glassman-catalog.pdf
[123] Keithley, 6485 Bench Digital Picoammeter Data Sheet, Accessed:March-2022. [Online]. Available: https://uk.rs-online.com/web/p/multimeters/7600307
[124] "IEC 60270:2000 Standard", *High-voltage Test Techniques – Partial Discharge Measurements*, 2000.
[125] SubsTech, "Ethylene tetrafluoroethylene (ETFE)," 2013.
[126] T. Okamoto, M. Koyama, Y. Inoue, N. Takahashi, and S. Nakamura, "Percolation phenomena of field grading materials made of two kinds of filler," in *Proceedings of 2001 International Symposium on Electrical Insulating Materials*, IEEE, pp. 83-86, 2001.
[127] VALQUA, *Characteristics of fluroresin*, Accessed:April-2022. [Online]. Available: http://www.seal.valqua.co.jp/en/fp_property/fluoroplastics_characteristic/.